University of Stuttgart

Institute of Geodesy

Investigation of the relationship between satellite altimetry and the environment by multisensor spaceborne data

Master Thesis

Geomatics Engineering

University of Stuttgart

Yiming Chen

Stuttgart, August 2020

Supervisor: Dr.-Ing. Mohammad J. Tourian

University of Stuttgart

Erklärung Der Urheberschaft

Ich erklre hiermit an Eides statt, dass ich die vorliegende Arbeit ohne Hilfe Dritter und ohne Benutzung anderer als der angefertigt habe; die aus fremden Quellen direkt oder indirekt bernommenen Gedanken sind als solche kenntlich gemacht. Die Arbit wurde bisher in gleicher oder hnlicher Form in keiner anderen Prfungsbehrde vorgelegt und auch noch nicht verffentlicht.

Ort, Datum: Unterschrift:

Abstract

Inland water surface bodies (e.g. rivers and lakes) are one of the most crucial resources to human life and society. However, excessive consumption of freshwater results shortage of the ground and surface inland water. The water crisis has aroused people's concern all over the world. Therefore, continuous monitoring of water bodies has been a critical task for human being in the past decades and will continues to be one in the future.

Satellite altimetry, a measurement technique which has wide coverage, relatively good temporal resolution, and continuous measurements has become an important part in the hydrological studies. In recent years, new SAR altimeter and techniques are exploited to provide accurate and reliable measurements over inland water. The Open-Loop Tracking Command (OLTC), for instance, contributes to the improvement of the reliability of altimetry data supporting by an on-board Digital Elevation Model (DEM) database. However, loss of tracking and wrong tracking still happens while inland water monitoring, especially for the small water bodies located in a complex environment. Although altimeter can acquire water information, its height products also have a non-negligible error from the true values.

In this thesis, we investigate how the environment influences the altimetry measurements. Therefore, fourteen virtual stations that are located in different environments and terrain (e.g. plain, mountain or valley) are determined. Then, we used the altimetry data of Sentinel-3 mission to generate the time series of water levels from December 2018 to December 2019 for all virtual stations. After determining the waveform and time series, we parameterized the feature of the waveform and the environment conditions within the footprints. To this end, we extracted 10 indicators out of waveforms including 1) thermal noise, 2) the number of peaks, 3) the position of the highest peak, 4) the power of the highest peak, 5) the position of the first peak, 6) the ratio of thermal noise and maximum power, 7) the width of the highest peak, 8) kurtosis, 9) peakiness, and 10) noise level. We then characterized the environment by 8 indicators including 1) the area of the river, 2) the width of the river, 3) the number of water bodies, 4) the distance between the river and nadir point, 5) vegetation coverage, 6) elevation variance, 7) elevation difference, and 8) crossing angle. Finally, we analyzed the effect of the environment on the altimetry measurement by the combination of the time series of water surface height, waveform indicators, and environmental indicators. Our analysis shows the following conclusions: 1) The high noise level is associated with the elevation difference and the number of water bodies in a complex environment. 2) The high noise level contributes to the large height difference between retrackers. 3) The high elevation difference is related to the high noise level. Nevertheless, it can generate a

large height difference between retrackers.

Key Words： Altimetry; Multiple sources; Waveform; Environmental influence

Content

List of Figures

List of Tables

Chapter 1

Introduction

Water covers more than seventy percent area of the earth's surface and the total volume of water is approximately 333 million km^3, including 97.47% saltwater and 2.53% freshwater. Nevertheless, liquid freshwater that can be directly consumed by human only account for 0.26% of the freshwater (Gleick, 1993). Global warming, caused by the surge of greenhouse gas emissions leads to changes in the distribution of water resources over many regions (S. Hagemann, 2013). Meanwhile, excessive consumption of freshwater results in the drain of the ground and surface inland water (lakes, rivers, etc.). The water crisis has aroused people's concern all over the world. Therefore, continuous monitoring of water bodies has been a critical task for human being in the past decades and will continues to be one in the future.

There are two commonly used approaches for water body monitoring: 1) Gauging station measurement, a traditional method to monitor water resources which can achieve high accuracy but restricted by its distribution and high construction cost; 2) Satellite altimetry, which has larger coverage and higher temporal resolution and continuous measurements. The quality and accuracy of altimetry are not comparable with that of the in-situ data because of errors from different sources. With the development of altimetry, especially the application of Delay-Doppler (SAR) altimeter, the aforementioned problems have been generally overcome in ocean application. However, low accuracy and unreliable quality of data which are driven by altimeter performance and post-processing technique over inland water bodies are still unfixed issues (Berry et al., 2005).

To ensure the quality of data over inland water, the Open-Loop Tracking Command (OLTC) is utilized on newly designed satellites (Jason-3, Sentinel-3). It is capable to set a proper reception window of altimeter and to ensure that received waveform coming from desired water bodies, supported by on-board pseudo-DEM tables and DORIS system (Le Gac, 2019). The received waveform is exploited to extract geophysical parameters (water level, backscatter), but it is normally contaminated by the environment within corresponding footprints (Tourian, 2012). This contamination changes the shape of the waveform and complicates the construction of it, further results in failing to determine the water level height. Therefore, it is important to understand the connection between the environment and the waveform for the sake of further improvement of measurement accuracy over inland water. In this thesis, we investigate the effect of the environment within footprints on the waveform and its height products using the Synthetic Aperture Radar (SAR) altimetry data obtained in OLTC mode, optical images, and DEM data.

1.1 Background of Satellite Radar Altimeter

American geophysicist W. M. Kuala officially formalized the concept of satellite altimetry at a Solid-Earth and ocean physics symposium in August 1968 and he emphasized the importance of altimetry in geodesy and hydrology field (Kuala, 1968). Participants made a proposal that develops an altimeter which has 10 cm level accuracy and 1° spatial resolution in ten years. Over the years, altimetry technique has made a great contribution to many fields. ***Figure 1.1*** shows launched and planned altimetry missions since 1985. ***Table 1.1*** presents information about launched and planned altimetry missions since 1985.

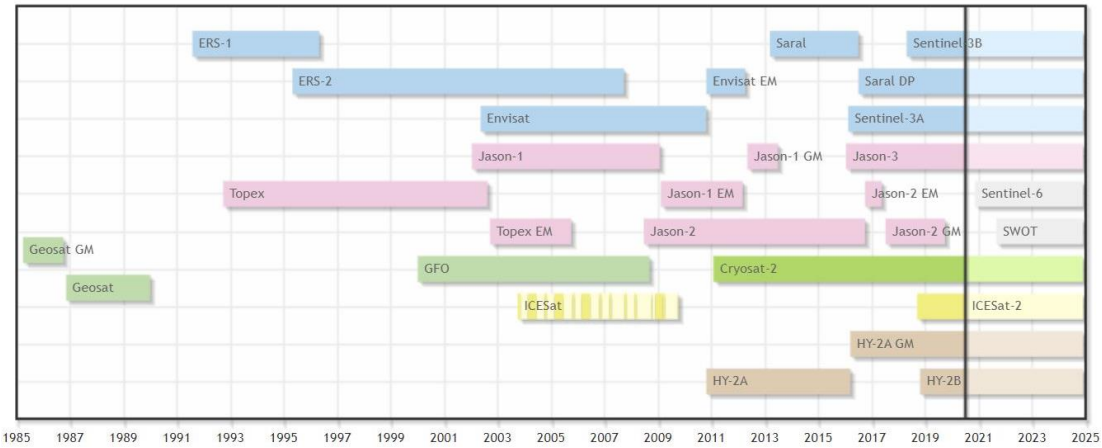

Figure 1.1: Operating period of altimetry satellite since 1985 (*Open Altimeter database, TUM*)

Table 1.1: Information about some altimetry mission since 1985

Satellite	Agency	Year	H	Altimeter	f	T	I	ε
Skylab	NASA	1973	435	S193	-	-	50	Range: 1m Orbit: about 5m
Seasat	NASA	1978	800	ALT	13.5	17	108	Range: 5cm Orbit: about 1m
Geosat	US Navy	1985	800	RA-	13.5	17	108	Range: 4cm Orbit: 30-50cm
ERS-1	ESA	1991	785	RA	13.8	35	98.5	Range: 3cm Orbit: 8-15cm
Topex /Poseidon	NASA CNES	1992	1336	Topex Poseidon-1	13.6/5.3	10	66	Range: 2cm Orbit: 2-3cm
ERS-2	ESA	1995	785	RA	13.8	35	98.5	Range: 3cm Orbit: 7-8cm

GFO	US Navy NOAA	1998	800	GFO-RA	13.5	17	108	Range: 3.5cm Orbit: /
Jason-1	CNES NASA	2001	1336	Poseidon-2	13.6/5.3	10	66	Range: 2cm Orbit: 2-3cm
Envisat	ESA	2002	800	RA-2	13.6/3.2	35	98.5	Range: 2-3cm Orbit: 2-3cm
Jason-2	CNES NASA Eumestat NOAA	2008	1336	Poseidon-3	13.6/5.3	10	66	Range: 2.5cm Orbit: <3cm
Cryosat-2	ESA	2010	717	SIRAL	13.575	369	92	Range: <3cm Orbit: 2-6cm
HY-2	SOA	2011	963	-	13.58/5.25	14	99.3	Range: <4cm Orbit: /
SARAL	ISRO CNES	2013	800	AltiKa	35.75	35	92	Range: 3.5cm Orbit: <3cm
Sentinel-3A	ESA	2016	815	SRAL	13.6/5.3	27	98.5	Range: 3cm Orbit: <3cm
Jason-3	CNES NASA Eumestat NOAA	2016	1336	Poseidon-3	13.6/5.3	10	66	Range: 3.5cm Orbit: <3cm
Sentinel-3B	ESA	2018	815	SRAL	13.6/5.3	27	98.5	Range: 3cm Orbit: <3cm

Satellite: Name of satellite altimetry

Agency: Agency transmitted **s**atellite

Year: Satellite launch date (Unit: year)

Height: Orbit Height (Unit: km)

Altimeter: On-board altimeter

f: Waveform frequency (Unit: GHz)

T: Orbit period (Unit: day)

I: Inclination (Unit: degree)

ε: Error

The first satellite Skylab loaded radar altimeter was transmitted on May 14, 1973. It

demonstrated the concept of using the satellite altimeter for geoid determination. Although noise level and systematic error were up to 1-3m and 10m, successful launch still signified a big approach to the practical application (Leitao et al., 1976). Seasat, launched in June 1978, was the first altimetry satellite applied in the oceanology field. Its on-board altimeter first implemented dechirp pulse compression technology, which significantly improved the resolution of altimeter (Tapley et al., 1982). Seven years later, the USA Navy transmitted Geosat satellite which marks ocean geoid can be determined from space (Cartwright et al., 1990). It was henceforth followed by a series of successively launched advanced altimetry satellites with different purposes: ERS, Topex/POSEIDON, Jason1/2/3, Envisat, ICEsat1/2, Sentinel-3A/B

Although most of these satellites are initially designed for ocean applications, their continental application has been demonstrated since Rapley et al. (1987) firstly used Seasat data to explore inland water targets. However, the aforementioned problems of the performance of the altimeter and post-processing technique, restricted the reliability and accuracy of data on inland water. Recently, benefitted from the Synthetic Aperture Radar (SAR) technique and the new OLTC tracking mode, the altimeter's performance over inland water has been significantly improved (Wingham et al., 2006; ESA, 2018; Biancamaria, 2018). The remaining problem is the uncertainty of the returned echo (waveform) during post-processing.

Variable conditions of different inland water and the complex environment within the altimetry footprints (***section 1.2.2***) are the main factors that result in this uncertainty. However, there have been very few researches dedicated to the relation between the waveform and two aforementioned reasons. Berry et al. (2005) reported that different sizes of water bodies present different shapes of the returned waveform, and classified them into four groups accordingly. Remy et al. (2012) indicated that waveform is influenced by snow characteristics fluctuation, and leads to the variation of the leading edge width in the central part of East Antarctica. Maillard et al. (2015) took environmental factors (river shape and width) into account to improve the precision of altimetry measurements of the water level. These papers focused on determining a single environmental factor and solving a specific problem, rather than comprehensively considering multiple factors. As a matter of fact, the waveform is associated with various environmental factors including the variation of elevation, coverage of the surface, the position of the water body within the footprints and so on. How these factors impact the shape of the waveform is still uncertain.

1.2 Basics of altimetry waveform

The basic content of altimetry is complicated and covers multiple fields. Therefore, only two concepts that are closely related to this thesis are presented in this section.

1.2.1 Satellite altimetry waveform

The waveform in altimetry data is a temporal profile (Marth et al., 1993) describing accumulated and smoothed power scattered from a ground object and received by the

on-board altimeter. The process of interacting between emitted pulse and scattering surface as well as its corresponding part in the waveform shown as follow schematic.

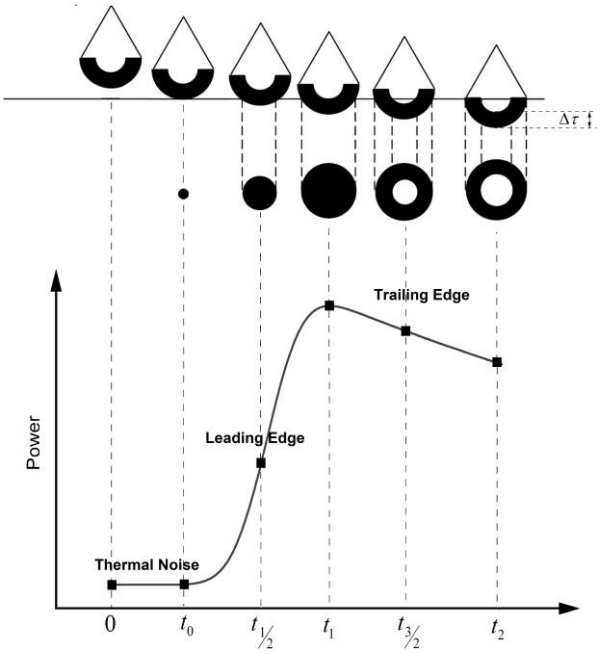

Figure 1.2: Interaction of pulse and scattering surface, and construction of waveform (Gao, 2020)

1. $0 < t < t_0$, altimeter emits radar pulses towards the earth surface in nadir direction. Pulses emitted by antenna form a semi-spherical shell. The width of this shell determined by pulse duration $\Delta\tau$ and width of pulse $c\Delta\tau$ is altimeter's range resolution.
2. $t = t_0$, pulse front faces and illuminates nadir points and a return echo begins to return toward altimeter.
3. $t_0 < t < t_1$, illuminated area continuously grows and forms a growing disc centered on nadir point until trailing edge reaches the surface. During this period, altimeter receives powers from antenna beam-limited area. Ascent part of waveform corresponds to this period
4. $t = t_1$, illuminated area stops increasing and begins to form an annular ring at the same time keeping area constant. This epoch corresponds to the peak point of waveform, received power to reach its maximum.
5. $t_1 < t < t_2$, the illuminated ring is getting larger and narrower, but still keep area constant. In this period, received power reflected from outside of antenna beam-limited area. It results in the declination of power and forms the trailing part of the waveform.

In general, a received signal undergoes different Rayleigh fluctuations when altimeter moves along the orbit and path lengths to multiple facets change (Chelton et al., 1989). Many individual waveforms must be averaged to obtain a mean and smooth waveform.

The averaged waveform (***Figure 1.2*** bottom) is mean returned power series which recorded by altimeter (Brown, 1977), it consists mainly of three parts:

1. **The thermal noise:** This noise is generated by altimeter before it receives the first return signal. It remains a constant power level to return waveform.
2. **The leading edge:** It is the main part of the waveform where maximum power return from ground occurs on. The Surface Wave Height (SWH) and range between satellite and scattering surface at nadir point (if surface is ocean) can be extracted from this part.
3. **The Trailing edge:** Decaying return power in this part result in the trailing edge. It can be approximated by a straight line whose slope depends on the altimeter antenna pattern and the off-nadir angle (Chelton et al., 2001).

Mean sea level corresponds to half of the distance between wave crests and troughs. It can be determined by tracking the half power point on the leading edge. SWH can be determined from the slope of the leading edge of the returned waveform in the vicinity of the half-power point (Chelton et al., 1989).

The waveform characteristics mentioned above are appropriate for waveform extracted from ocean and large lakes, but not for inland water application. Berry et al. (2005) classified waveform from different lakes to four types as shown in ***Figure 1.3***. Decreasing the size of the lake, the number of Brown model waveforms decreases, and quasi specular waveforms occur more times. Occurrence frequency of flat patch waveforms is highest among four types for the case of a s mall water body.

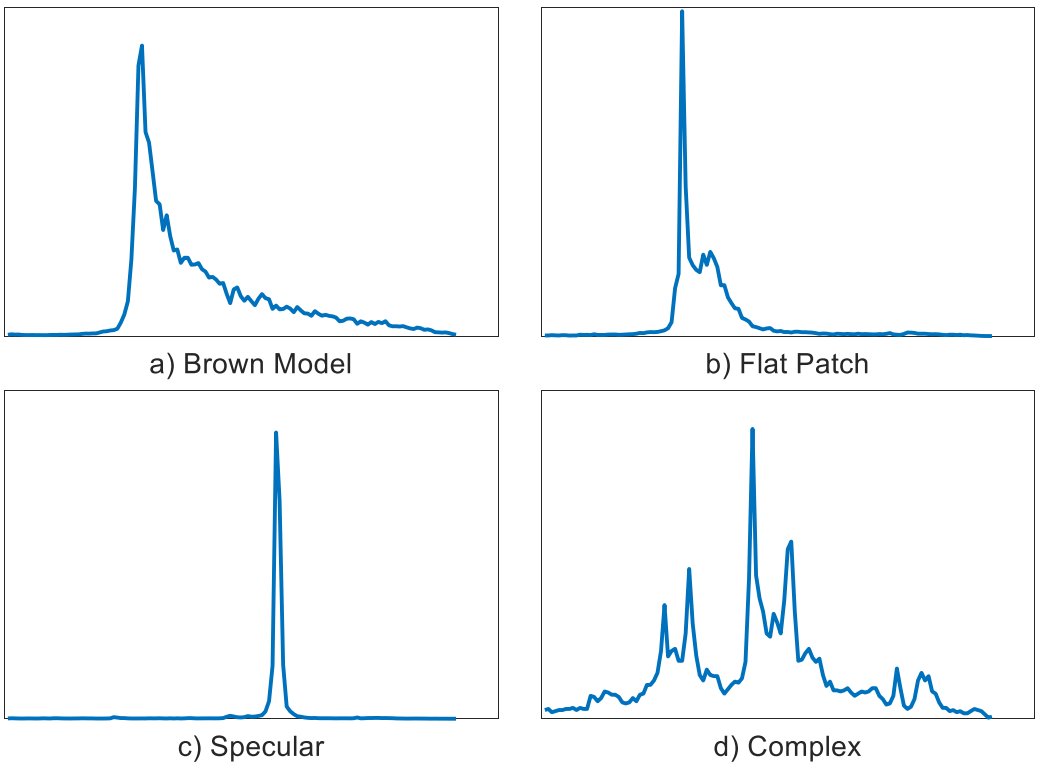

Figure 1.3: Example of four different types of waveform

The situation on rivers is more complex than lakes because the shape of a river is normally a narrow square or even a line, making it more difficult for altimeter to acquire water information from rivers. Meanwhile, the environment surrounds the river affects more on the shape of the waveform, the position of the leading edge and power amplitude.

1.2.2 Footprints

The footprint of a conventional radar altimeter is the area on water surface illuminated by the antenna beam angle defined by the half power point of the antenna gain (Chelton et al., 1989). In principle, the effective footprint area can be calculated from the pulse duration τ, altitude of the satellite R_0, the radius of earth R_e and significant wave height $H_{1/3}$ which is approximate to the crest-to-trough height of the 1/3 largest waves in the footprint. Taking two satellites whose altitudes are 800 km and 1335 km as an example, the effective footprint diameters computed from equation 1.2.1 are presented in ***Table 1.2***.

$$A = \frac{\pi R_0 \left(c\tau + 2H_{\frac{1}{3}} \right)}{1 + \frac{R_0}{R_e}} \tag{1.2.1}$$

Table 1.2: Conventional altimeter effective footprint diameters as a function of significant wave height(Chelton et al., 1989)

$H_{1/3}$ (m)	Effective footprints diameter (R_0 = 800km) (km)	Effective footprints diameter (R_0 = 1335km) (km)
0	1.6	2.0
1	2.9	3.6
3	4.4	5.5
5	5.6	6.9
10	7.7	9.6
15	9.4	11.7
20	10.8	13.4

The Delay Doppler/SAR altimeter (SAR mode) is different from the conventional radar altimeter as it implements coherent processing of groups of transmitted pulses. Its processor allows to sharpen the area of the pulse in the along-track direction. The Doppler beam formation in SAR mode allows to discriminate the direction of arrival of the echoes in the along-track direction instead of the measure of the time delay. Hence, the width of footprints is defined independently in both independent directions, the along-track and the across-track directions. In the across-track direction, the width of footprints is defined as the radius of conventional altimeter footprints. However, in the along-track direction, the width of the footprint is defined as the sharpened beam-limited area which can be calculated by equation 1.2.2 (ESA, 2018)

$$d = h\,\frac{\lambda}{2v}\,\frac{PRF}{64} \tag{1.2.2}$$

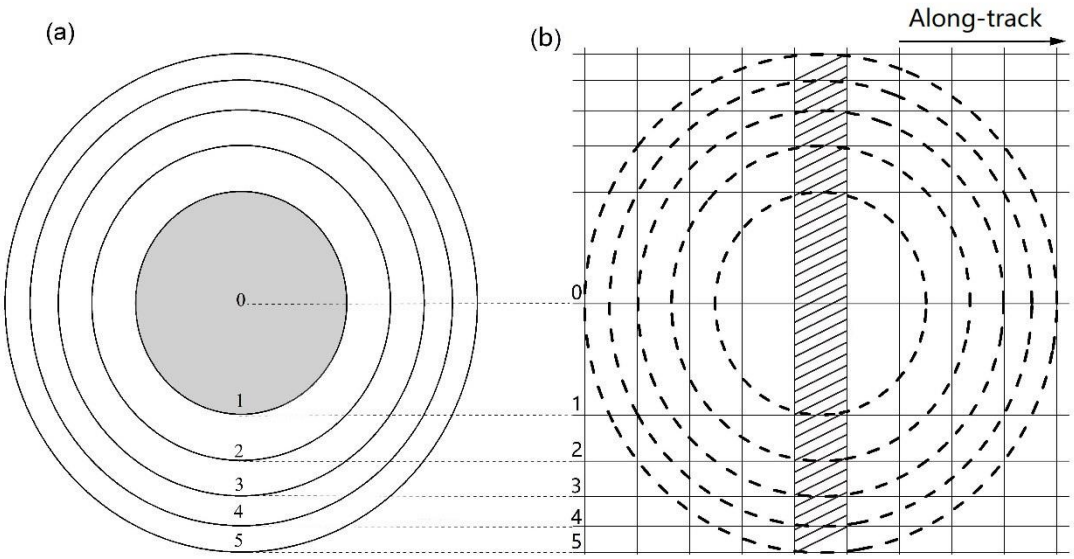

Figure 1.4: Comparison of conventional (a) and SAR (b) altimetry's footprints (Gao, 2020)

Figure 1.4a is schematic of altimeter measuring in conventional mode (LRM). Center region presents ideal footprints, each annulus indicates different time delay and returns different delay pulse. ***Figure 1.4b*** is schematic of altimeter measuring in SAR mode whose along-track resolution has been significantly improved and across-track resolution remains the same, its footprints is the swath in the center.

Chapter 2

Data and case study

As mentioned in chapter one, this thesis is dedicated to assessing the relation between altimetry waveform, water level, and the environment within its corresponding footprints. Waveform and water level can be obtained from altimetry data. The environmental conditions can be evaluated by remote sensing images and DEM data. Therefore, in this chapter, we firstly introduce Sentinel-3 altimetry data, Sentinel-2 and Landsat-8 image data, and STRM DEM data which are used for our purpose. Afterward, the case study is presented in the second section. For the sake of diversity of the environmental conditions, we selected two types of rivers: rivers in the valley and rivers in the plain area. In addition, these rivers have different water flow and climate conditions. At the end of the chapter, we would determine fourteen virtual stations located on two rivers with the help of remote sensing images.

2.1 Data

2.1.1 Sentinel-3 data

Sentinel-3 satellites are jointly designed and operated by ESA and EUMETSAT as part of the European Commission Copernicus program, which aims to monitor earth for global environment and security. It can provide multiple sorts of data about sea surface topography, sea and land surface temperature, and ocean and land surface color with high accuracy and reliability. The Sentinel-3 mission is based on two identical satellites flying on a polar, Sun-synchronous orbit at altitude 815 km, an inclination of 98.6°, a repeat cycle of 27 days and having a 140 degrees orbit phase difference between twins. First satellite, Sentinel-3A, was launched on 16 February 2016. Sentinel-3B which doubled the coverage of mission became the second member of the constellation on 25 April 2018.

Embarked instruments on Sentinel-3 are shown as follow:

- A push-broom imaging spectrometer instrument called the Ocean and Land Color Instrument (OLCI). A dual view (near-nadir and backward views) conical imaging radiometer called the Sea and Land Surface Temperature Radiometer (SLSTR) instrument. OLCI and SLSTR are devoted to optical imagery acquisition.
- A dual-frequency SAR altimeter called the SAR Radar Altimeter (SRAL) operating in Ku band (15.575 GHz) and C band (5.42 GHz). SRAL can operate in SAR (Synthetic Aperture Radar) or LRM (Low Resolution Mode) processing

mode.

- A Microwave Radiometer (MWR) instrument and OLTC Tracking mode (more detail on section 3.1.1 supporting the SRAL by providing wet atmosphere correction and maintaining a stable tracking control.
- A Precise Orbit Determination package including a Global Navigation Satellite Systems (GNSS) instrument, a Doppler Orbit determination and Radio-positioning Integrated on Satellite (DORIS) instrument and a Laser Retro-Reflector (LRR). These systems are used to precisely calculate the satellite orbit.

Two follow-on satellites Sentinel-3C and Sentinel-3D are planned to launch in 2021.

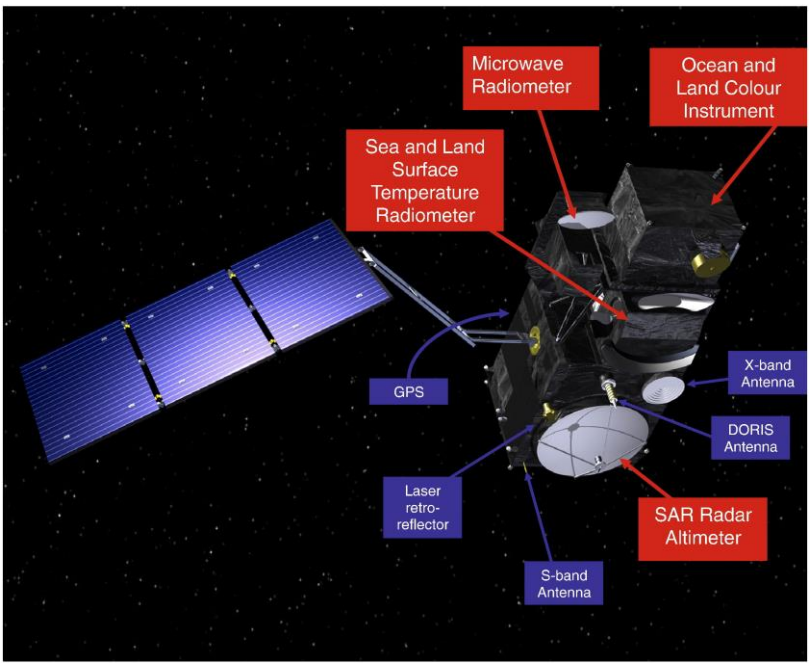

Figure 2.1: Sentinel-3 and payload instrument (Credit: ESA)

For our water level application, Level 2 product produced by SRAL altimeter has been used. SRAL is a redundant dual-frequency (C-band and Ku-band) instrument for determining the two-way delay of the radar echo from the Earth's surface with a precision better than a nanosecond (ESA, 2018). It has two observation modes: Low Resolution Mode (LRM) and Synthetic Aperture Radar (SAR) mode.

LRM mode is the conventional altimeter pulse limited mode in which Pulse Repetition Frequency (PRF) is about 1924Hz. These pulses are transmitted toward the ground follow a model of 3 Ku band pulses + 1 C band pulse + 3Ku band pulses. On-board altimeter processes and average pulses to produce a 128 bins waveform every 50.9 ms.

SAR mode is the high along-track resolution mode based on Synthetic Aperture Radar technique. The PRF is about 17800 Hz in SAR mode. Transmitted pulses consist of Ku-band bursts and two C band pulses at the two sides of each burst. Each burst contains 66 pulses (1 C band pulse + 64 Ku band pulses + 1 C band pulse), corresponding to a duration of 12.74 ms.

Sentinel-3 has three levels of products in which level 0 product is original measurements and it isn't provided to common users, level 1 (B) product is processed by several steps (i.e. calibration, beam pointing, beam steering, beam stacking, muti-look, etc), and level 2 product that we used in this thesis. The Level 2 products are divided into Land (*SR_2_LAN__*) and Marine (*SR_2_WAT__*) products over different areas. Marine Products contain information sensed over the open ocean, the coastal areas, the sea-ice and over part of the land within a certain distance from the coastline. As far as Land Products contain information sensed over land, the coastal areas, land ice and inland water (ESA, 2018).

2.1.2 Sentinel-2 data

The Copernicus Sentinel-2 mission contains a constellation that consists of two polar-orbiting satellites operated in a 786 km high sun-synchronous orbit, with an inclination of 98.62° and a 180° phase difference between twins. The first satellite Sentinel-2A was launched on 23 June 2015, and its twins Sentinel-2B was transmitted on 7 March 2017. The mission aims at monitoring variability in land surface conditions, and its swath is 290 km width and 10 days revisit cycle for each satellite (5 days with 2 satellites at the equator) will support monitoring of Earth's surface changes. The limitation of satellite coverage is from between latitudes 56° south and 84° north.

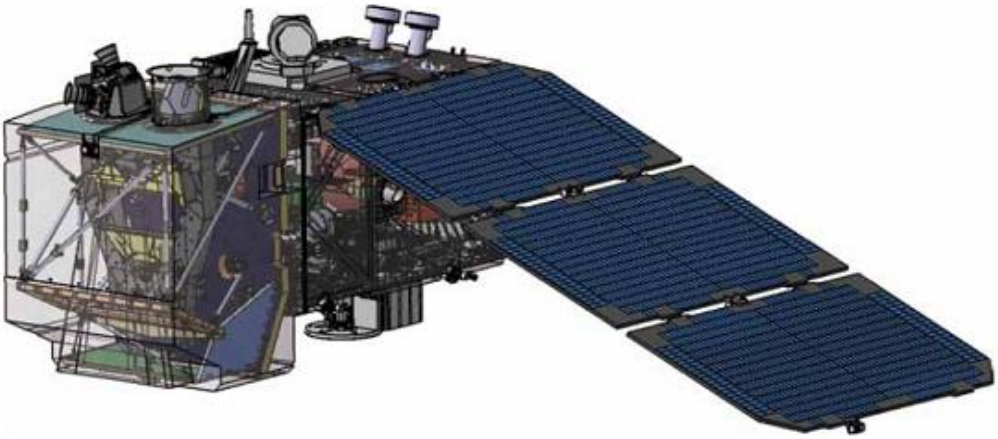

Figure 2.2: Sentinel-2 satellite (Credits: ESA)

Each of the Sentinel-2 satellites carries a single multi-spectral instrument (MSI) with 13 spectral channels in the visible/near-infrared (VNIR) and short wave infrared spectral range (SWIR). MSI uses a push-broom concept whose sensor works by collecting rows of image data in the direction across satellite track and producing new rows for acquisition with the forward motion of satellite along the orbit. The average period of observation over land and coastal areas is approximately 17 minutes and the maximum period of observation is 32 minutes.

Table 2.1: Spectral bands for the MSI sensors (Sentinel-2)

	S2A		S2B		
Band Number	**Central wavelength (nm)**	**Bandwidth (nm)**	**Central wavelength (nm)**	**Bandwidth (nm)**	**Spatial resolution (m)**
Band 1 - Coastal aerosol	442.7	21	442.3	21	60
Band 2 - Blue	492.4	66	492.1	66	10
Band 3 - Green	559.8	36	559.0	36	10
Band 4 - Red	664.6	31	665.0	31	10
Band 5 - Vegetation red edge	704.1	15	703.8	16	20
Band 6 - Vegetation red edge	740.5	15	739.1	15	20
Band 7 - Vegetation red edge	782.8	20	779.7	20	20
Band 8 - NIR	832.8	106	833.0	106	10
Band 8a - Narrow NIR	864.7	21	864.0	22	20
Band 9 - Water Vapour	945.1	20	943.2	21	60
Band 10 - SWIR - Cirrus	1373.5	31	1376.9	30	60
Band 11 - SWIR	1613.7	91	1610.4	94	20
Band 12 - SWIR	2202.4	175	2185.7	185	20

Similar to Sentinel-3, Sentinel-2's products have three levels that provide different kinds of images with different processing methods. In our research, we used Level-2 products which have finished the atmospheric correction and radiometric calibration. That means we can directly execute classification and extract environmental properties from them.

2.1.3 Landsat-8 data

Landsat-8 is the eighth satellite in the Landsat program, which is collaboratively operated by National Aeronautics and Space Administration (NASA) and the United States Geological Survey (USGS). It was launched on 11 February 2013, flying in a sun-synchronous, near-polar orbit, at an altitude of 705 km, inclined at 98.2°, an orbital period of 99 minutes, and a 16-day repeat cycle. Landsat-8 can collect and archive medium resolution (30-meter spatial resolution) multispectral image data affording seasonal coverage of the global landmasses for more than 5 years. It carries a two-sensor payload comprise of the Operational Land Imager (OLI), built by BATC, and the Thermal Infrared Sensor (TIRS), built by NASA GSFC. Both the OLI and TIRS sensors simultaneously image every scene but can be independently exploited if a problem in either sensor arises (USUG, 2019). The OLI sensor collects image data for 9 shortwave spectral bands over a 190 km swath with a 30 m spatial resolution for all bands except the 15 m Pan band, and the TIRS sensor collects image data for two thermal bands with a 100 m spatial resolution over a 190 km swath (***Table 2.2***).

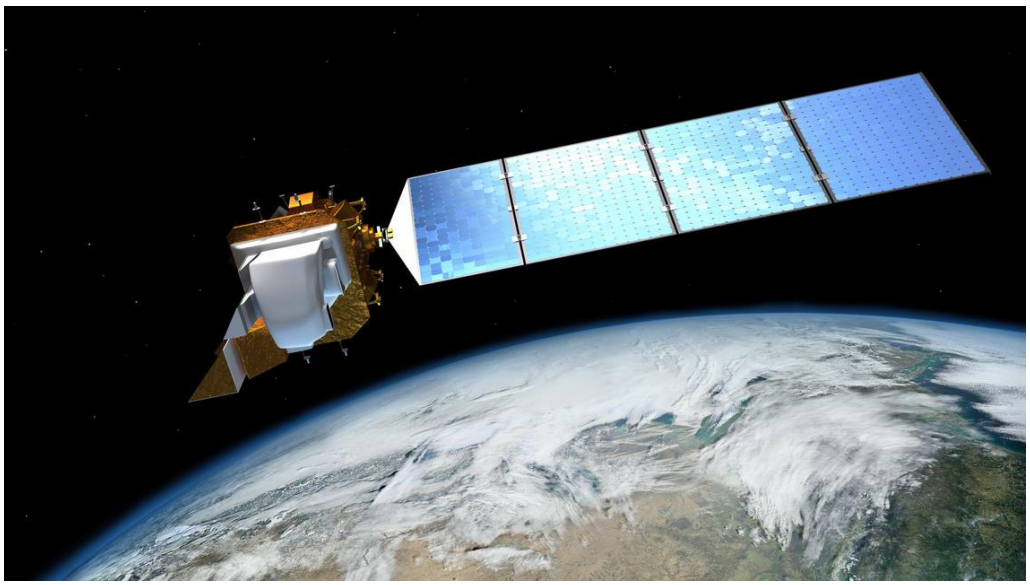

Figure 2.3: Illustration of the Landsat 8 Satellite (Credits: USUG)

Table 2.2: Spectral bands for the OLI and TIRS sensors (Landsat-8)

Band Number	wavelength (µm)	Spatial resolution(m)
Band 1 - Coastal aerosol	0.435 - 0.451	30
Band 2 - Blue	0.452 - 0.512	30
Band 3 - Green	0.533 - 0.590	30
Band 4 - Red	0.636 - 0.673	30
Band 5 - NIR	0.851 - 0.879	30
Band 6 - SWIR-1	1.566 - 1.651	30
Band 10 - TIR-1	10.60 - 11.19	100
Band 11 - TIR-2	11.50 - 12.51	100
Band 7 - SWIR-2	2.107 - 2.294	30
Band 8 - Pan	0.503 - 0.676	15
Band 9 - Cirrus	1.363 - 1.384	30

In this thesis, we used the Level 1C Landsat-8 product which is also post-processed by geometric and radiometric correction. Environmental properties can be directly extracted from the product without further processing. The spatial resolution of images for Landsat-8 (30 m) is lower than Sentinel-2 (20m). Therefore, Landsat-8 is the supplementary data in the case of river targets are covered by cloud or shadow in Sentinel-2 images.

2.1.4 Shuttle Radar Topography Mission data

The Shuttle Radar Topography Mission (STRM) is an international project spearheaded by the U.S. National Geospatial-Intelligence Agency (NGA) and the U.S. National Aeronautics and Space Administration (NASA). It aims at obtaining digital elevation models on a near-global scale from 56°S to 60°N, generating the most complete high-resolution digital topographic database of Earth prior to the release of the ASTER GDEM in 2009. DEM data was acquired through a specially modified radar system that flew

on-board the Space Shuttle Endeavour during the 11-day STS-99 mission in February 2000.

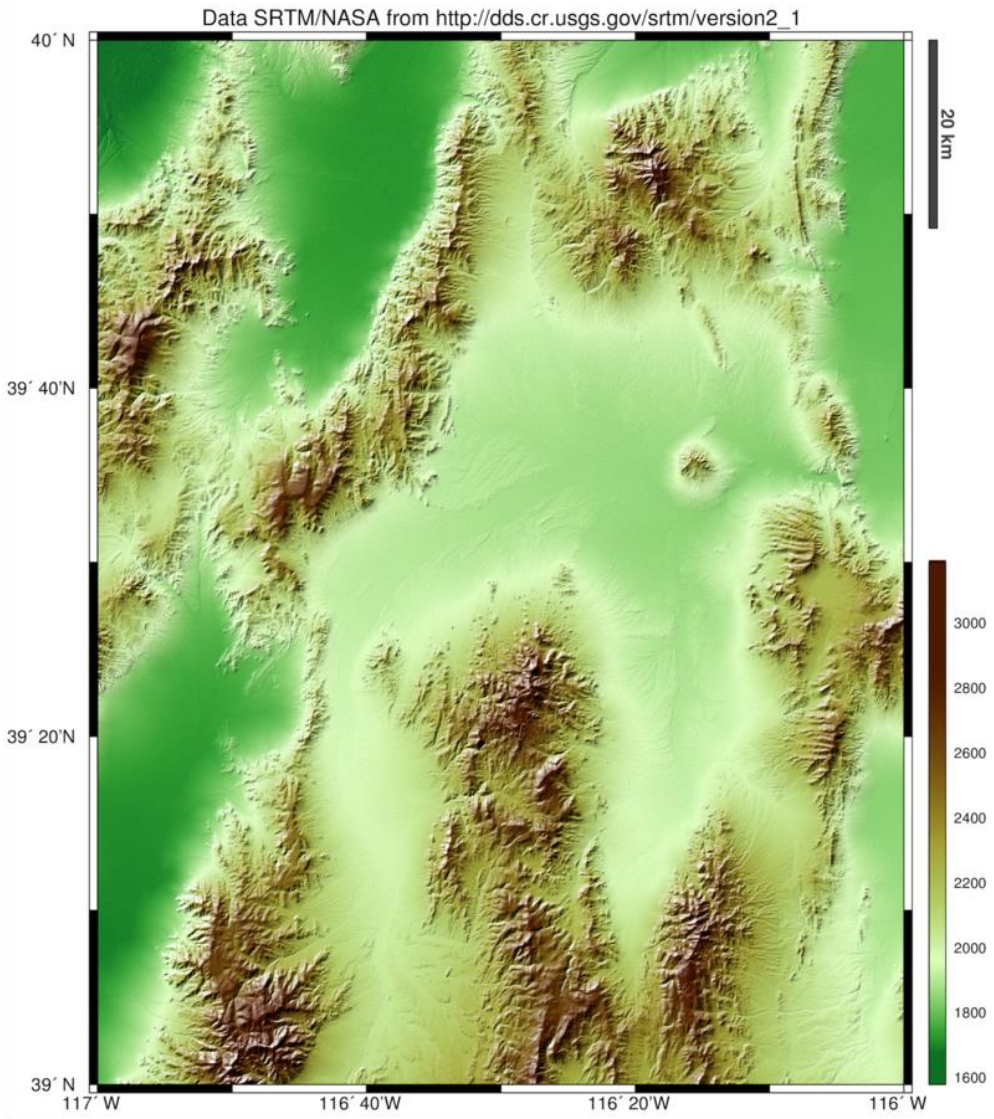

Figure 2.4: Example of a map of Nevada from SRTM1 data (Credits: USGS)

The resolution of the original data is one arcsecond (30 m). The coverage includes Africa, Europe, North America, South America, Asia, and Australia. However, the data is only available to governments. Hence, the product we used in this thesis is STRM 3 and its resolution is three arcseconds (about 90 m). Considering the size of SAR footprints is about 330 m·2000 m (general condition), STRM 3 is sufficient for describing the topography within the footprints.

2.2 Case study

2.2.1 Yarlung Tsangpo River

The Yarlung Tsangpo River is the longest plateau river in China, located in Tibet Autonomous Region. It is one of the highest rivers in the world. The river originated from the Jemajangzong Glacier, the north of the Himalaya mountains in southwest Tibet, whose upstream also called Maquan River. The Yarlung Tsangpo River flows across the south of Tibet from west to east and turns southward at the easternmost peak of Himalaya. It flows out of Chinese territory through Bhashika in the end. The river is 2900 km long with a basin area of $6.17 \cdot 10^5$ km. 2057 km of the total length and $2.4 \cdot 10^5$ km^2 of the basin areas are located within China. The mainstream above Lazi is upstream. The lowest point of the riverbed of the upstream is at 3950 m above sea level, which is the alpine valley zone.

The annual variation of precipitation in the Yarlung Tsangpo River basin is small and its distribution is uneven. The wet season is from July to September, accounting for 50% to 80% of the annual precipitation. Meanwhile, more meltwater from snow and ice flows into the rivers during the months with the most rainfall, as resulting in a high water level. The annual precipitation of the YarlungZangbo River is less than 300 mm in upstream and higher than 300 mm in midstream which belongs to the plateau temperate climate. However the downstream of the basin is high temperature and rainy, with an average annual rainfall of more than 4000 mm near Basica. Most of the virtual stations (***Figure 2.5***) of Yarlung Tsangpo River are located in the upstream and midstream of the river.

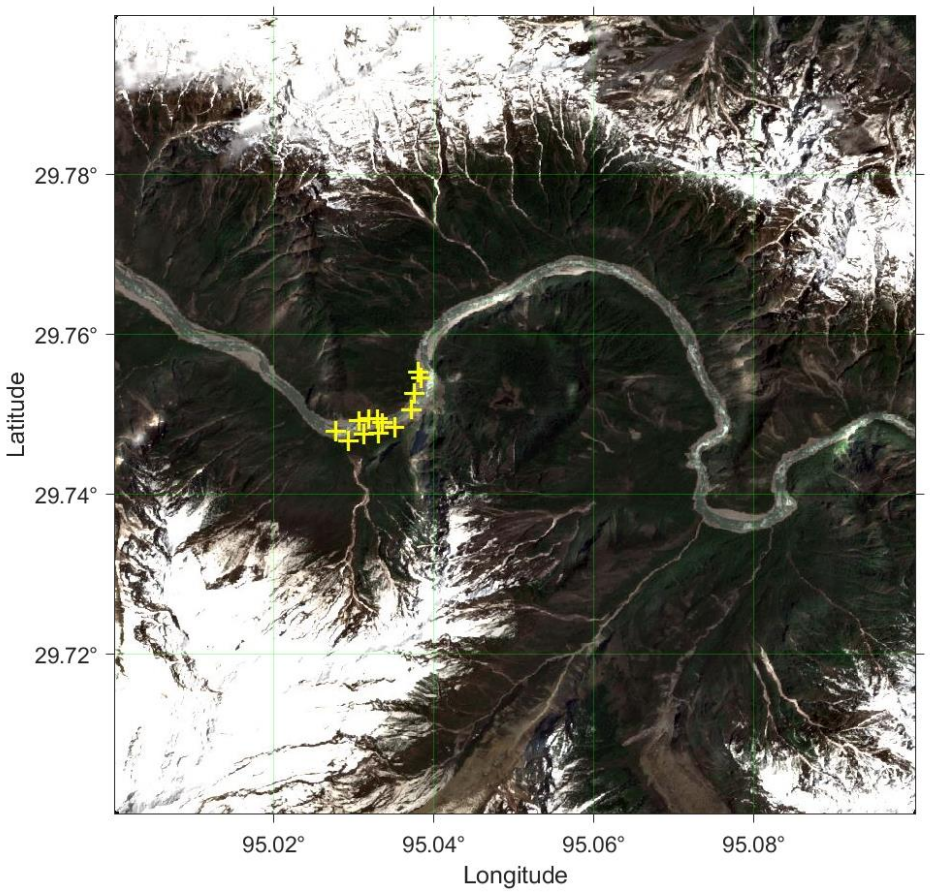

Figure 2.5: Part of the Yarlung Tsangpo River and the location of virtual station 1 (yellow cross)

2.2.2 Yangtze River

The Yangtze River originates from the Ratandon peaks in the Qinghai-Tibetan Plateau, flows through 11 provincial administrative regions include Qinghai, Tibet, Sichuan and Shanghai more than 6300 km. It runs through an area of about $2 \cdot 10^6$ km^2 before finally discharging into the East China Sea in the east of Chongming Island. It is the largest river in Asia in terms of water discharge and the third-longest river in the world (Milliman et al., 1983).

The upstream of the Yangtze River (serval virtual stations located in this reach), also known as Jinsha River (***Figure 2.6***), has a basin area of $5 \cdot 10^5$km^2, accounting for about 26 percent of the Yangtze River basin area. The middle and upper reaches of the Jinsha River are surrounded by valleys except for the estuary of tributaries, where the river valley is slightly wider, the slope of most valleys is between 35° and 45° and more than 60° ~ 70° for some cliffs. It is worth mentioning that water height difference of the river is large. The difference can reach 220m in ten kilometers.

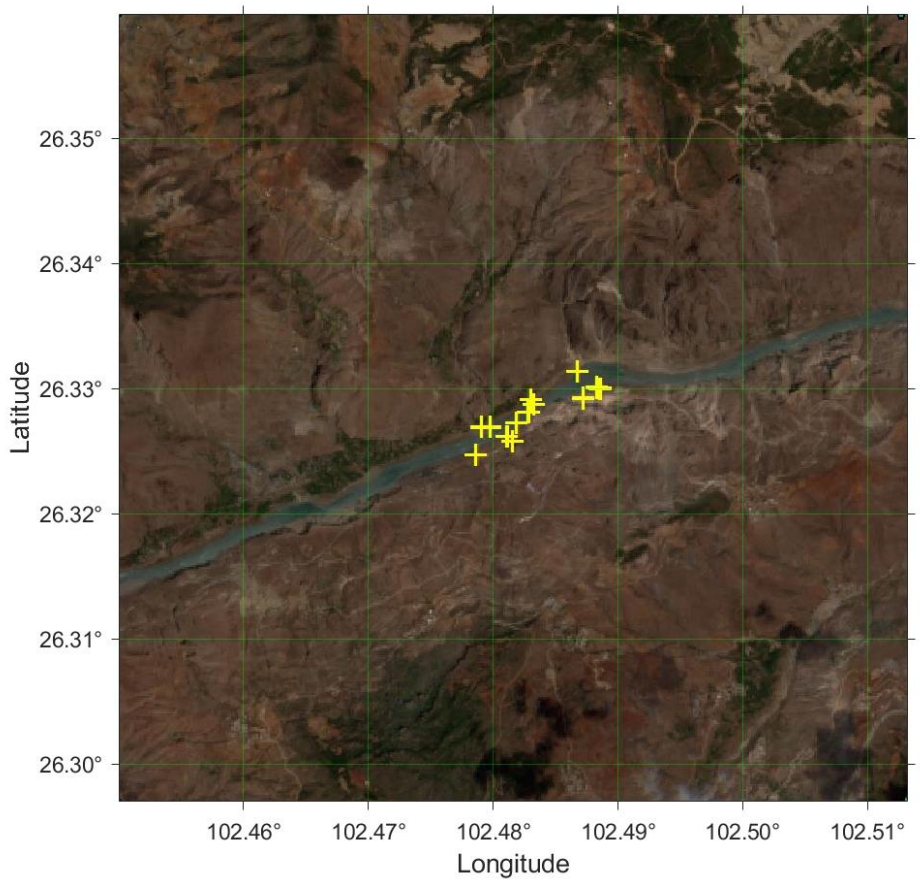

Figure 2.6: Part of the Jinsha River and the location of virtual station 8 (yellow cross)

People usually call the Yangtze River as Chang River in China. Yangtze is the old name for the downstream of the Chang River, covering the area from Nanjing to its estuary. Different from the upper reaches, the lower reaches are flat with an average elevation

of less than 500 meters. Beginning from Nanjing city, the river gradually gets wider (***Figure 2.7***) and develops towards the estuary in the shape of a trumpet. By the time it reaches the estuary, the river can achieve 80 kilometers wide.

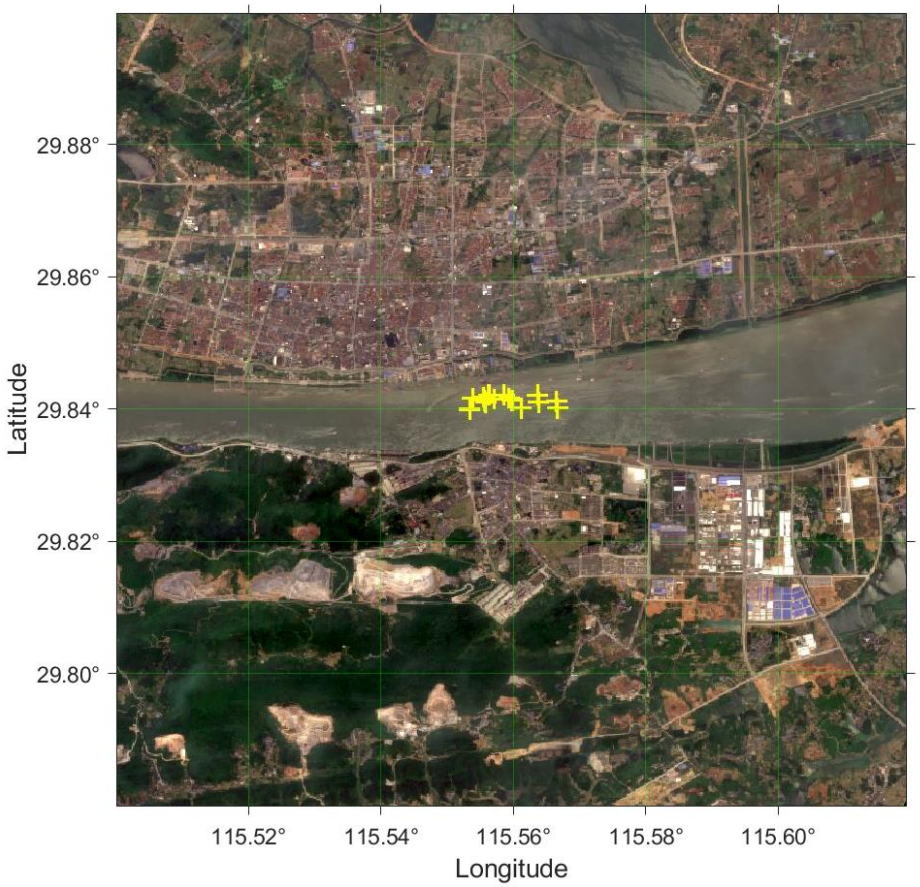

Figure 2.7: Part of the Yangtze River and the location of virtual station 15 (yellow cross)

2.3 Virtual station

A virtual station can be determined on an intersection point of the target river and the ground track of Sentinel-3 with a given search radius (5 km). Each time the satellite passes over the river, ground tracks have a slight drift to the set virtual station. As shown in ***Figure 2.8***, the yellow cross is the position of virtual station 8, blue lines indicate the drifted ground tracks. Different from the ocean application, in order to get more accurate range measurements and avoid hooking effect over inland water, water and land surfaces surrounding the virtual station are supposed to be distinguished by remote sensing images. Furthermore, the resolution of the along-track direction is about 330 meters while the width of rivers is in the same or a smaller magnitude, which means only one or two samples in each cycle can obtain the proper waveform from the river. Not only distinguishing the type of surfaces is important, but also, we should select the one sample data which is located nearest to the virtual station or the river.

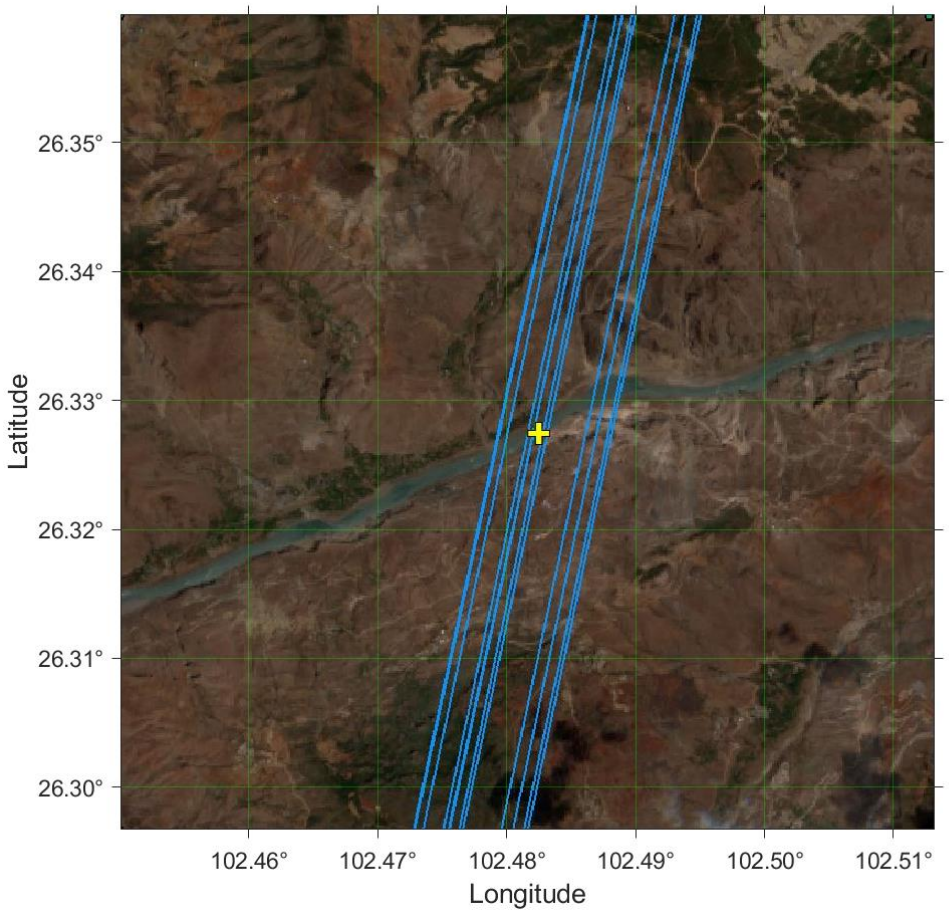

Figure 2.8: Schematic of Virtual Station 8

The description of the virtual station is present in ***Table 2.3***. The chosen station evenly distributed on two kinds of topography and the elevation surround it should be documented in on-board DEM table. Station 7 is located on a small tributary of the Yangtze River, and not recorded in the OLTC database. Therefore, the virtual station 7 didn't involve subsequent processing.

Table 2.3: Description of virtual stations

No.	Latitude	Longitude	Direction	Track	River
1	29.7454	95.0321	Ascending	53	Yarlung Tsangpo River
2	29.7475	95.1206	Descending	161	Yarlung Tsangpo River
3	29.9016	95.1615	Descending	161	Yarlung Tsangpo River
4	29.0439	93.3518	Ascending	324	Yarlung Tsangpo River
5	29.0397	93.0589	Descending	47	Yarlung Tsangpo River
6	29.2564	92.1823	Descending	375	Yarlung Tsangpo River
7	29.7493	95.9660	Ascending	110	Yangtze River

8	26.3227	102.4822	Ascending	67	Jinsha River
9	26.3344	102.6306	Descending	289	Jinsha River
10	27.4171	103.1350	Ascending	124	Jinsha River
11	28.9072	108.3504	Ascending	82	Yangtze River
12	26.6480	106.1244	Ascending	296	Yangtze River
13	25.7780	109.0320	Descending	303	Yangtze River
14	25.7328	109.1833	Ascending	82	Yangtze River
15	29.8363	115.5811	Ascending	153	Yangtze River

Chapter 3

Water level generation from altimetry data

Altimetry waveform can be directly obtained from satellite data, while the water level must be calculated by the altitude of the satellite, range measurements between the satellite and target water, and several corrections. The technique exploited to accurately acquire the range is referred to as waveform retracking. The results from three retracking methods: SAMOSA-3 retracker, Ice-sheet retracker and OCOG retracker, are used in this thesis. After accurate range measurement is determined, several geophysical and range corrections also should be applied to eliminate propagation errors and geophysical errors. In this chapter, we investigate the waveform and water levels of our target water bodies. More specifically, we introduce the principle of water level generation from satellite altimetry data and demonstrate its result of fourteen virtual stations.

3.1 Measuring principle

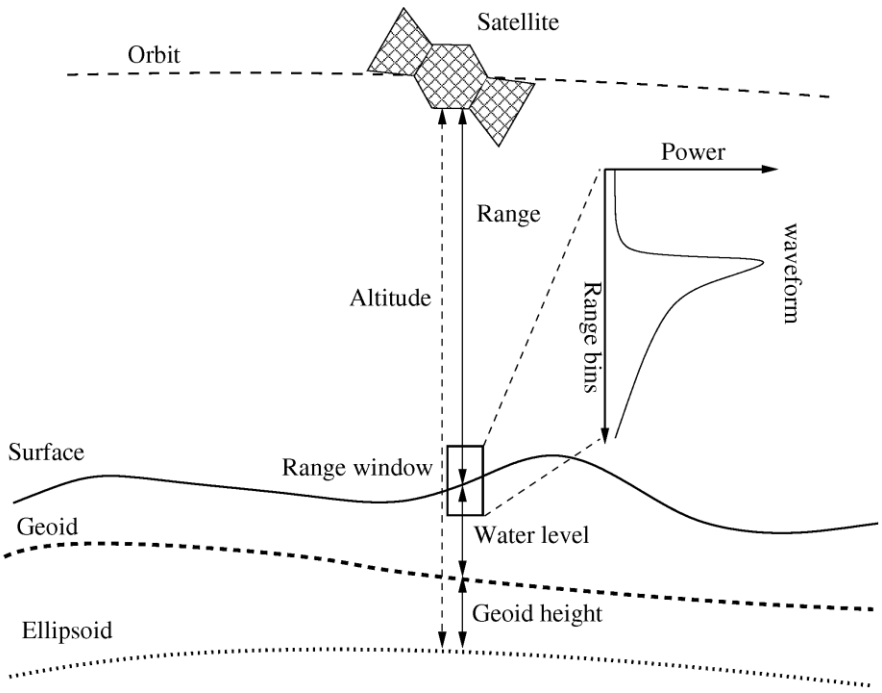

Figure 3.1: the principle of satellite altimetry measurement (Nielsen et al., 2017)

On-board radar altimeter transmits high-frequency signals toward Earth and receives the power returned from the surface. They referred to a time dependence measurement to make the round trip between the satellite and the surface. If this precise measurement

of round trip is recorded, the range measurements R, the one-way distance, can be determined. The Sea Surface Height (SSH) is the height of the sea surface with respect to a reference ellipsoid. ***Figure 3.1*** is the schematic of the satellite altimetry measurement principle and physical significance for each parameter.

3.1.1 Tracking system

As shown in ***Figure 3.1***, the position of range window (reception window) decides whether the altimeter properly receives the pulse from water. The position is set by the tracking system which is normally referred as a tracker. In other words, the tracker guarantees the quality of range measurements by controlling when and how altimeter acquiring return signal. It has two different tracking modes: the "Closed-Loop" mode (CL) and the "Open-Loop" mode (OL). CL, also called autonomous mode, requires the acquisition phase to set up altimeter's reception window. OL, also called Diode/DEM on altimeters, allows signal tracked inside reception window, contributes to prior parameters in on-board pseudo-DEM tables (Le Gac et al., 2019). OLTC is a new tracking technique applied for open-loop mode on Sentinel-3. It is capable of roughly evaluating the relative position between satellite and water targets, and accordingly setting the proper reception window based on elevation information recorded in on-board tables and navigation bulletin provided by DORIS system.

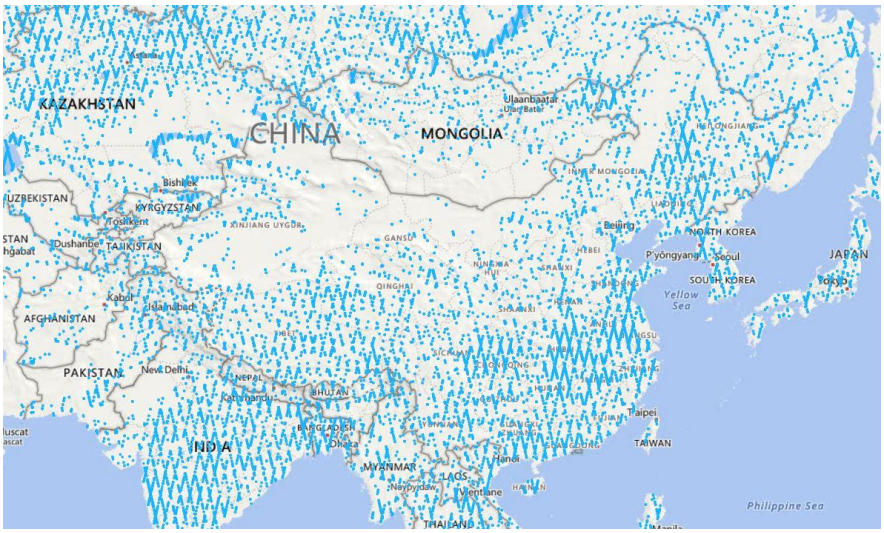

Figure 3.2: Hydrology Targets database defined for Sentinel-3B in China and its surrounding area (Credits: ESA)

ESA and its collaboration agency established an online database to collect hydrology targets data for OLTC application on Sentinel-3 mission (*https://www.altimetry-hydro.eu/*). Users from all over the world can contribute to this database. Sentinel-3A's latest upgrade on its OLTC on-board table was on March 9, 2019. Sentinel-3B upgraded its on-board table on November 27, 2018. There are more than thirty thousand hydrology targets recorded in Sentinel-3 on-board table which supports the altimeter acquiring high quality data.

Le Gac et al. (2019) compared the performance of open-loop and closed-loop by Sentinel-3B measurements. The result indicated that the success rate of retracking is significantly higher, especially for small lakes (from 67% to 84%) and rivers (63% to 83%). The small lakes and rivers are also the focus in this thesis. To improve the quality of data, we only exploited the measurement acquired in open-loop mode.

3.1.2 Water level calculation

The sea surface height can be calculated by (Dinardo, 2020):

$$SSH = Alt - \left(\frac{1}{2} \cdot c \cdot t_0 + \frac{1}{2} \cdot Tracker\_Delay + Cor_{sea}\right) \quad (3.1.1)$$

Where:

- SSH is the sea surface height
- Alt is the altitude of the satellite center of mass above the reference ellipsoid, it can be precisely acquired with the help of Doppler Orbitography and Radioposition Integrated by Satellite (DORIS) and Global Positioning System (GPS)
- c is the speed of light in vacuum
- $Tracker\_Delay$ is the two-way tracker time delay between the pulse transmission and reference tracking point, corrected by all the instrumental effects. It can be accurately acquired with the help of the tracking system
- Cor_{sea} is the range and geophysical correction over the sea. It will be introduced with more details in section 3.3

The inland water surface height (WSH) can be derived by:

$$WSH = Alt - \left(\frac{1}{2} \cdot c \cdot t_0 + \frac{1}{2} \cdot Tracker_{Delay} + Cor_{land}\right) \quad (3.1.2)$$

Where Cor_{land} is the range and geophysical correction over land. It will be elaborated in section 3.3 as well.

3.2 Improving range using waveform retracking

All altimeter data over different surfaces must be post-processed to generate accurate range measurements between satellite and water targets. This post-processing so-called waveform retracking is done by computing the departure of the waveform's leading edge from the altimeter tracking gate and offsetting the satellite range measurement error accordingly (***Figure 3.3***). In essence, waveform retracking aims at finding the mid-power point of leading edge and offsetting tracking gate to this point.

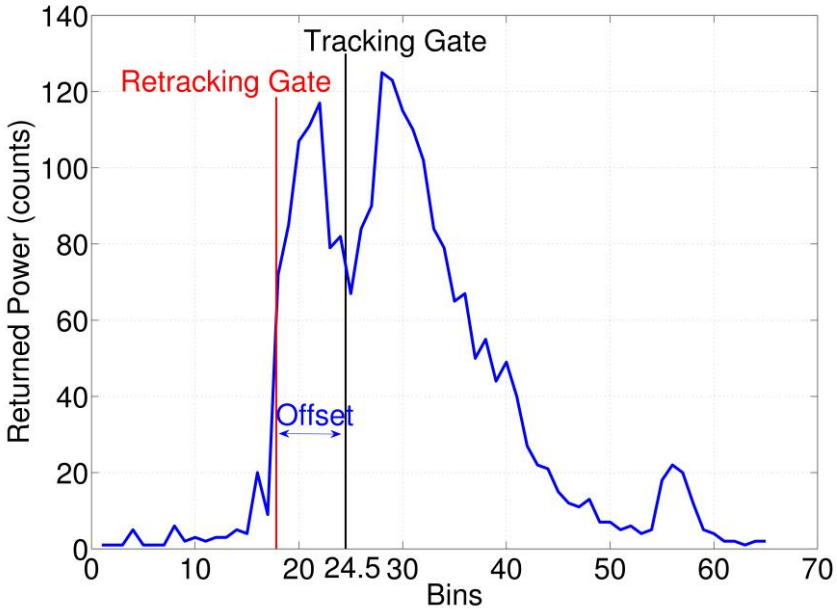

Figure 3.3: Schematic of waveform retracking (Tourian, 2012)

SRAL is a dual-frequency SAR altimeter, which we use for extracting inland water surface height in this thesis. There are four waveform retracking algorithms (retracker) for SRAL that are deputed to retrieve geophysical measurements for different types of surface:

- SAMOSA-3 retracker over open ocean and coastal zones
- Ice-Sheet retracker (MLE4) over ice sheets
- OCOG retracker over sea-ice margins
- Sea-Ice retracker over sea ice

Shu et al. (2020) indicated that Sea-Ice retracker was unable to be applied on inland water bodies, as the result of the high rate of missing data. Therefore, Sea-Ice retracker would not be introduced in this thesis.

3.2.1 SAMOSA-3 retracker

SAMOSA model is a compact closed-form model for the SAR altimetry return waveform from the ocean, developed within the framework of an ESA-funded project on the development of SAR Altimetry Mode Studies and Applications over the ocean, coastal zones and inland water (SAMOSA).

SAMOSA-3 is an ocean retracking model in SAMOSA project which assumes Ocean Gaussian statistics and is sensitive to surface roughness (Jain, 2014). Model's parameters are waveform epoch t_o, significant wave height SWH, Pu waveform amplitude Pu, surface RMS slope, skewness and mis-pointing angles. The Doppler Frequency

and the Time Delay are the model's independent variables (Dinardo, et al. 2015). It has two different operating modes involving waveform fitting: the Lead mode which fits retracking position and roughness; the Ocean fits significant wave height and retracking position.

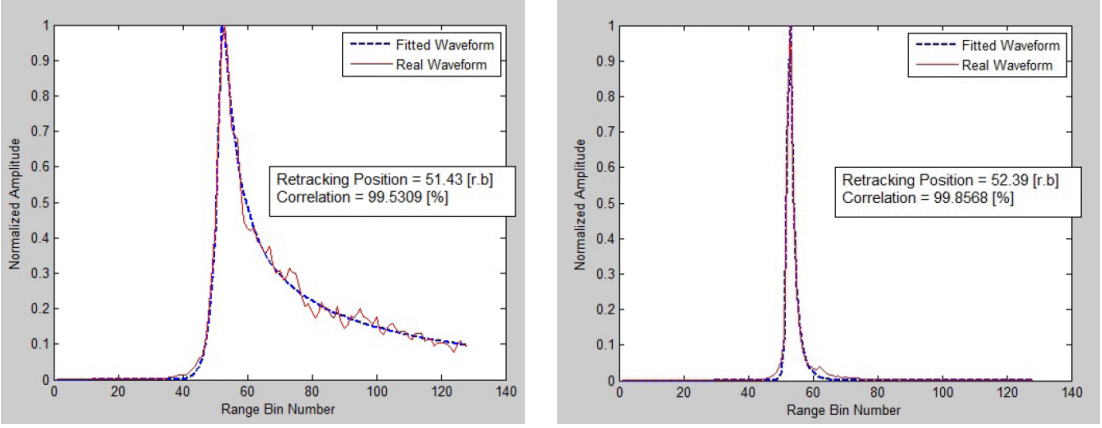

Figure 3.4: Waveform fitting in Ocean (left) mode and Lead (right) mode (Jain, 2014)

Normally, the surface discriminator flag (recorded in altimetry measurements) is used to decide in which mode to operate the retracker. In Jain et al.'s (2014) research, this flag has shown several false alarms in processing. Thus, they based on the Pearson correlation coefficient to determine the operating mode. ***Figure 3.4*** shows the waveform fittings in Ocean Mode and Lead Mode, retracking position can be used to derive the mean sea level.

3.2.2 Ice-sheet retracker (MLE4)

The Maximum Likelihood Estimation of the 4th order (MLE-4) retracking algorithm is an analytic return power model to make the measured waveform coincide, according to weighted Least Square Estimators derived from Maximum Likelihood Estimators, and to estimate the 4 following parameters (ESA, 2010):

- Epoch is associated with the position of the waveform in the analysis window, from which the altimeter range is derived, accounting for the tracker range.
- Composite Sigma is associated with the width of the waveform leading edge, from which the significant wave height (SWH) is derived, accounting for the width of the Point Target Response.
- Amplitude of the waveform, from which the backscatter coefficient and the wind speed are derived, accounting for the radar equation.
- Square of the off-nadir angle is associated with the slope of the waveform trailing edge.

3.2.3 Off Center of Gravity (OCOG) retracker

OCOG is an empirical retracking algorithm appropriate to topographic surfaces developed by Wingham et al. (1986). It calculates the center of gravity (COG) of a rectangular box, the twice the height of the center of gravity (amplitude A) which determines the length of the box, and the width of the box (W) which determines the retracking gates (***Figure 3.5***).

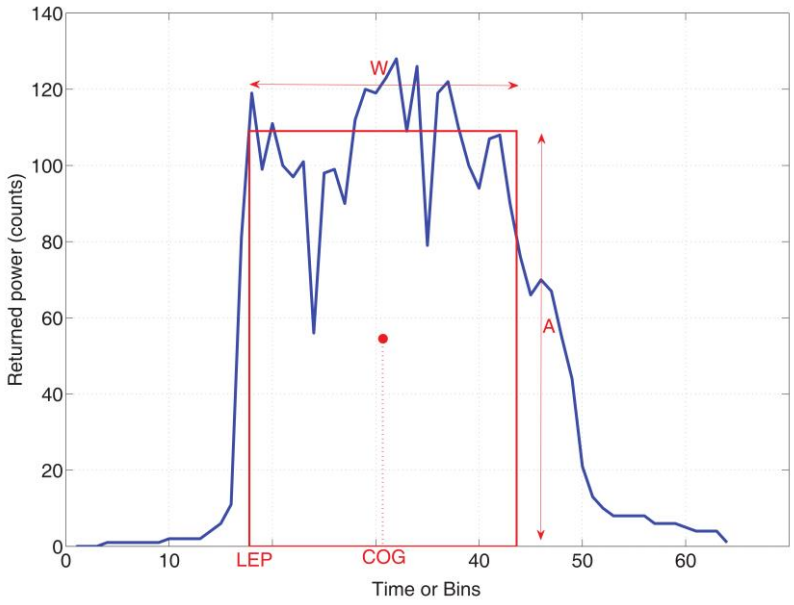

Figure 3.5: Schematic description of the OCOG retracker (Tourian, 2012)

For a range window of N bins samples $P(n)$,

$$COG = \sum_{i=1+n_a}^{N-n_a} iP^2(i) \Big/ \sum_{i=1+n_a}^{N-n_a} P^2(i) \qquad (3.2.1)$$

$$A = \sqrt{\sum_{i=1+n_a}^{N-n_a} P^4(i)} \Big/ \sqrt{\sum_{i=1+n_a}^{N-n_a} P^2(i)} \qquad (3.2.2)$$

where N is the number of samples in the reception window, n_a is the number of bins influenced by aliasing, and $P(i)$ is the waveform sample power at i^{th} bin. The width estimate is then computed by requiring that the product $2AW$ should equal the total area of the pulse:

$$W = \sqrt{\left(\sum_{i=1+n_a}^{N-n_a} P^2(i)\right)^2} \Big/ \sqrt{\sum_{i=1+n_a}^{N-n_a} P^4(i)} \qquad (3.2.3)$$

The Leading Edge Position (LEP) can be given by:

$$LEP = COG - \frac{W}{2} \quad (3.2.4)$$

3.3 Correction parameters

Range measurements are generated after waveform retracking. However, several corrections are included in altimeter range measurements which would result in the bias of water surface height. The corrections fall into two groups (Vignudelli, et al., 2001). Range corrections adjust the speed of radar signals when it propagates through a non-vacuum medium and actual scattering surface of the radar pulse. Geophysical corrections prevent the largest time-variable contributors such as ocean tide and pole tide from disturbing altimeter observe only purely water topographic dynamics.

Corrections for sea surfaces can be indicated as:

$$Cor_{sea} = Tropo_{dry} + Tropo_{wet} + Iono_{delay} + equi_{tide} + longperiod_{tide} + load_{tide} + dyn_{atm} + soildearth_{tide} + pole_{tide} + SSB \quad (3.3.1)$$

Where:

- $Tropo_{dry}$ is the dry tropospheric correction
- $Tropo_{wet}$ is the wet tropospheric correction
- $Iono_{delay}$ is the ionospheric delay
- $equi_{tide}$ is the ocean equilibrium tide
- $load_{tide}$ is the ocean loading tide
- $longperiod_{tide}$ is the ocean long period equilibrium tide
- dyn_{atm} is the dynamic atmospheric correction
- $soildearth_{tide}$ is the geocentric tide
- $pole_{tide}$ is the geocentric polar tide
- SSB is the sea state bias

Since most of inland water bodies are closed systems, ocean dynamic corrections and sea state bias are not applied in the calculation. Hence, Cor_{sea} can be simplified as:

$$Cor_{land} = Tropo_{dry} + Tropo_{wet} + Iono_{delay} + soildearth_{tide} + pole_{tide} \quad (3.3.2)$$

Correction models applied for altimetry measurements in this thesis (Sentinel-3) are shown as ***Table 3.1*** (Gao, et al., 2019):

Table 3.1: Range and Geophysical corrections for the Sentinel-3 Level-2 product

Correction	Model	Variable for level-2 product
Dry troposphere	ECMWF model	Mod_dry_tropo_cor_meas_altitude_01
Wet troposphere	ECMWF model	Mod_wet_tropo_cor_meas_altitude_01
Ionosphere	Global Ionospheric Map	Iono_cor_gim_01_ku
Solid earth tide	Cartwright model	Solid_earth_tide_01
Geocentric polar tide	Historical pole location	Pole_tide_01
Ocean loading tide	GOT00.2 model	Ocean_tide_sol1_01

3.4 Time series

After waveform retracking and several corrections, water heights within the search radius (5 km) are generated. As mentioned in section 2.3, we are also supposed to select the appropriate waveform and water height from each cycle to improve the accuracy of the measurement. With the help of Sentinel-2 images, we located the position of each waveform and height results, then selected the one which is the closest to the river and virtual station as the result for each cycle.

Selected time series of fourteen virtual stations are demonstrated as below. Some absent results in some cycle represent failure retracking.

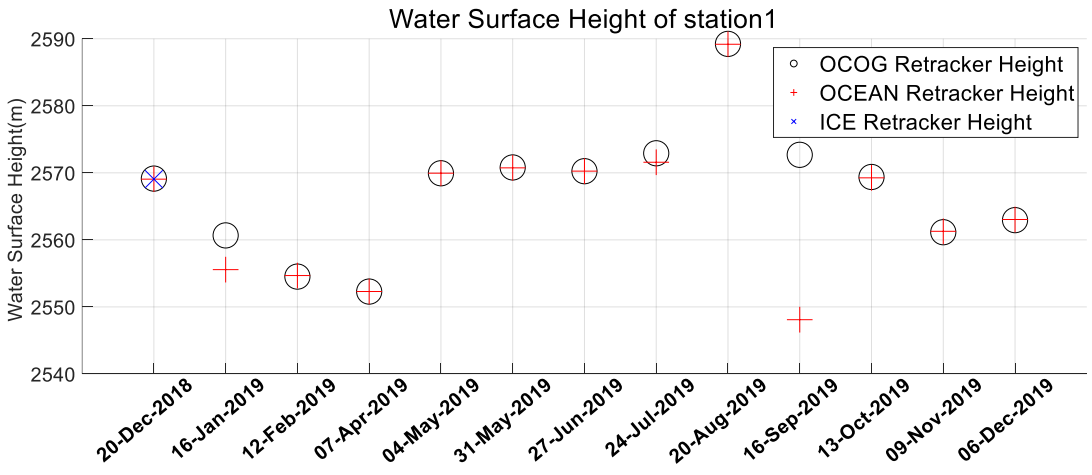

Figure 3.6: Time series of virtual station 1

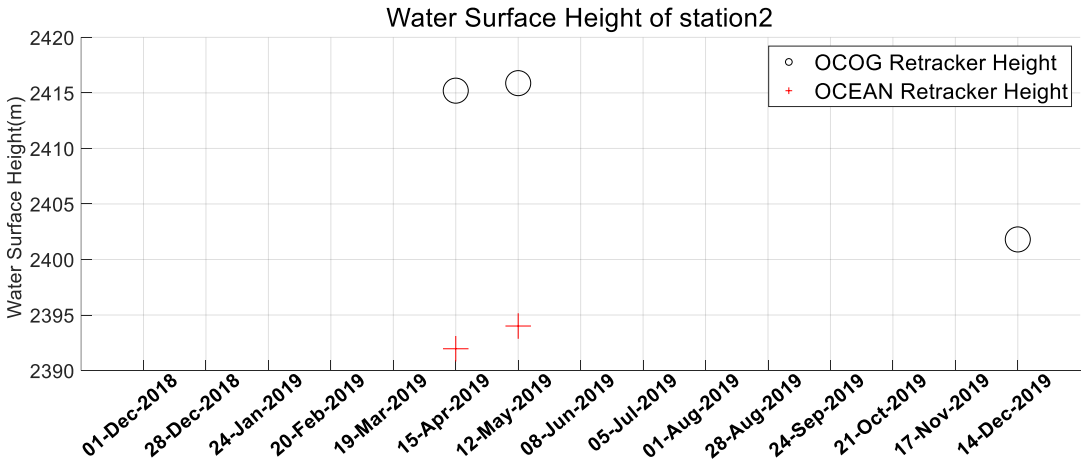

Figure 3.7: Time series of virtual station 2

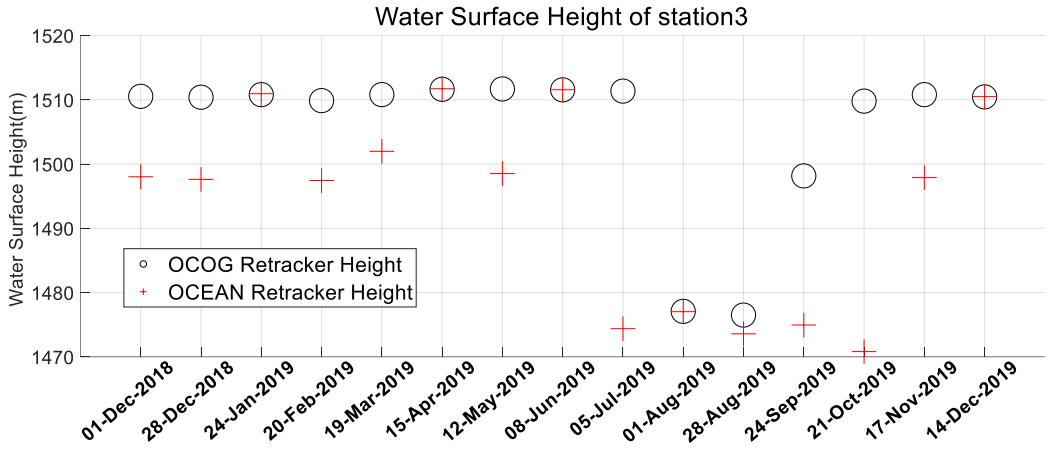

Figure 3.8: Time series of virtual station 3

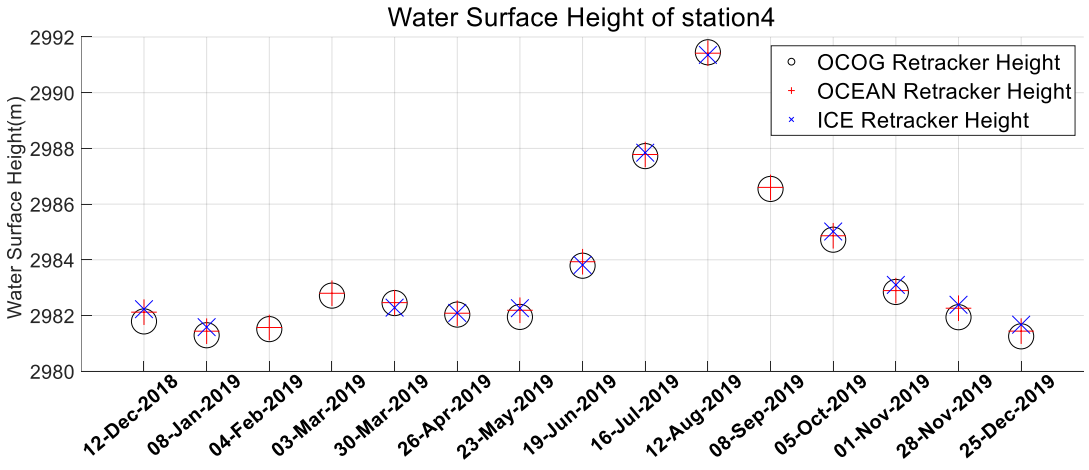

Figure 3.9: Time series of virtual station 4

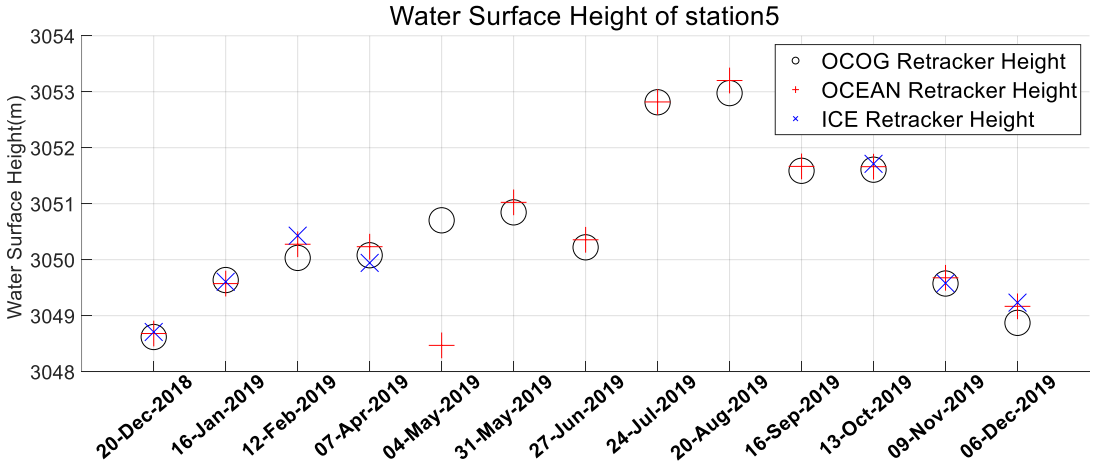

Figure 3.10: Time series of virtual station 5

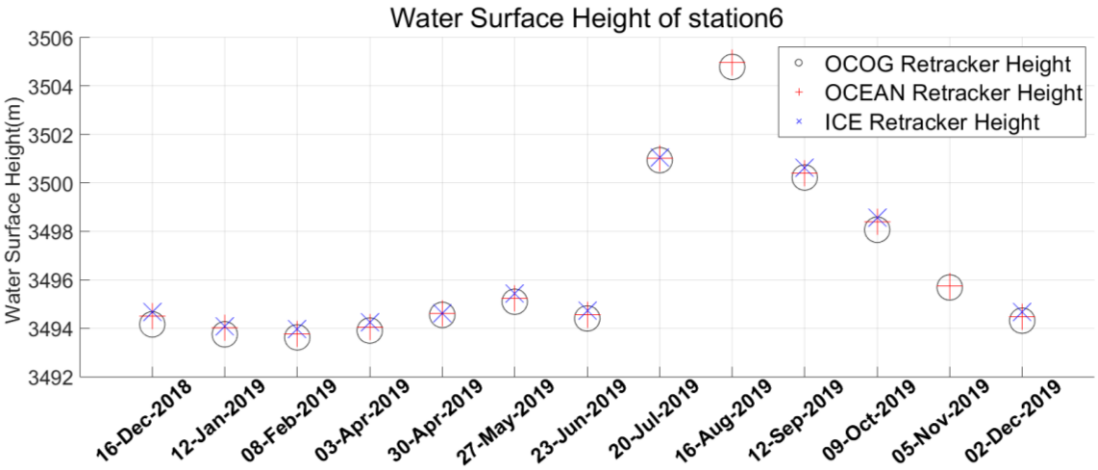

Figure 3.11: Time series of virtual station 6

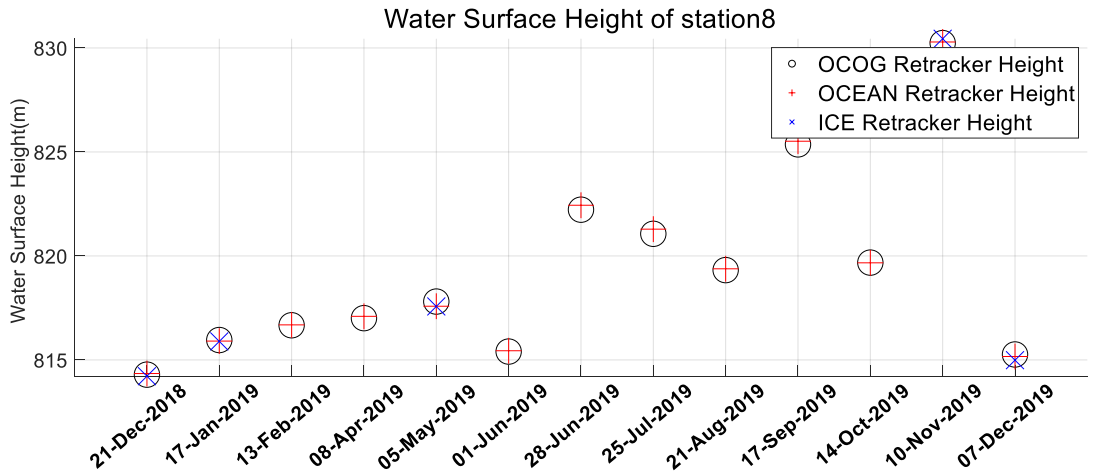

Figure 3.12: Time series of virtual station 8

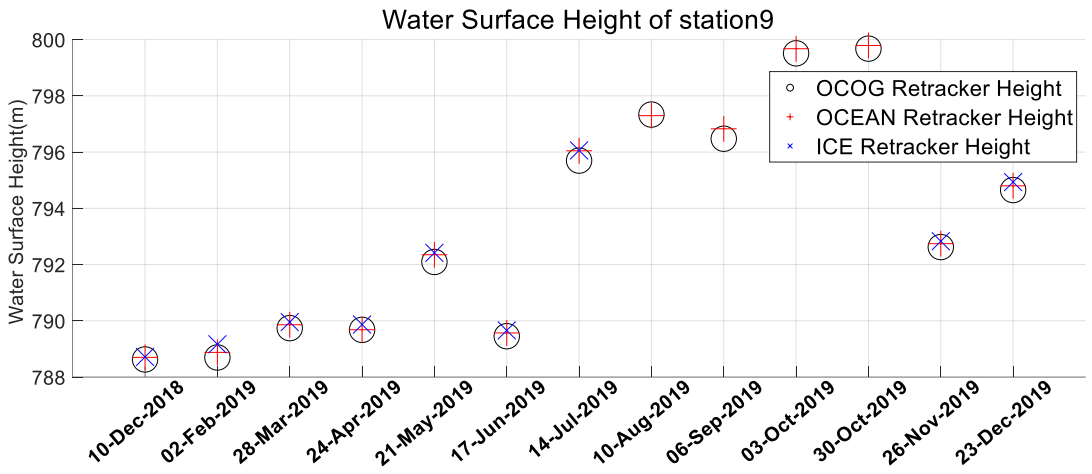

Figure 3.13: Time series of virtual station 9

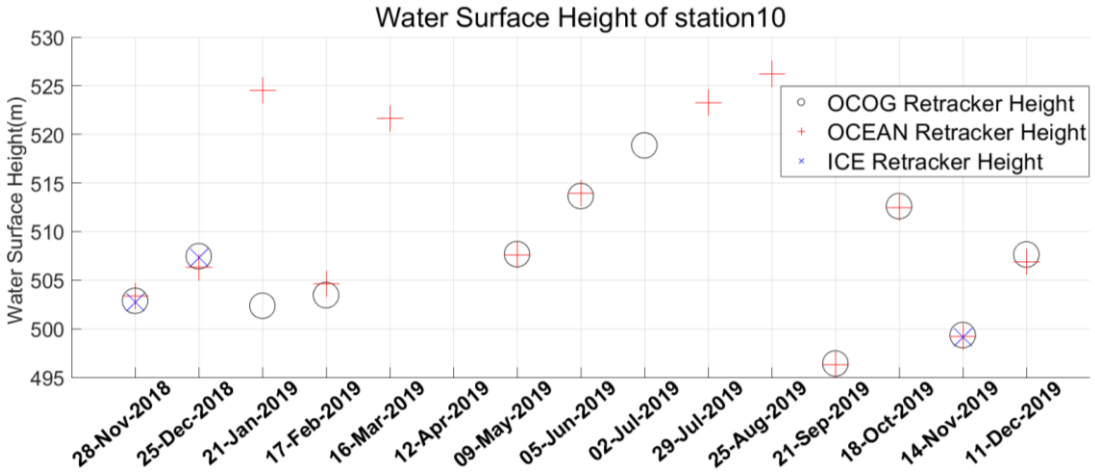

Figure 3.14: Time series of virtual station 10

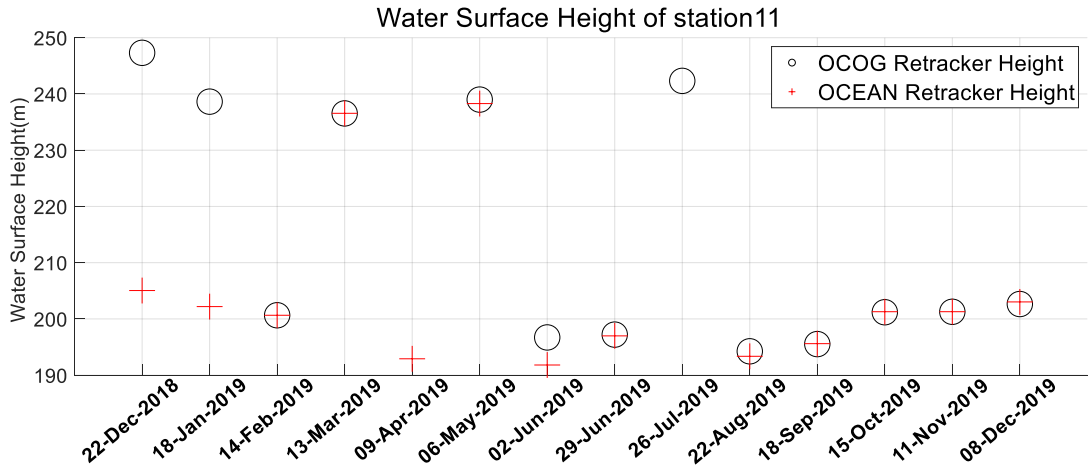

Figure 3.15: Time series of virtual station 11

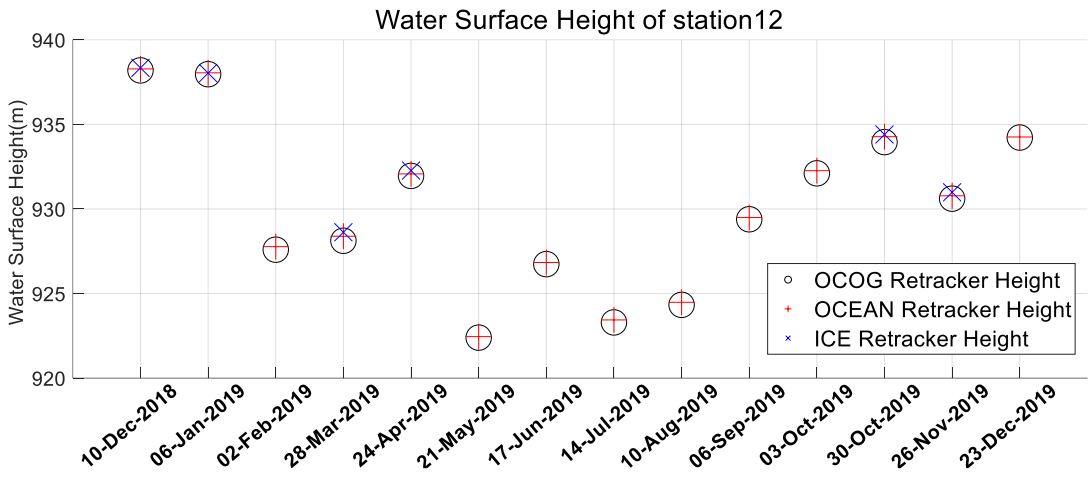

Figure 3.16: Time series of virtual station 12

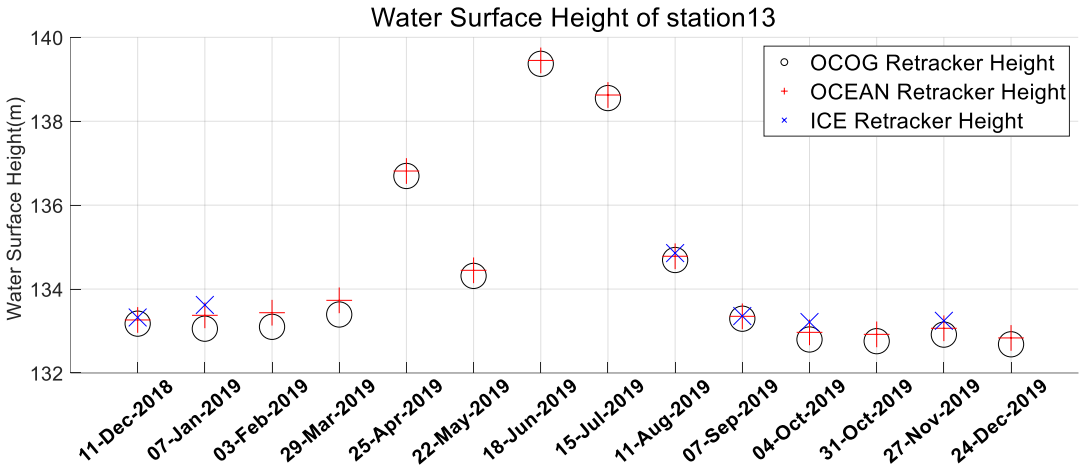

Figure 3.17: Time series of virtual station 13

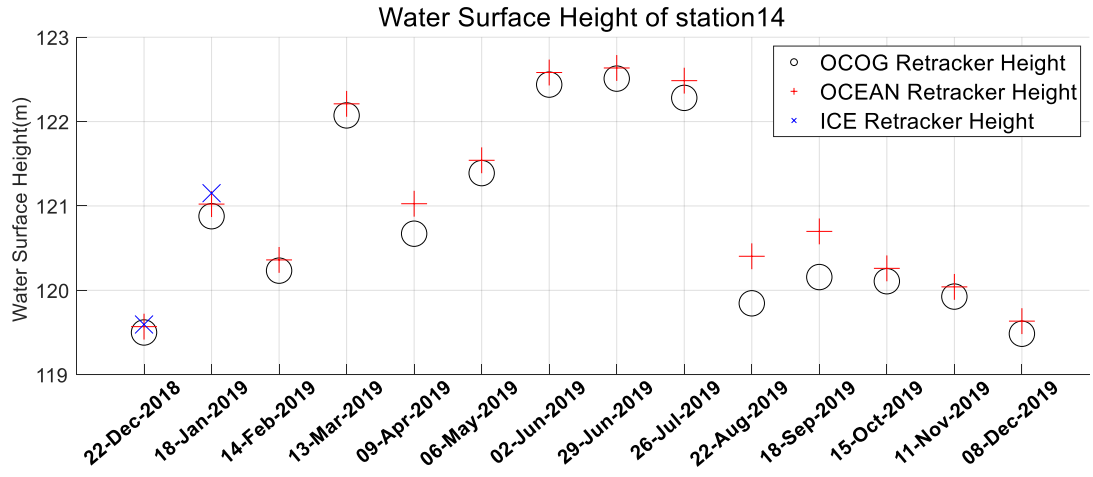

Figure 3.18: Time series of virtual station 14

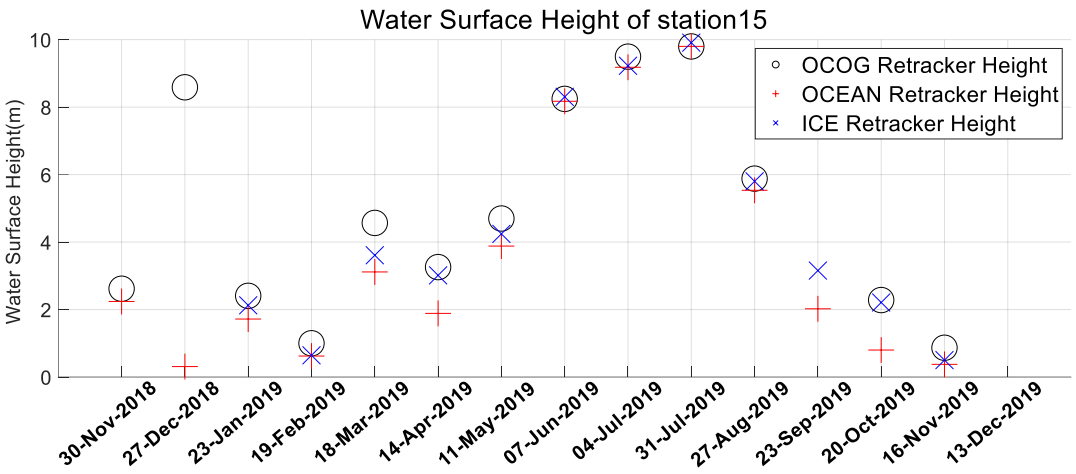

Figure 3.19: Time series of virtual station 15

In the above figures, three types of results can be identified:

- The first type of waveform can be corrected by three retrackers, and their height results are close to each other except waveforms obtained from the fifth, sixth, and fourteenth cycle in virtual station 15. The comparison between these exceptions in station 15 and other waveforms belong to the first type are shown in ***Figure 3.20***. The first figure shows a specular waveform and the second figure shows a flat patch waveform. These two kinds of waveforms correspond to the similar height results we mentioned above. The third and last figure show Brown waveforms, which produced different results from the three retrackers.

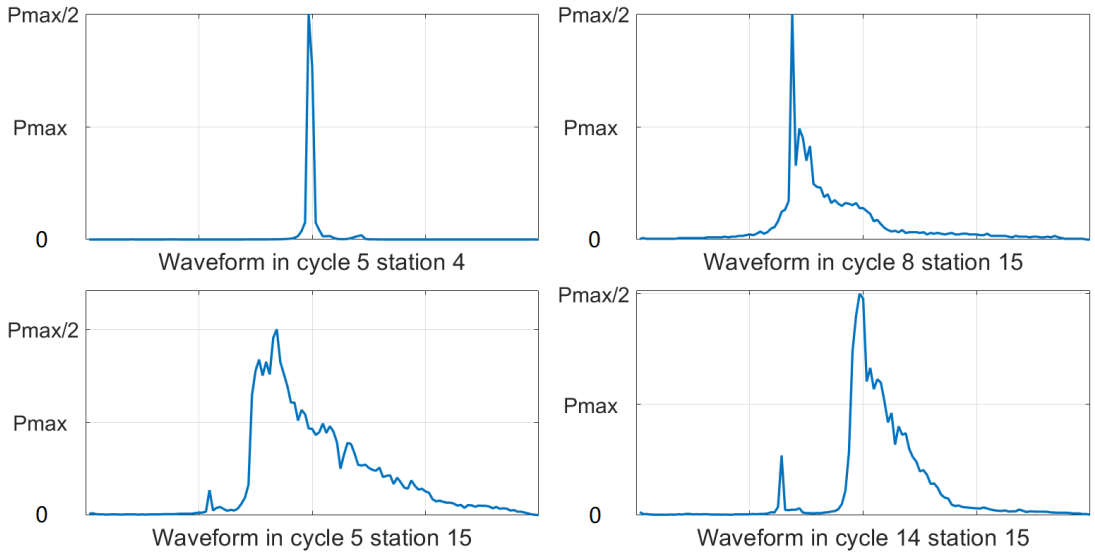

Figure 3.20: Comparison of waveforms which successful retracked by three methods, the first figure shows a specular waveform and the second figure shows a flat patch waveform, the third and last figures show Brown waveforms

- The second type of waveform can be corrected by OCOG retracker and Ocean retracker (SAMOSA 3). Similar to the first type, different kinds of waveform influence the difference between OCOG retracker height and Ocean retracker height. The first two figures in ***Figure 3.21*** show specular waveforms corresponding to small differences and the last two figures show complex waveforms which result in large differences. In cycle 13 of station 3, the largest peak appears at the end of the waveform. Its height difference even achieves 40 meters. That means OCOG retracker considers the left side of the peak in the middle as leading edge while Ocean retracker considers the left side of the highest peak as leading edge.

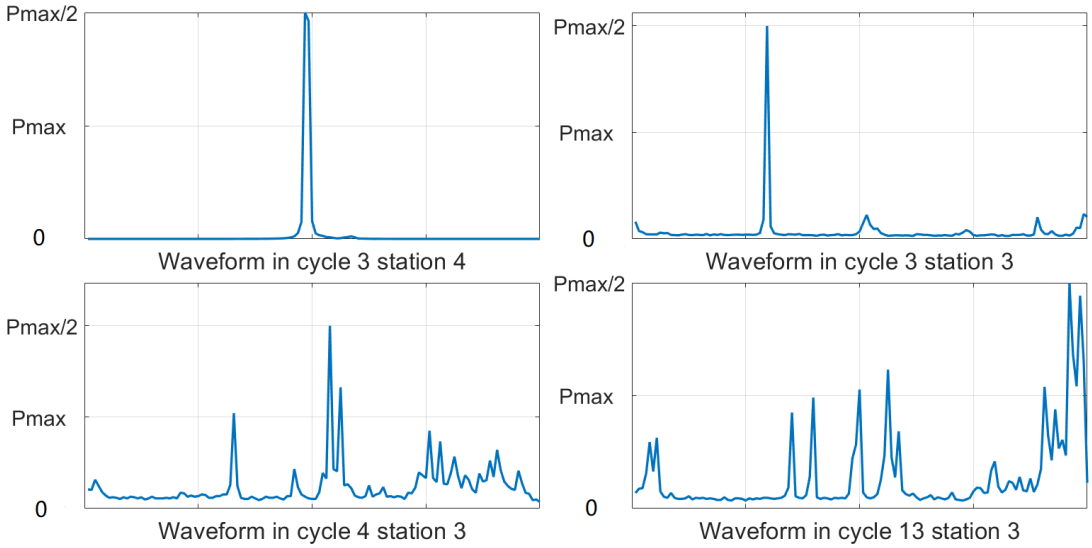

Figure 3.21: Comparison of waveforms which successful retracked by two methods, the first two figures show specular waveforms and the last two figures show complex waveforms

- The third type of waveform can only be offset by one retracker. The top figure in ***Figure 3.22*** presents a flat patch waveform that can be retracked by Ocean retracker. The bottom figure presents a specular waveform that can be retracked by OCOG retracker. The peaks in both figures appear at the beginning of the waveforms, which may be rejected by some retracker, further resulting in a failure retracking. It also indicates the on-board DEM document is not precise enough to support river application in some regions.

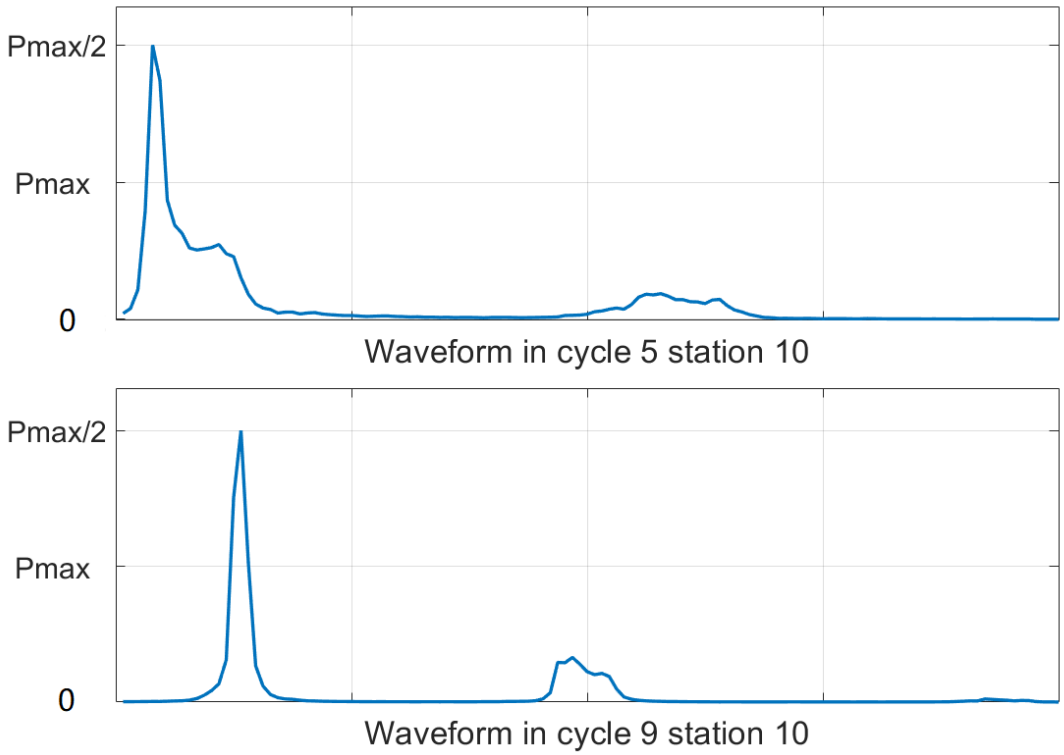

Figure 3.22: Comparison of waveforms that successful retracking by one method. The top figure presents a flat patch waveform can be retracked by Ocean retracker, the bottom figure presents a specular waveform can be retracked by OCOG retracker

All analyses above are merely based on the shape of the waveform. There are lots of phenomena that can't be precisely interpreted, such as two similar specular waveforms, one can be retracked by Ice-sheet retracker, but the other cannot. Therefore, to describe more details about the waveform and establish a connection between it and the environmental condition, we still ought to parameterize the waveform.

Chapter 4

Altimetry uncertainty analysis

As mentioned in Chapter 1, two sorts of features are supposed to be parameterized, namely waveform indicator and environmental indicator. Waveform indicators describe the characteristics, which are related to generating the water level height. Noise level of the waveform, for instance, bias the arrival time and the rise time which can lead to errors in range measurements (Sandwell & Smith, 2005). These waveform indicators can be derived from waveforms which are determined in Chapter 3. Environmental indicators describe the conditions of the surface where the transmitted pulse reflected from. Two kinds of data, which are remote sensing images and digital elevation model (DEM), are involved in the extraction of environmental indicators. Properties of the target river and the surface type within the footprints can be determined by remote sensing images. The topography surrounding the virtual station can be evaluated by DEM documents. In this chapter, we will perform the methodology of indicators extraction.

4.1 Waveform indicators extraction

4.1.1 Thermal Noise

The thermal noise power of waveform is generated by the altimeter prior to receiving an echo from the scattering surfaces. It can be identified as the background noise of the whole waveform and treated as a constant level. In general, we can extract it from the first segment of the waveform.

As we introduced in section 3.1.1, new tracking mode OLTC is capable of controlling the time to receive the returned waveform supported by on-board DEM document. In some complicated topography, this DEM may not fully coincide with the real landscape because of the on-board DEM storage's limitation. As a consequence, the reception window does not correspond exactly with the return time of scattered pulses, leading to a shifted waveform. It is shown in the following figure.

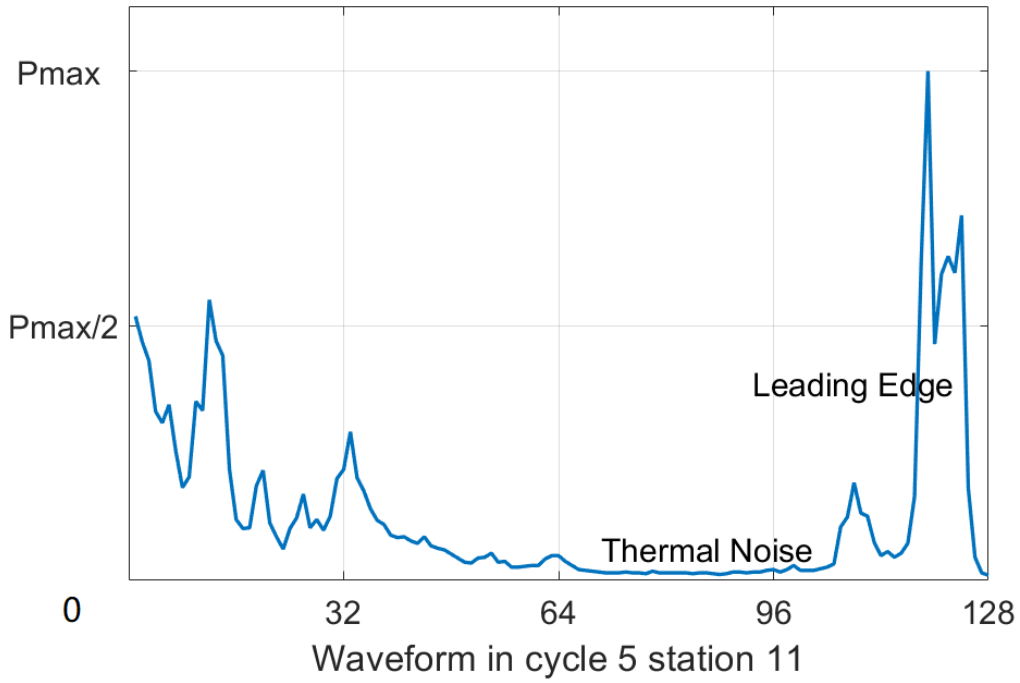

Figure 4.1: Waveform obtained from Virtual Station 11, cycle 5. The thermal noise (background noise) segment doesn't appear at the beginning of the waveform.

The thermal noise segment (background noise) appears in the middle part of the waveform instead of the beginning part. Meanwhile, the method to extract thermal noise should be adjusted. We firstly ascending ranked 128 power values in a waveform and obtained an ascending sequence. Then taking the median of first 40 power values in the sequence as the thermal noise of this waveform.

4.1.2 Peak properties

Most information on a waveform is contained in its leading edge and peaks. The property of the peak is associated with the height result. However, property extraction is not an easy task because it is complicated to identify the individual peaks of a complex waveform. Hence, we set the thermal noise as the threshold and determined the individual peak and its properties according to follow rules:

- Smoothing the waveform to eliminate the jagged noise on waveform
- Calculate the derivative of smoothed waveform with respect to the time (Bins)
- Take the increasing interval and decreasing interval as the leading edge and trailing edge of one peak. Choose the first point of leading edge whose value is larger than two times of the threshold (the multiple might change for different kinds of waveform) as the beginning of the peak. The end of the peak is the first point whose value is smaller than two times of threshold
- Select the peaks whose maximum power are larger than one-third of the maximum power of the whole waveform

- Record the number of selected peaks, the position of each peak, crest power of each peak and their width

An extraction example is shown in ***Figure 4.2***:

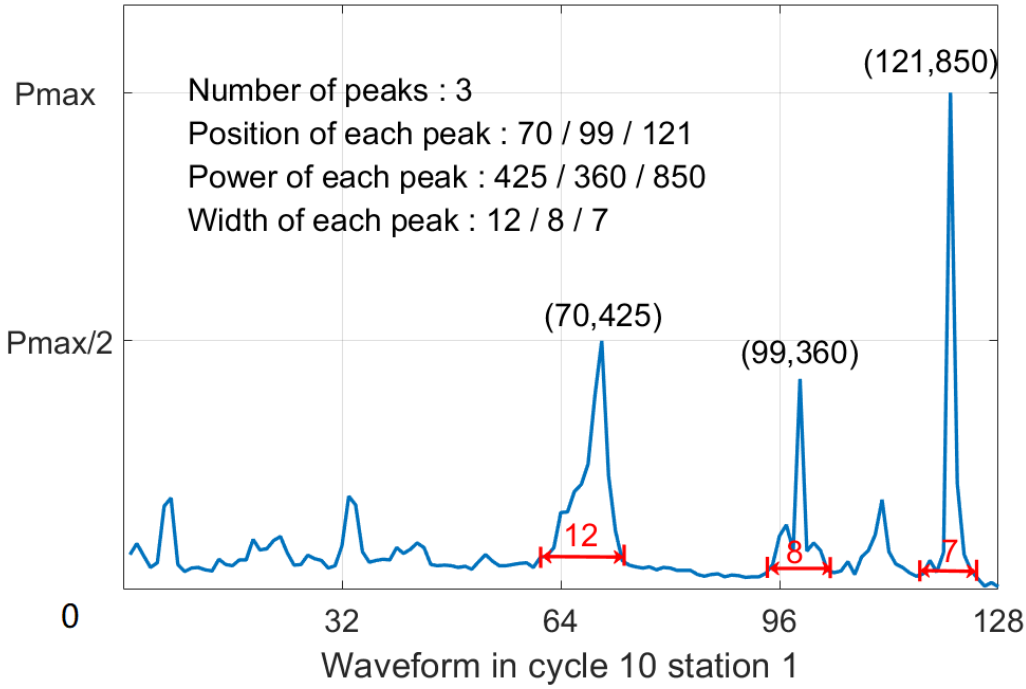

Figure 4.2: An example of peak property extraction

Peakiness is a ratio of the maximum waveform power to the sum of the power of all bins, which describes how sharp the waveform is. It can be calculated by:

$$Peakiness = \frac{Max(W_i)}{\sum_{i=1}^{n} W_i} \tag{4.1.1}$$

where W_i is the power on i bin, n is the number of sample data in a waveform.

Kurtosis is a measure of the tailedness of the probability distribution of a real-valued random variable. It describes the shape of a probability distribution. High kurtosis represents the increasing variance caused by low-frequency peak or crest value. In general, kurtosis can be computed by:

$$Kurtosis = \frac{\frac{1}{n}\sum_{i=1}^{n}(W_i - \overline{W})^4}{(\frac{1}{n}\sum_{i=1}^{n}(W_i - \overline{W})^2)^2} - 3 \tag{4.1.2}$$

where $\overline{W}$ is the mean value of waveform powers.

4.1.3 Noise level

The altimetry waveform also contains various kinds of noise except the thermal noise, especially the waveform obtained from a complicated surface. It can bias the arrival time and the rise time which results in the error in range measurements. To evaluate the noise level, we initially smooth the waveform by applying a smooth filter. The length of the filter is 3 or 5 bins based on the shapes of waveforms. It is executed from the left side of the waveform to the right side. Each value in the center of the filter is replaced by the median of the values within the range of the filter. After smoothing, we calculate the difference between the smoothed waveform and the original waveform. The normalized noise level is the root mean square of these differences:

$$Noise\ level = \sqrt{\frac{\sum_{i=1}^{n}(W_i - S_i)^2}{n}} \tag{4.1.3}$$

$$Normalized\ noise\ level = \frac{Noise\ level}{Max(W_i)} \tag{4.1.4}$$

where S_i is the power on i bin of smooth waveform.

However, the peak value is removed when we apply a smooth filter on the waveform with high peakiness. As shown in ***Figure 4.3***, the red line is waveform after smoothing. The peak value that can lead to a wrong noise level has been replaced by a median value.

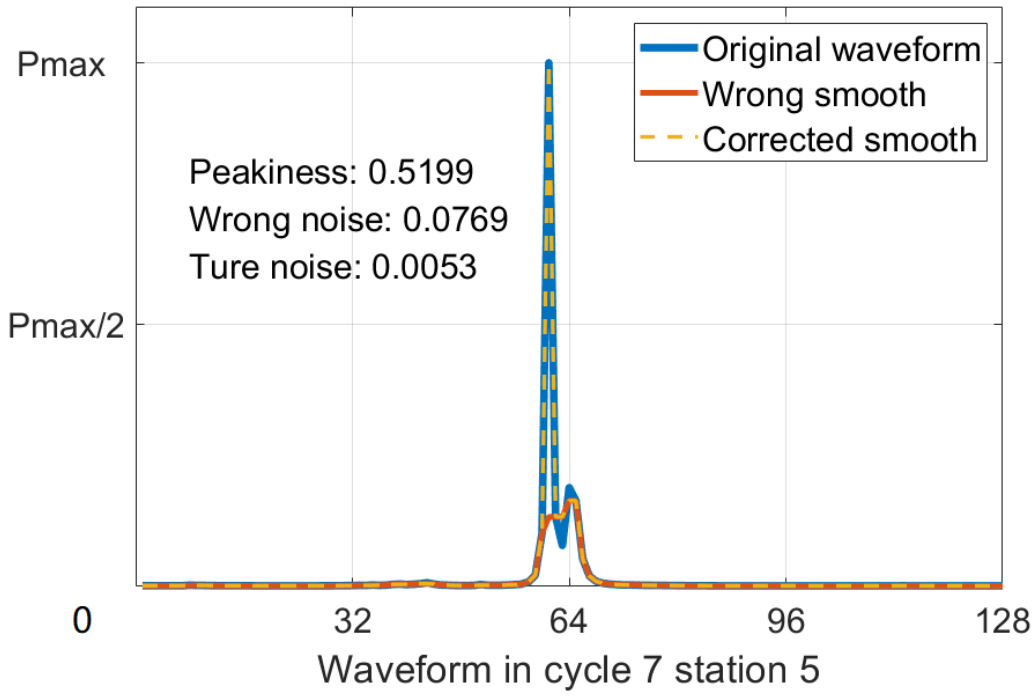

Figure 4.3: Peak value would be removed when we applied a smooth filter on a high peakiness waveform

Therefore, it is decided to set a judgment condition before smoothing the waveform. If the peakiness is higher than 0.3, the peak value in the smooth waveform keeps the same

value to that in the original waveform. The orange dash line in ***Figure 4.3*** is the corrected smooth waveform, the corresponding noise level of which is much smaller than the wrong one.

4.2 Environmental indicators

Two preparatory works should be performed before deriving the environmental indicators. Determining footprints which are the scattering surface of the selected waveform is the initial task. However, it is difficult to delimit a certain boundary of footprints over inland water since its effective size is influenced by the topography and the location of the satellite. For example, transmitted pulses may be blocked by mountains and thus decreasing the size of effective footprints when the altimeter flies over a water body located in the mountainous area. Since the actual footprints can be obtained, we assumed a footprint that is rectangular with a length of 8 km and a width of 330 m (***Figure 4.4***). The assumed footprint is obviously longer than the effective one. It will be adjusted by adding a threshold base on the topography situation. The specific operation will be introduced in the following section.

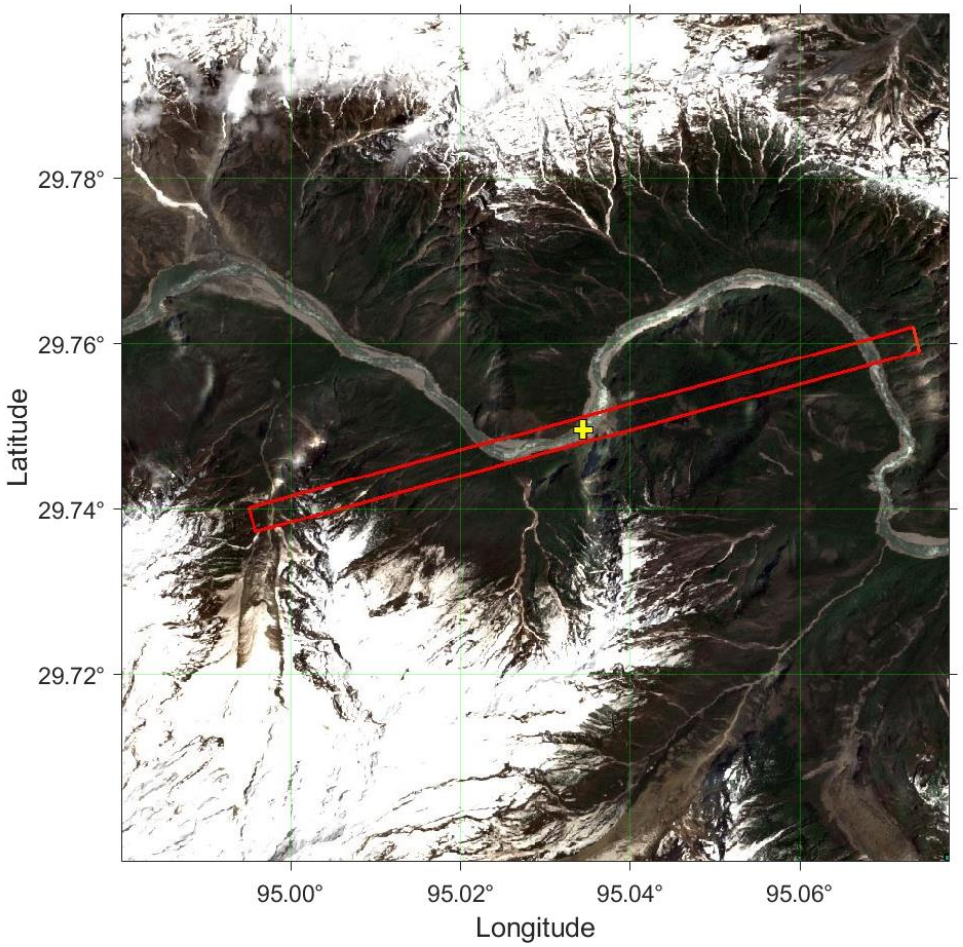

Figure 4.4: Footprints of virtual station 1 cycle 11

Another preparation is to check whether remote sensing images are sufficient to the

following requirements. Each image has its own corresponding waveform. To guarantee the validity of images, the difference of acquisition time between images and waveform should be less than ten days. Meanwhile, the target river must be observed clearly. Landsat-8 images can be an alternative if the river in Sentinel-2 images is covered by clouds or shadow. After footprints determination and image check, three types of environmental indicators are set for generation.

4.2.1 Topography

The DEM data used in this section is a grid map that consists of 3-dimension points (latitude, longitude, elevation). Two parameters can be derived from DEM documents. One is elevation variance of whole footprints, and the other is the elevation difference around the river. The first parameter describes the general variation of the elevation. Choosing the point within the boundary of footprints, elevation variance can be evaluated by the root-mean-square of the difference between the true elevation E_i and the mean elevation $\bar{E}$:

$$\bar{E} = \frac{\sum_{i=1}^{n} E_i}{n} \tag{4.2.1}$$

$$Elevation\ variance\ = \sqrt{\frac{\sum_{i=1}^{n}(E_i - \bar{E})^2}{n}} \tag{4.2.2}$$

where n is the number of data points within the footprints.

The elevation difference indicates how rapidly the elevation changes around the river. Part of the satellite track must overlap with the river in each footprint. The rest of the track should also be vicinity of the river. The gradient along the satellite track can be used to evaluate the elevation difference around the river. Thus, we interpolate the elevation value on the satellite track. The along track gradient and the elevation difference can then be computed by:

$$\nabla E'_i = \frac{E'_i - E'_{i-1}}{d_i} \tag{4.2.3}$$

$$Elevation\ difference = \sqrt{\frac{\sum_{i=1}^{n}\left(\nabla E'_i - \overline{\nabla E'}\right)^2}{n}} \tag{4.2.4}$$

where E'_i is the elevation value, which is interpolated on the track, n is the number of elevation values interpolated on the track.

4.2.2 Shape of river

Five parameters, including area, length, average width of the river, crossing angle between the river and the satellite track, and the number of individual water bodies, are

generated in this section. Water area extraction from the remote image is a mature technology that has been used for many years. We execute the classification by calculating the modification of normalized difference water index (MNDWI). It is a band operation method which can enhance open water features while efficiently suppressing the noise from other ground objects. This index is expressed as follow (Xu, 2007):

$$MNDWI = \frac{Green - MIR}{Green + MIR} \tag{4.2.5}$$

where $Green$ is a green band such as Sentinel-2 MSI band 3 (OLI band 3), MIR is a middle infrared band such as MSI band 11 (OLI band 6).

After executing the band operation, we obtain the mask of the river area. ***Figure 4.5*** is an example of water extraction. The white mask in the center is the extracted water area and the red rectangular is the assumed footprints. The number of individual water bodies can be counted from the mask as well. We then transform this mask to a polygon shapefile documents in order to post-processing.

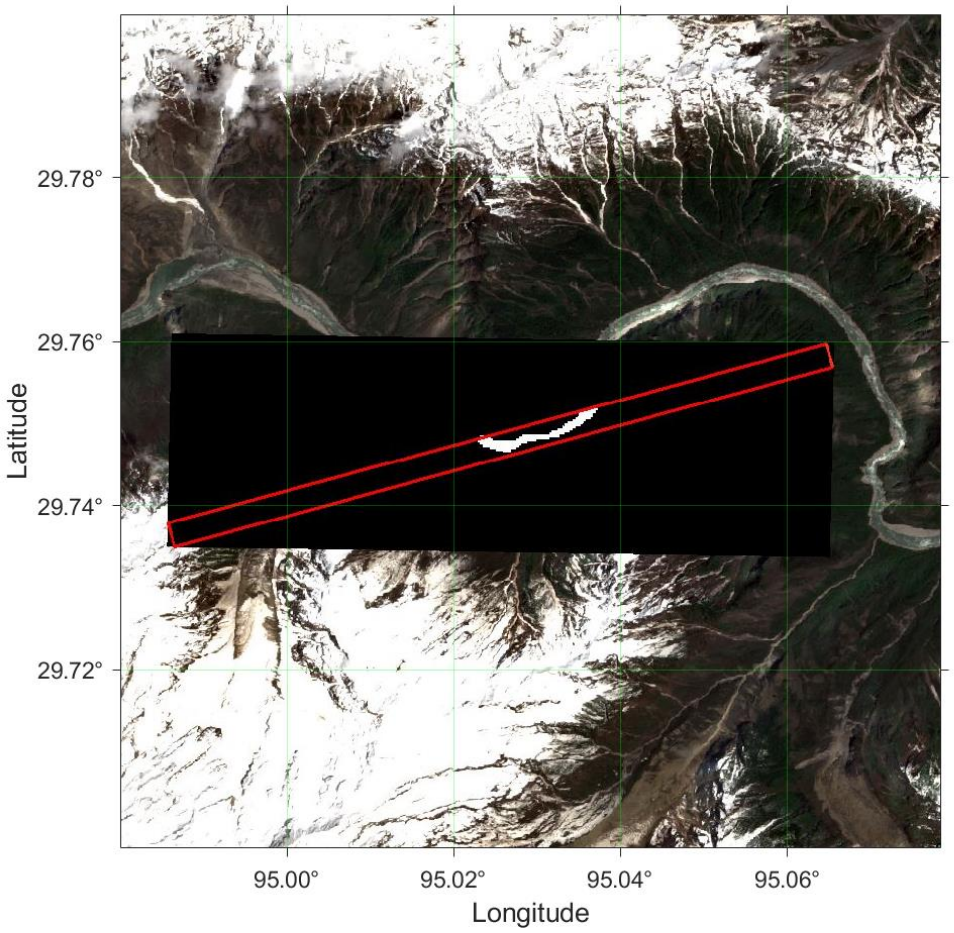

Figure 4.5: An example of water extraction by using MNDWI

The area of the river within the footprints can be calculated by:

$$S_{river} = N_{river} \cdot S_{pixel} \quad (4.2.6)$$

where N_{river} is the number of pixels which are classified as the river, and S_{pixel} is the area of one pixel. It is 400 m^2 for Sentinel-2 and 900 m^2 for Landsat-8.

To acquire the river length, we produce a line shapefile document for the target river base on the images. Take the footprints as the boundary, the river length of boundary is easy to compute (***Figure 4.6***).

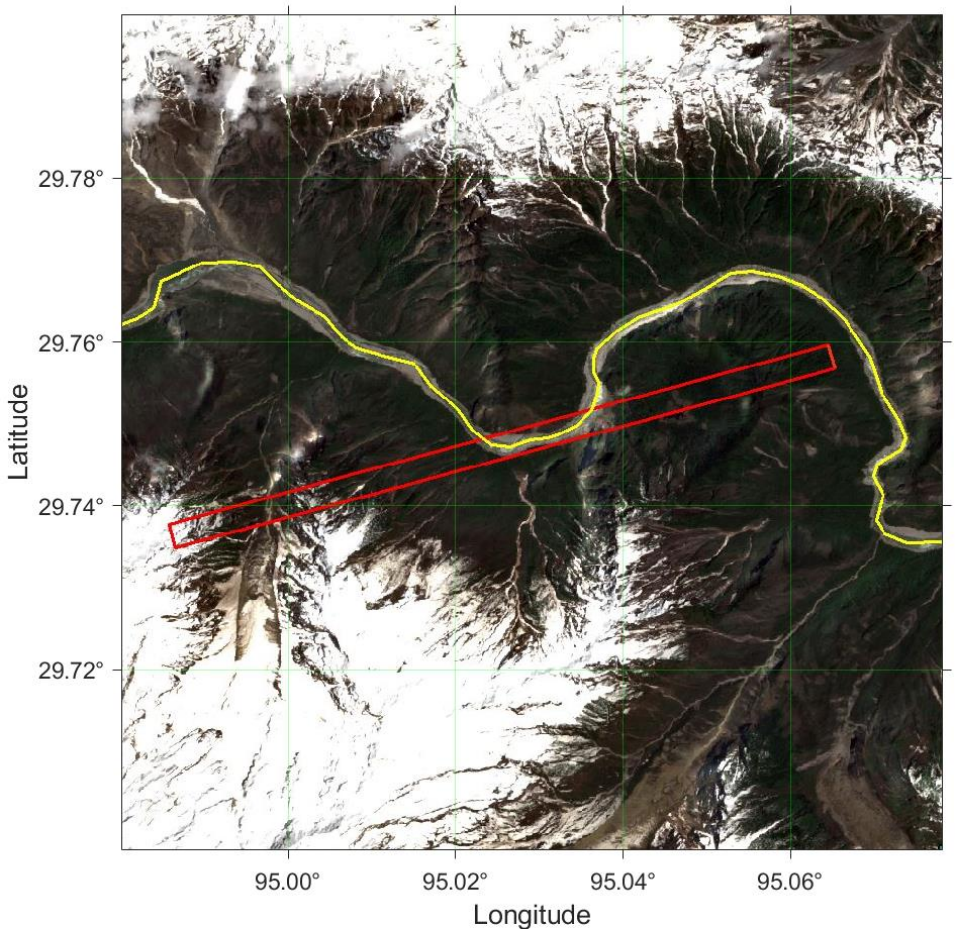

Figure 4.6: Line shapefile of the target river

The average width of the river can be evaluated by its area and length:

$$W_{river} = \frac{S_{river}}{L_{river}} \quad (4.2.7)$$

As for the last parameter, crossing angle, it can be computed by a combination of the satellite track and river shapefile. If the angle is larger than 90°, one more step of calculation is needed:

$$Uniform\ Crossing\ Angle = 180^\circ - Crossing\ Angle \quad (4.2.8)$$

However, there is still one crucial problem. As we introduced at the beginning of this section, we assumed footprints are the same for all virtual stations so that it is convenient for processing the images. Indicators generated from it might be larger than the true value because the length of assumed footprints is much longer than the actual situation. Hence, further adjustments on the size of footprints and corresponding indicators are needed. We acknowledge that the size of the footprint is influenced by topography and it has been evaluated in section 4.2.1. Referring to the elevation variance, we maintain the center position and reduce the length of footprints as following: 1) 6 km if its elevation variance is smaller than 500 m; 2) 4 km if its elevation variance is between 1500 m and 500 m; 3) 3 km if its elevation variance is between 1500 m and 3000 m; 4) 2 km if its elevation variance is larger than 3000 m. Afterward, we combine the new footprints with the line shapefile and the polygon shapefile of the river. The adjusted river area and length are obtained with the help of the ArcGIS tool. Eventually, we re-calculate the river width and re-count the number of individual water bodies.

4.2.3 Surface coverage

Most of the virtual stations are distributed in the mountainous area or suburban in our research, where the ground is mainly covered by vegetation. The situation of vegetation can be described by Normalized Difference Vegetation Index (Yue, et al., 2007):

$$NDVI = \frac{NIR - Red}{NIR + Red} \tag{4.2.9}$$

where the NIR is the near-infrared band (band 8 for MSI, band 5 for OLI) and Red is the red band (band 4 for MSI, band 4 for OLI).

We set the appropriate value as the threshold which normally is between 0.2 and 0.4. The region whose NDVI larger than the threshold is classified as vegetation area. An example of vegetation extraction based on adjusted footprints is presented in ***Figure 4.7***:

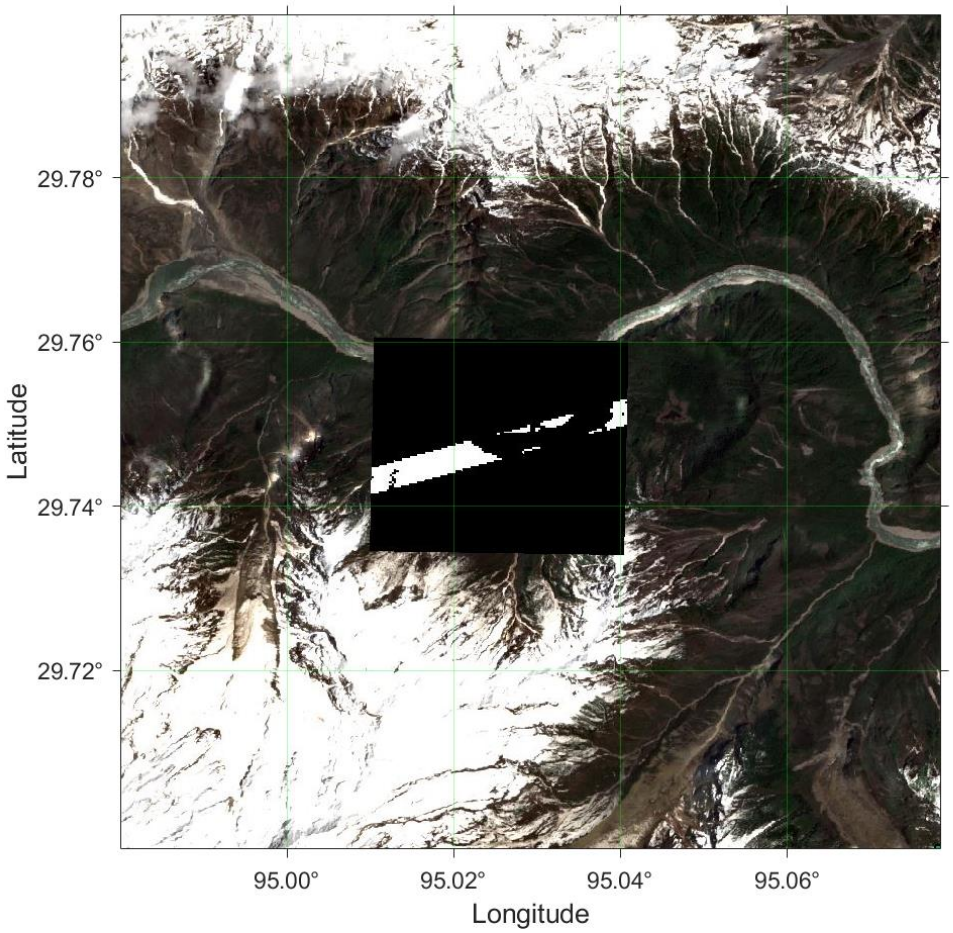

Figure 4.7: An example of vegetation extraction based on adjusted footprints

Chapter 5

Result and analysis

This chapter is set in two scenarios: analysis of two kinds of indicators, and analysis of the water level and all indicators. In the first part, we not only generally discuss how the environment influences the shape of waveforms but also determine some conditions and analyze whether the influence would change under the specific condition. In the second part, we present the time series of water level and indicators for each virtual station determined in previous chapters. We then comprehensively analyze which kind of environments, the waveform can be successfully retracked by aforementioned retracking methods.

5.1 Analysis of waveform and environmental indicators

5.1.1 General analysis

Combining the waveform and environmental indicators from 14 virtual stations that are surrounded by different environments, we have 196 groups of data in total. At the waveform side, we have 10 indicators including 1) thermal noise, 2) the number of peaks, 3) the position of the highest peak, 4) the power of the highest peak, 5) the position of the first peak, 6) the ratio of thermal noise and maximum power, 7) the width of the highest peak, 8) kurtosis, 9) peakiness, and 10) noise level. For the environment, we have 8 indicators defined:1) the area of the river, 2) the width of the river, 3) the number of water bodies, 4) the distance between the river and nadir point, 5) vegetation coverage, 6) elevation variance, 7) elevation difference, and 8) crossing angle. Plotting the scatter diagram for each pair of indicators, 80 scatter plots are presented in ***Figure 5.1***. For each plot, the x-axis denotes an indicator on the waveform side while the y-axis represents an indicator on the environment side. The shade of the color represents the density of points. We then calculate Spearman's rank correlation coefficient which adapts for the non-linear relation and is insensitive to prominent outliers. The result is shown in ***Figure 5.2***.

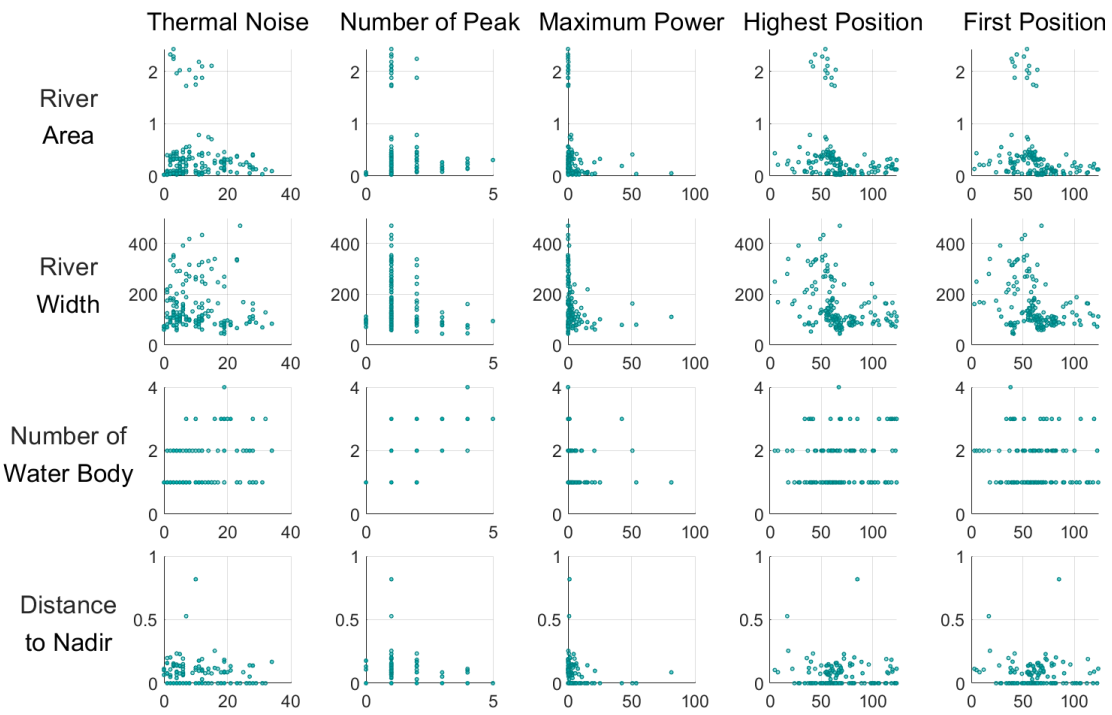
Thermal Noise
Number of Peak
Maximum Power
Highest Position
First Position
River Area
River Width
Number of Water Body
Distance to Nadir

(A)

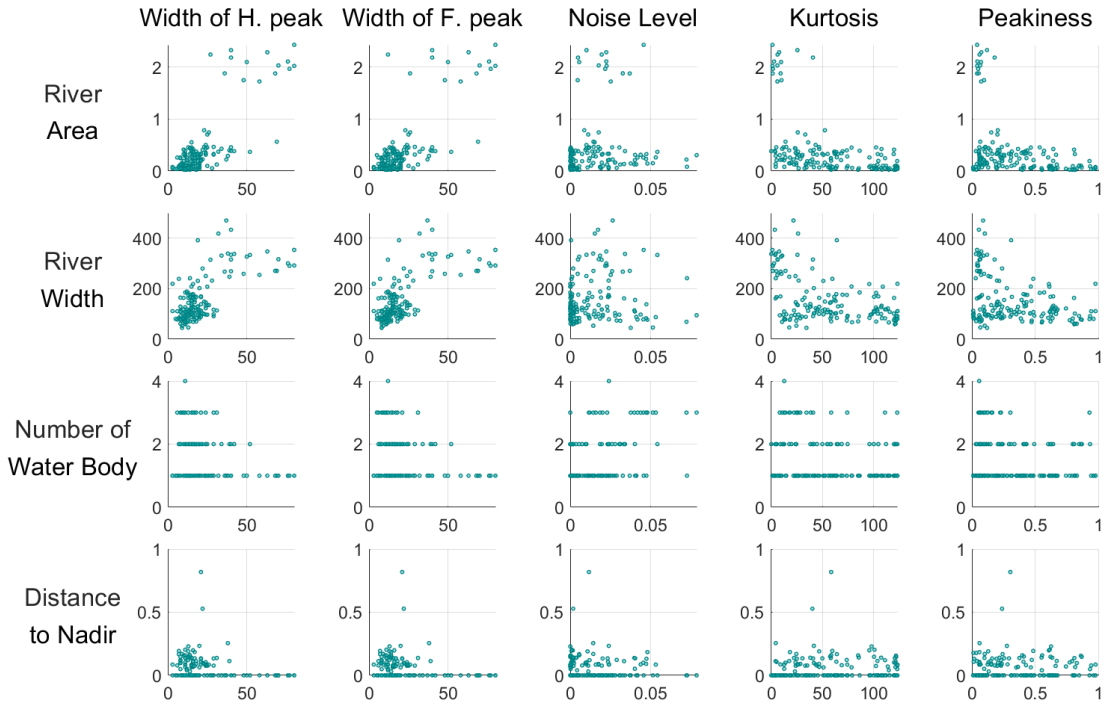
Width of H. peak
Width of F. peak
Noise Level
Kurtosis
Peakiness
River Area
River Width
Number of Water Body
Distance to Nadir

(B)

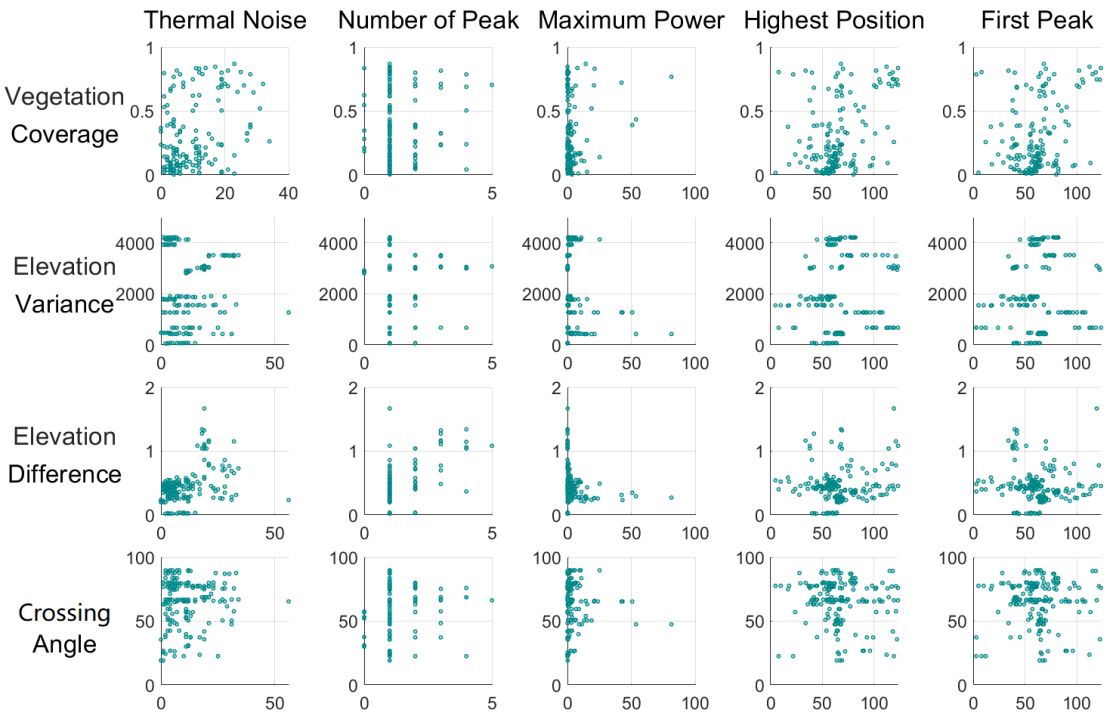

(C)

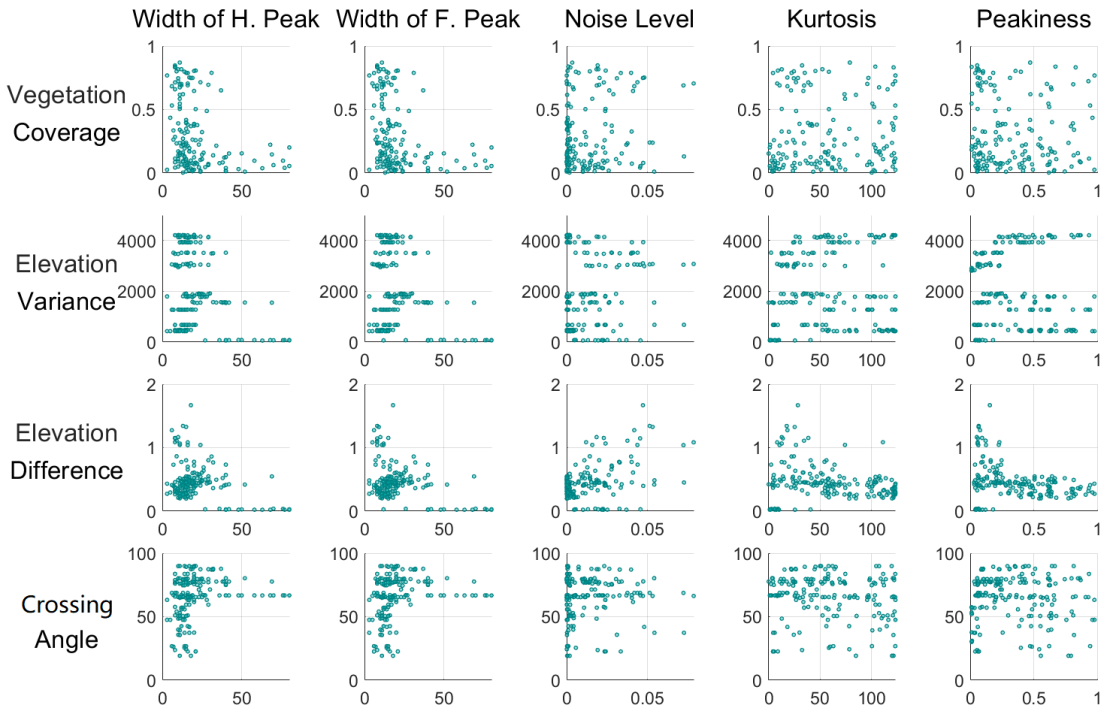

(D)

Figure 5.1: Scatter plots of the waveform and environmental indicators for the general result

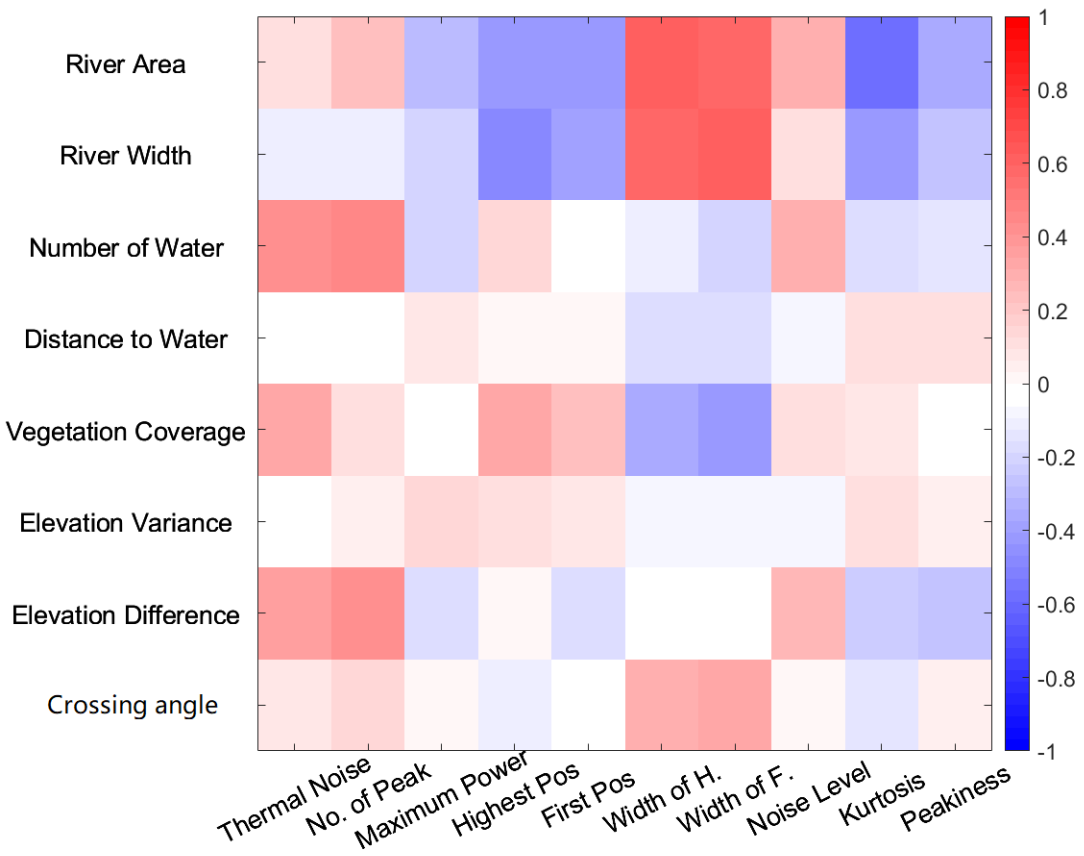

Figure 5.2: Spearman rank correlation of the waveform and environmental indicators for the general result

In general, several facts can be interpreted from the correlation figure:

- The area and width of the river have similar correlations with waveform indicators, showing positive correlations with the width of the waveform peak. As the waveform theory introduced in section 1.2.1, the Brown model waveform appears more often with the increasing in the size of the water body so that the width of the peak grows. Moreover, for a specular waveform, the larger area of the river illuminated by altimeter pulses, the longer time pulses contact with the river, meaning that the width of the peak increase as well.
- The area of the river also shows a negative correlation with kurtosis. It can be explained by the increase of the peak width. The increasing variance of a waveform is not only caused by its peak value but also a result of the wider waveform peak. Hence, the kurtosis would decrease with the increase of river area.
- The number of individual water bodies and the elevation difference expresses a positive correlation with thermal noise and the number of peaks. Except for the correlation between the number of water bodies and peaks. There is no theoretical interpretation for other correlations.

By further analysis of scatter plots, more details can be revealed:

- There are several prominent outliers in the area of the river (larger than 1 km^2), elevation variance, and elevation difference (approximate to 0). By tracing the sources of them, all of the outliers are measured from virtual station 15. It is located on a vast river surface which can be approximated to the ocean surface. Therefore, we exclude these outliers in post-analysis in order to eliminate the impact of these observations.
- We also find that although they have similar correlations, the distribution of scattered points for area and width is different. The scatter plots on width indicators show an even distribution without any outliers. One possible explanation can be that there is an inconsistency under different conditions. This deduction is verified in the next section.
- In principle, the distance between water bodies and nadir should influence the position of the first peak if the signal is properly tracked. However, the distance indicators show no relation with any waveform features in our case. The position of the first peak is randomly distributed on sample bins, although some distance indicators showing that the river is located on the nadir points of the altimeter. This phenomenon indicates that the capability of tracking system for inland water applications still needs improvement. In other words, the accuracy of OLTC DEM database can be further developed.
- By excluding the outliers, the distribution of elevation difference indicator shows a positive relation with noise level while elevation variance does not show any tendency. The observations on the distribution of maximum power illustrate that high powers appear more on the low elevation difference but there is no clear evidence showing the non-random distribution on elevation variance. These cases indicate that the waveform shape is more sensitive to the height difference along the track than the variance of the whole footprints.

The indicators demonstrated above include various conditions, that may preventing us from determining the influence of some specific indicators clearly. Therefore, the classification of the data is a viable method for investigating specific indicators. There are two main questions we want to answer. Firstly, for a complex waveform which often appears over inland water, the first peak may not be the highest peak of the waveform. As we discuss at the end of Chapter 3, different retracker may track the mid-power point of different peaks. Thus, the influences of environment on complex waveform is needed to be determined. Secondly, for a complicated environment, the environment influence may differ from the normal cases. Which environmental indicator plays a more important role is another question. These two subjects will be discussed after classification in the following section.

5.1.2 Analysis of the influence of complex waveform

A waveform which has more than one peak is classified as a complex waveform. There are 32 complex waveforms among all waveforms, the corresponding scatter plots and correlation diagram are shown in ***Figure 5.3*** and ***Figure 5.4*** respectively.

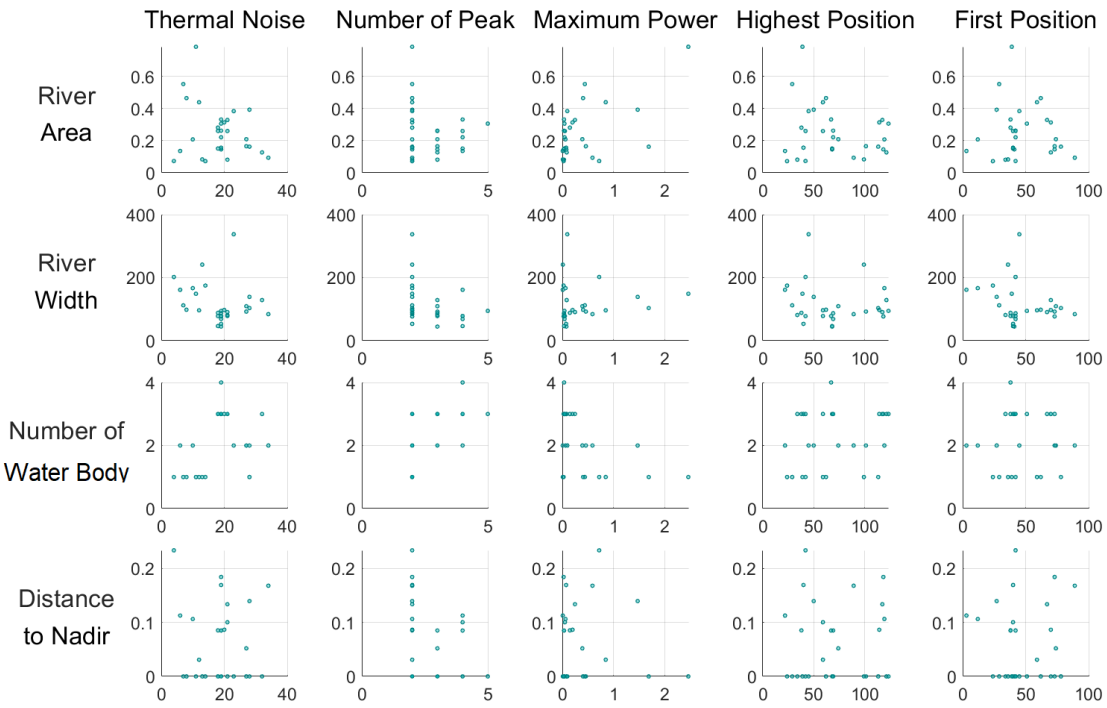
Thermal Noise
Number of Peak
Maximum Power
Highest Position
First Position
River Area
River Width
Number of Water Body
Distance to Nadir

(A)

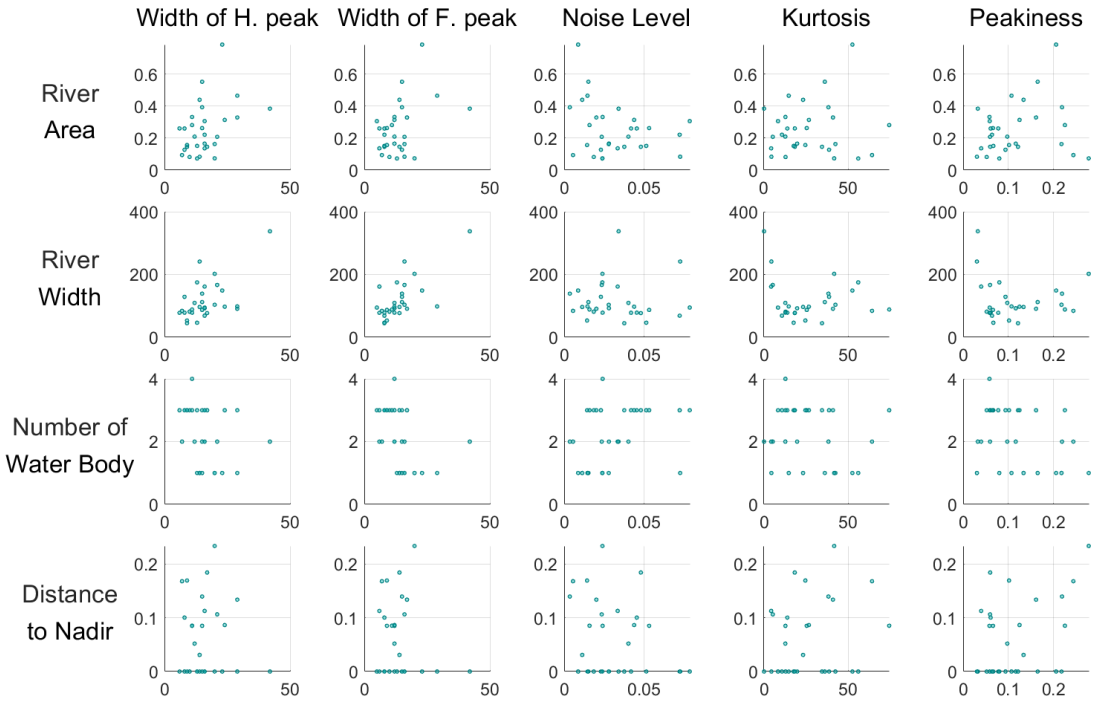
Width of H. peak
Width of F. peak
Noise Level
Kurtosis
Peakiness
River Area
River Width
Number of Water Body
Distance to Nadir

(B)

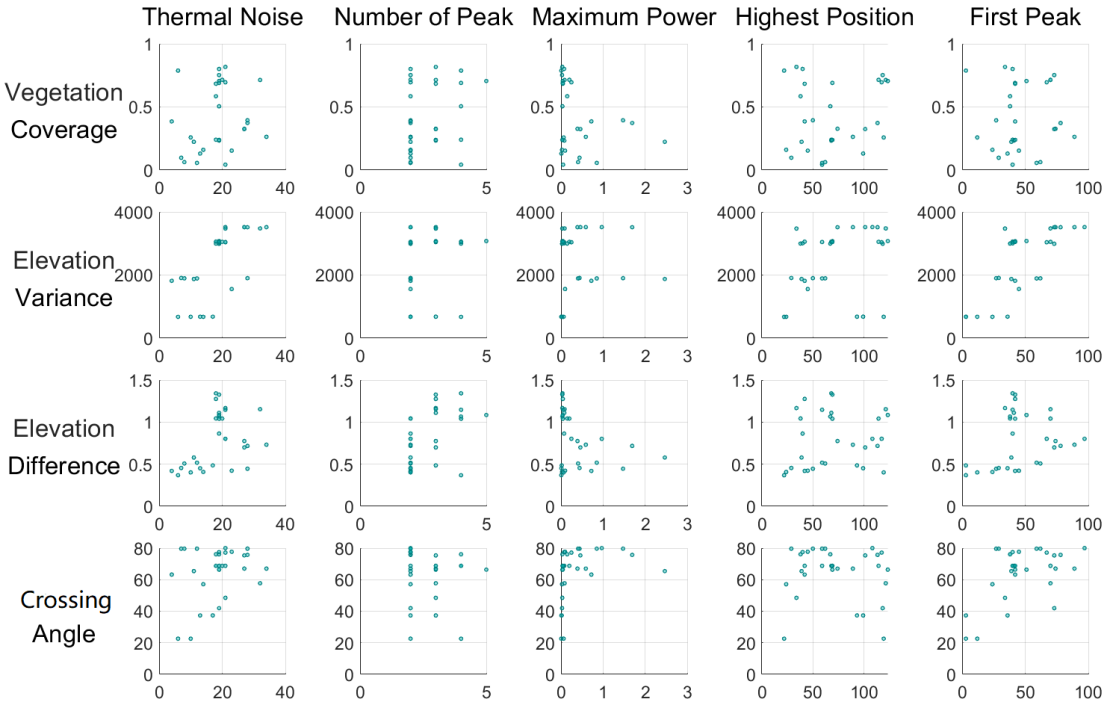

(C)

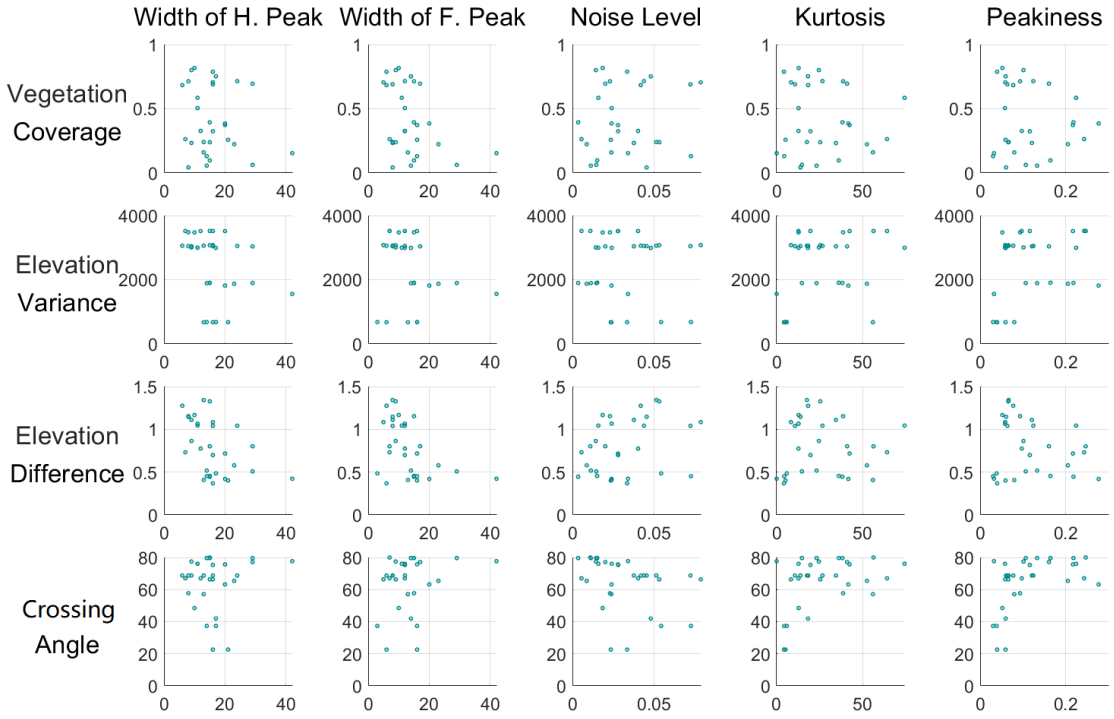

(D)

Figure 5.3: Scatter plots of the waveform and environmental indicators for the complex waveform

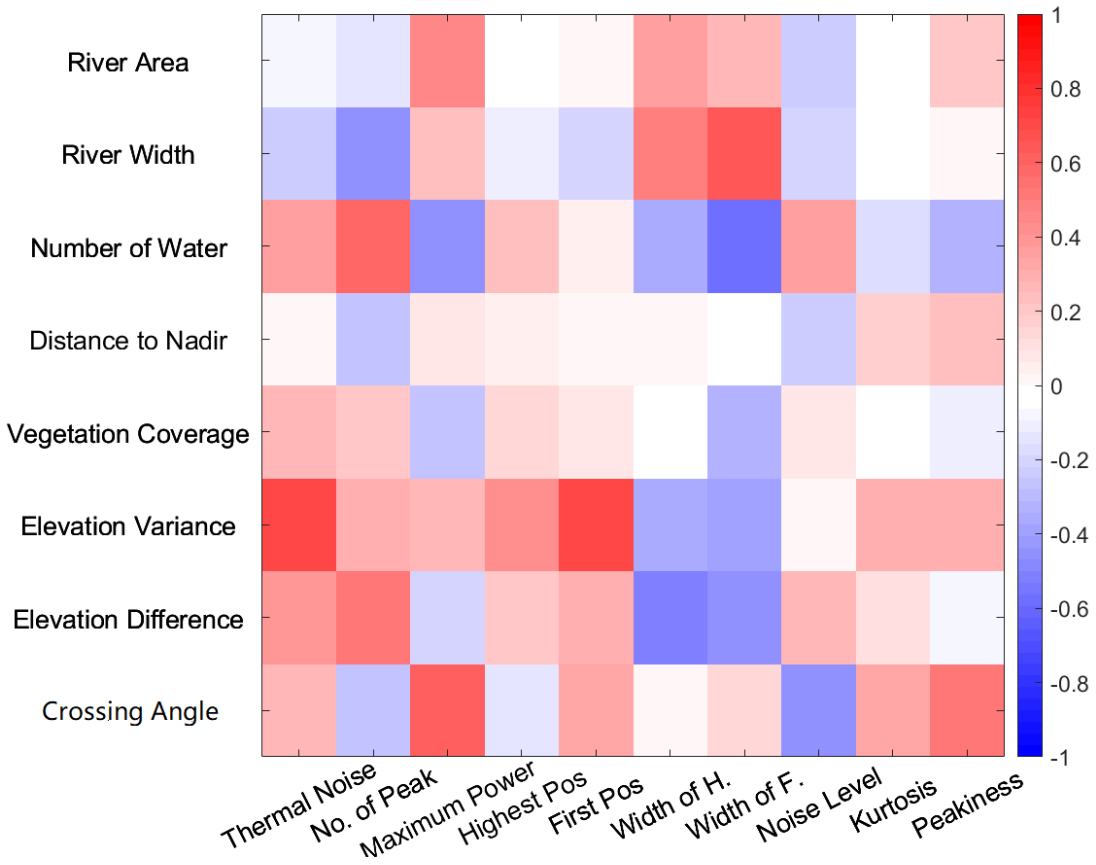

Figure 5.4: Spearman rank correlation of the waveform and environmental indicators for the complex waveform

From the figures above, we can find out that:

- The width indicator shows a more significant positive correlation with the width of the waveform peak than the area indicator.
- The number of individual water body shows that it has a negative relation with the width of the first peak.
- Both elevation variance and difference affect the width of the waveform peak. Meanwhile, the variance robustly influences the position of the first peak. More rapid the changes of elevation within footprints, later the appearance of the first peak.
- All elevation difference indicators are larger than 0.4, which means complex waveform usually appears in complicated topography.
- The larger maximum power usually corresponds to a low elevation difference and a high crossing angle.
- According to the distribution of peakiness indicator, the sharp waveform usually has a small crossing angle.

The comparison of these results and the general result (shown in figures 5.1 and 5.2) reveals that in the case of the complex waveform, the width of the river effectively influences the shape of the waveform, while the influence of the river decreases. Elevation variance plays an important role, but the elevation difference does not show any correlation with any waveform indicators.

5.1.3 Analysis of the influence of the complex environment

We allocate the data whose elevation difference indicator is larger than 0.45 (complex topography) and the number of the individual water body is more than 1 (complex water distribution) into the complex environment condition. Then the data whose elevation indicator smaller than 0.45 and water number equal to 1 is classified into normal condition. Results of normal environment condition are demonstrated in ***Figure 5.5*** and ***Figure 5.6***:

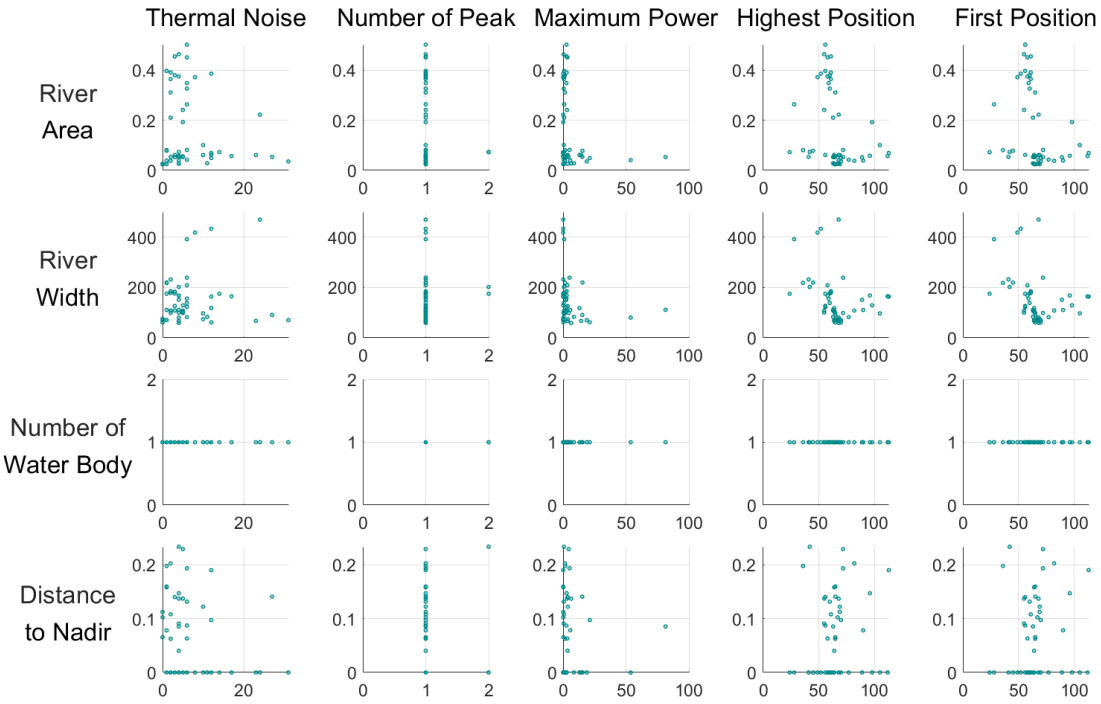

(A)

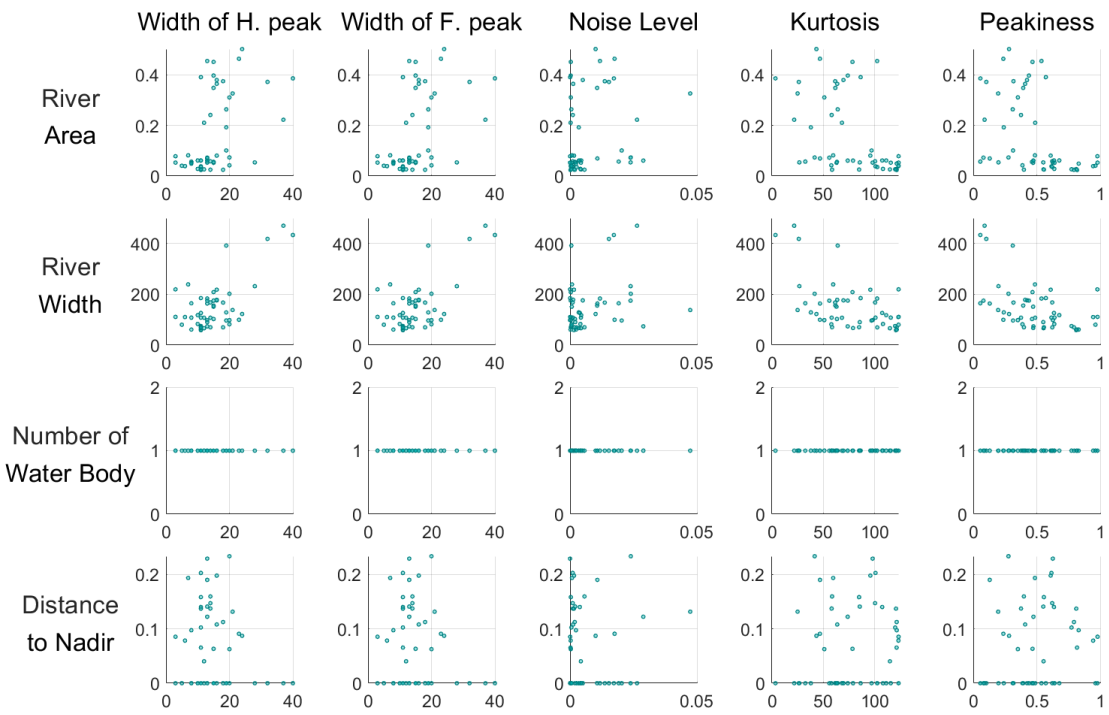
Width of H. peak
Width of F. peak
Noise Level
Kurtosis
Peakiness
River Area
River Width
Number of Water Body
Distance to Nadir

(B)

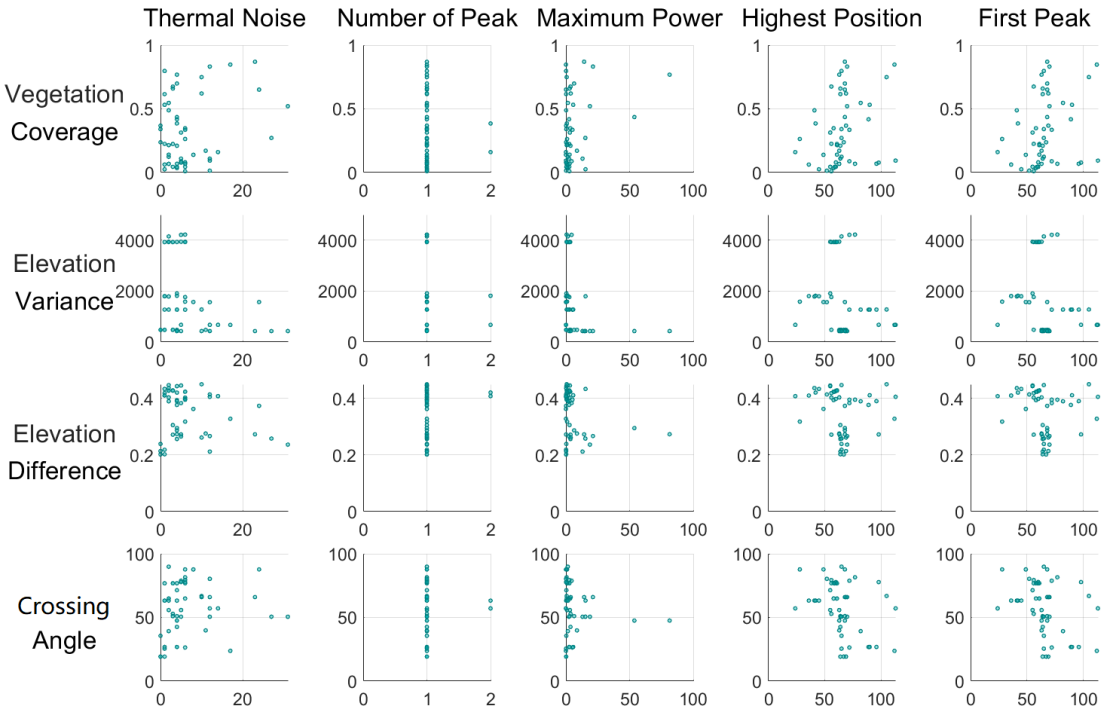
Thermal Noise
Number of Peak
Maximum Power
Highest Position
First Peak
Vegetation Coverage
Elevation Variance
Elevation Difference
Crossing Angle

(C)

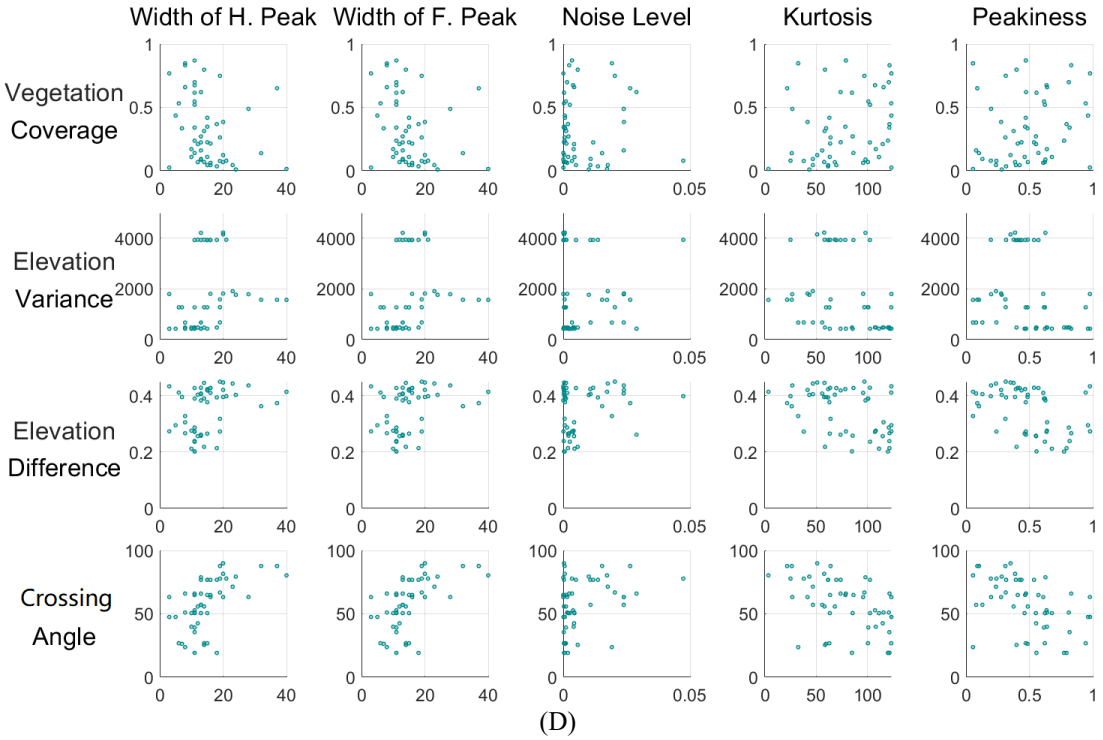

Figure 5.5: Scatter plots of the waveform and environmental indicators for the normal environment condition

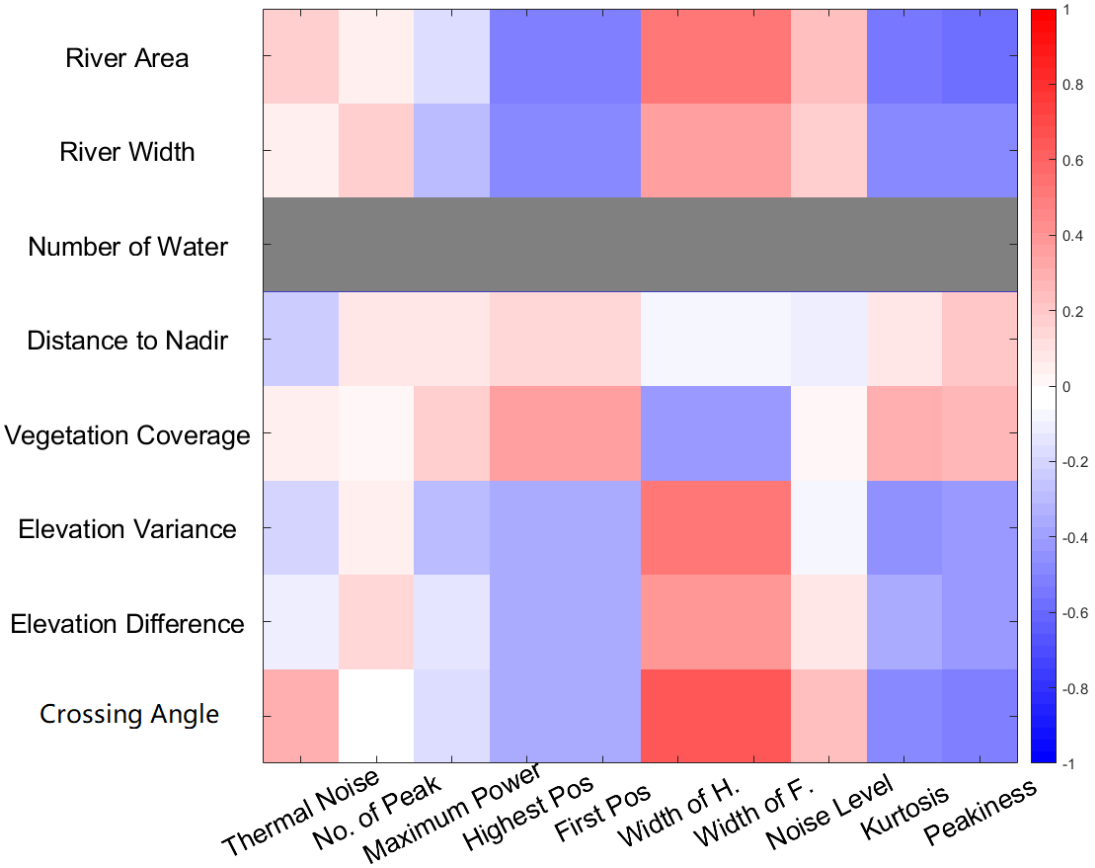

Figure 5.6: Spearman rank correlation of the waveform and environmental indicators for the normal environment condition

For the normal condition, a waveform is generated over a flat topography and only one water body is located within its corresponding footprints. Theoretically, the contamination of waveform can be reduced to a low level and less complex waveform appears under this condition. The figures above show following characteristics:

- The area and width of the river show a similar influence of waveform again. The area has a more significant impact.
- The highest peak coincides exactly with the first peak, and the number of peaks is essentially equal to one except in very rare cases. That means little complex waveform appears in this condition.
- The noise level is significantly reduced. Most of the noise level is less than 0.03.
- Elevation variance and difference perform less influence with the shape of the waveform and are replaced by crossing angle.
- All the difference indicators are less than 0.45. However, some of the variance indicators remain at a high level (about 4000). By comparing the fact of these two indicators, we conclude that variance indicator is not necessarily a reliable factor in evaluating topography. In other words, the along-track elevation difference may not be significant in high variation areas. Using the elevation difference to evaluate topography influence is better than elevation variance.

Results of complex environment condition are shown in:

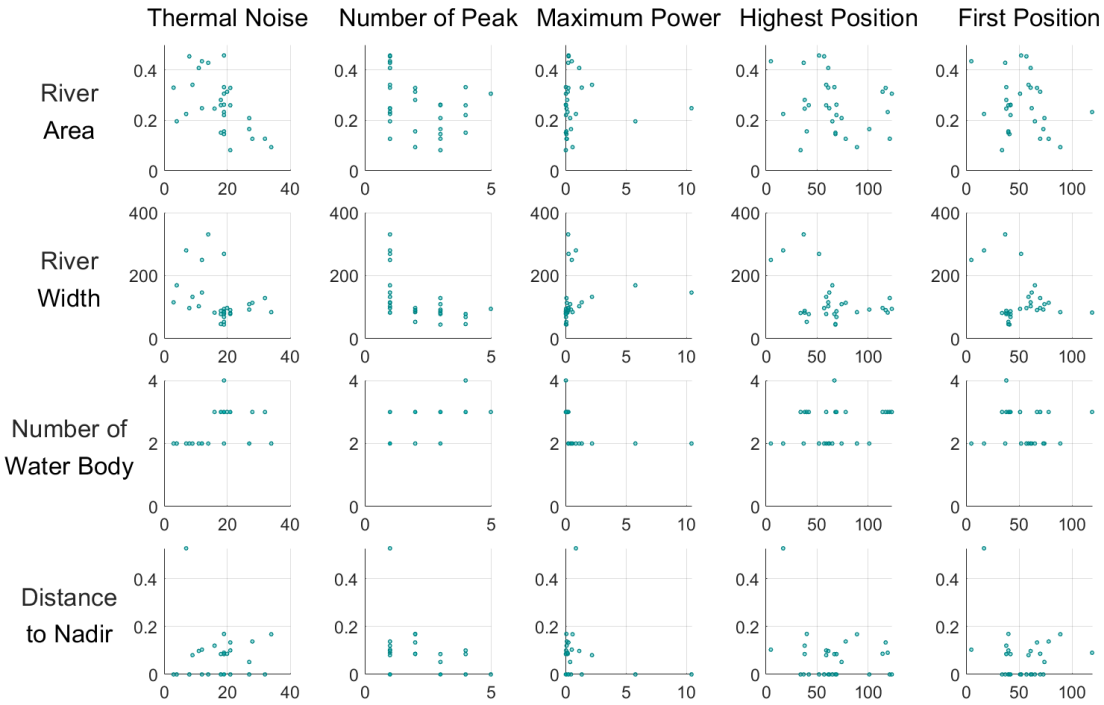

(A)

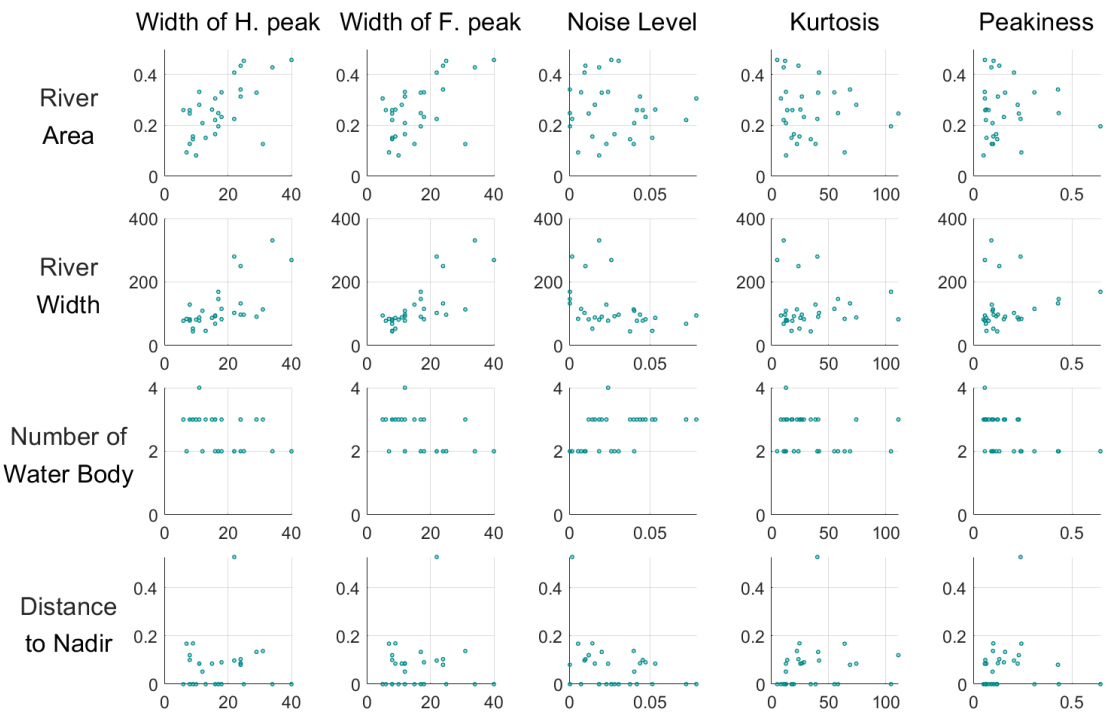
Width of H. peak
Width of F. peak
Noise Level
Kurtosis
Peakiness
River Area
River Width
Number of Water Body
Distance to Nadir

(B)

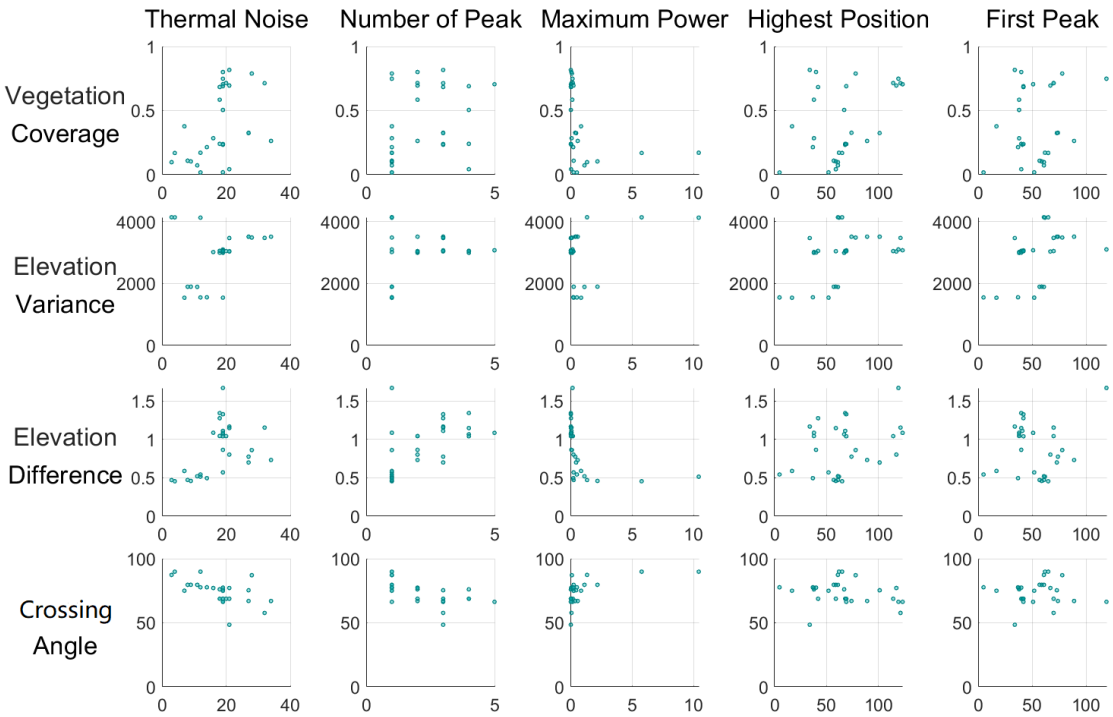
Thermal Noise
Number of Peak
Maximum Power
Highest Position
First Peak
Vegetation Coverage
Elevation Variance
Elevation Difference
Crossing Angle

(C)

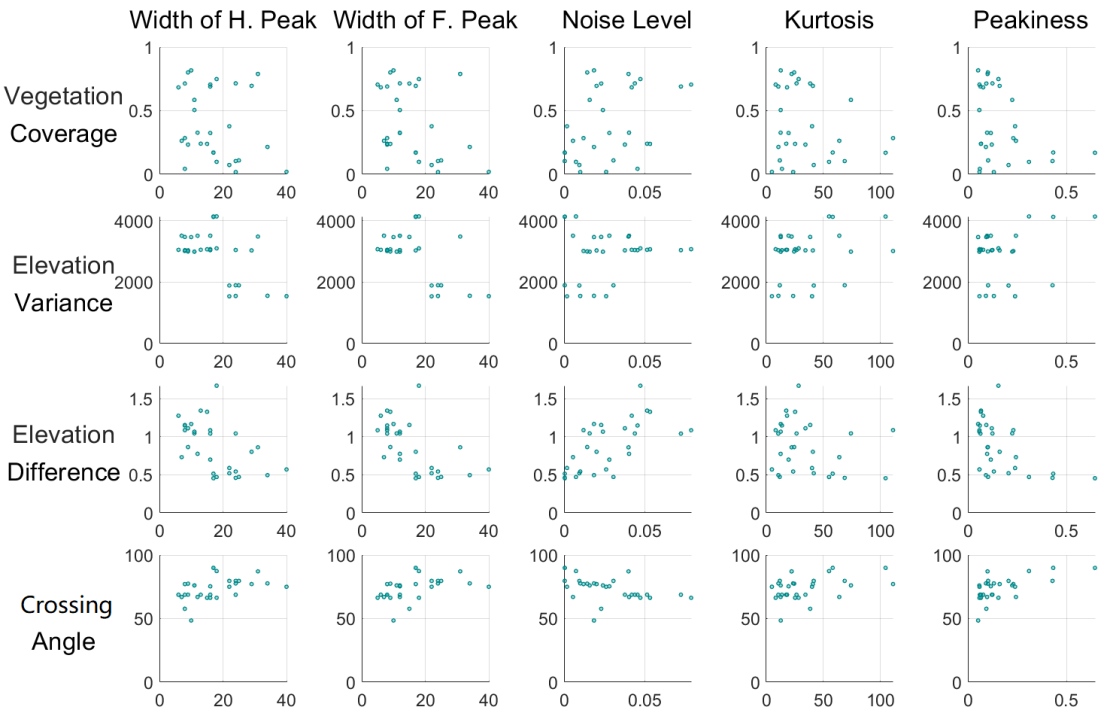

(D)

Figure 5.7: Scatter plots of the waveform and environmental indicators for the complex environment condition

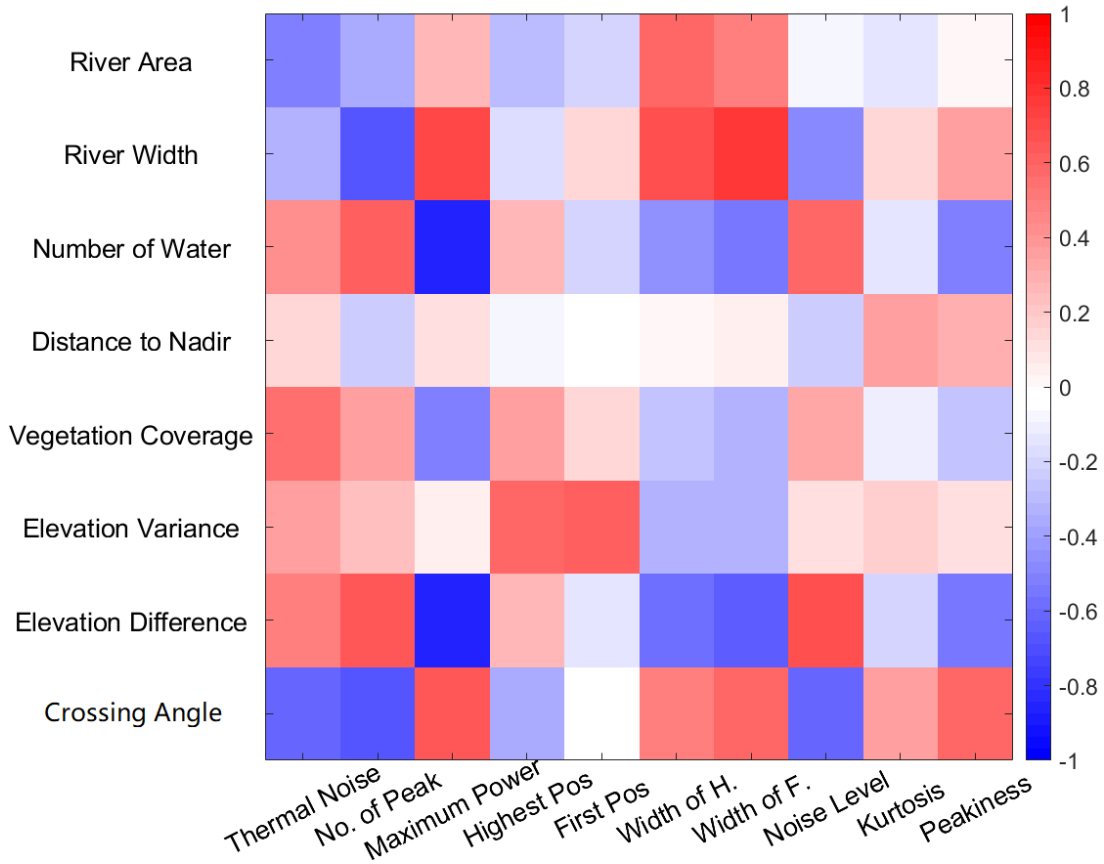

Figure 5.8: Spearman rank correlation of the waveform and environmental indicators for the complex environment condition

The figures above show different results from the normal condition:

- The width of the river shows a more robust influence of waveform. With the increase of river width, not only the peak gets wider but also the maximum power becomes larger.
- Crossing angle plays an important role in determining the shape of the waveform. With the crossing angle approaching 90°, the width of peak increases but the waveform becomes sharper. It is because the number of the peak also decreases which can amplify the influence of the highest peak and increase the peakiness and kurtosis.
- More noise level indicators are larger than 0.03 and the high noise level is associated with the elevation difference and the number of water bodies.
- Complex waveforms appear in the complex environment and the corresponding river widths are narrower than 140 m.

The area of river influences more on the waveform shape in a flat area, whereas the width of river has larger impacts on the waveform shape in complex environment. Crossing angle is only associated with peak width in the normal condition. However, it also affects the number of peaks in the complex condition. The high noise level and the complex waveform appear considerably more frequent in complex environment, which means it is more difficult to be properly retracked. In addition, some positions of the first peak which are larger than 100 bins occur in both conditions, revealing that the error tracking may not be solely influenced by the elevation factor.

5.2 Analysis of indicators and water surface height

After understanding the relationship between environment and waveform, we further combine them with the water level to analysis the impacts of the environment on the performance of different retrackers. The combined results of each virtual station are demonstrated as shown in ***Figure 5.9***—***Figure 5.22***.

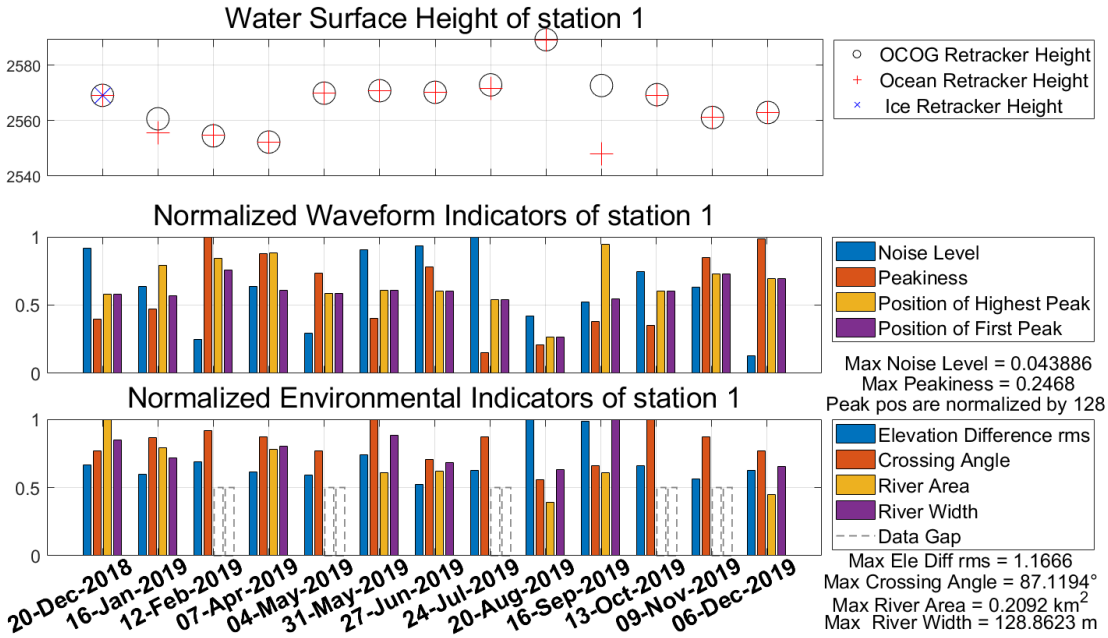

Figure 5.9: Combined results of Indicators and water surface height in station 1

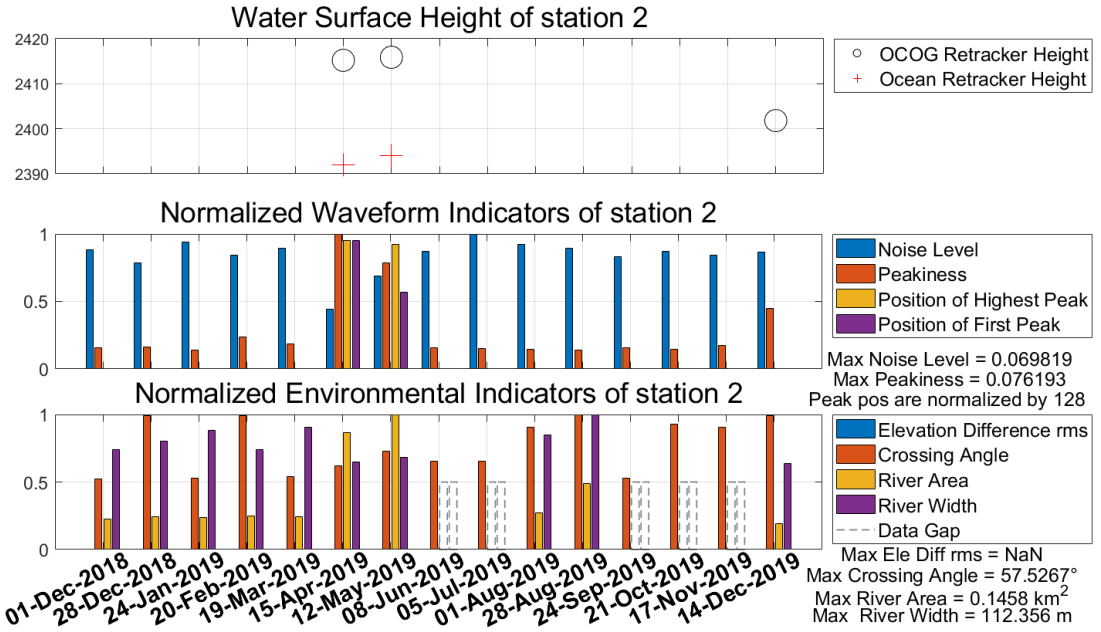

Figure 5.10: Combined results of Indicators and water surface height in station 2

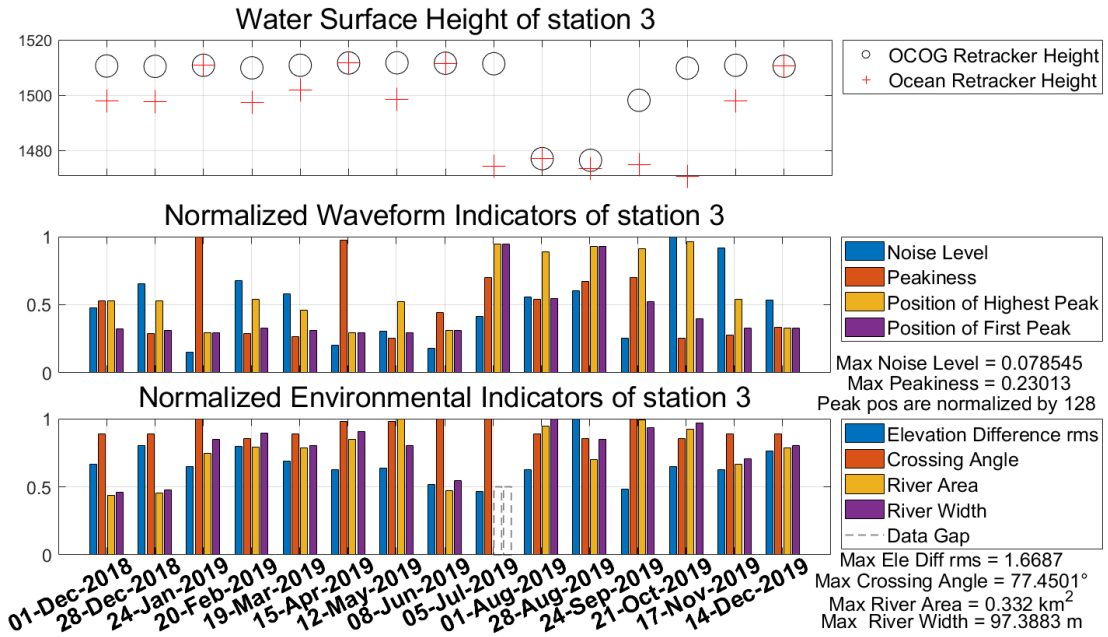

Figure 5.11: Combined results of Indicators and water surface height in station 3

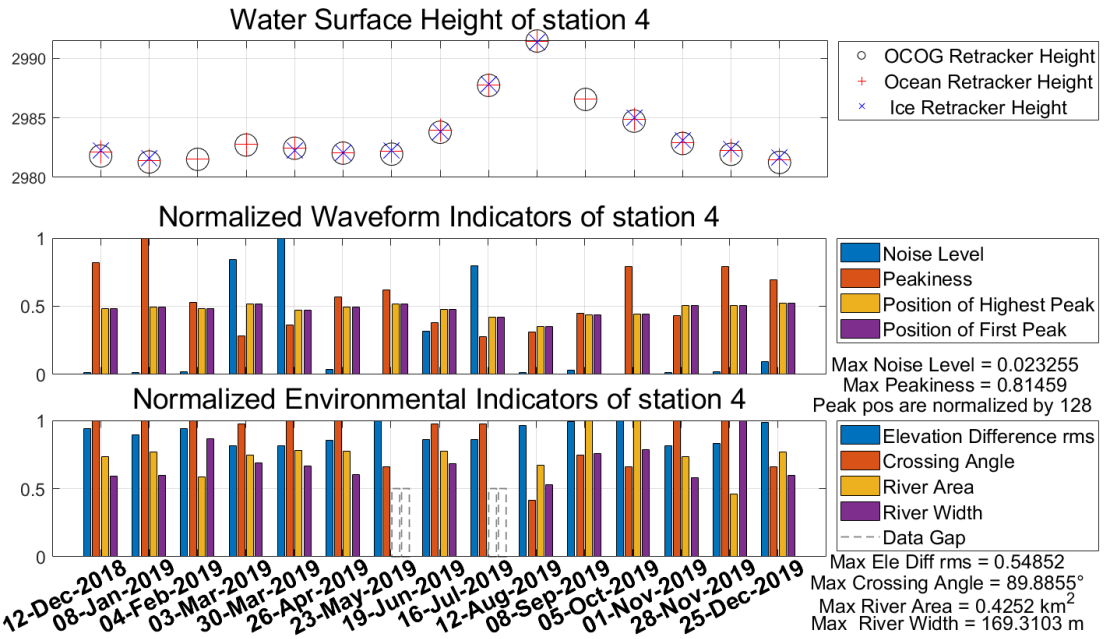

Figure 5.12: Combined results of Indicators and water surface height in station 4

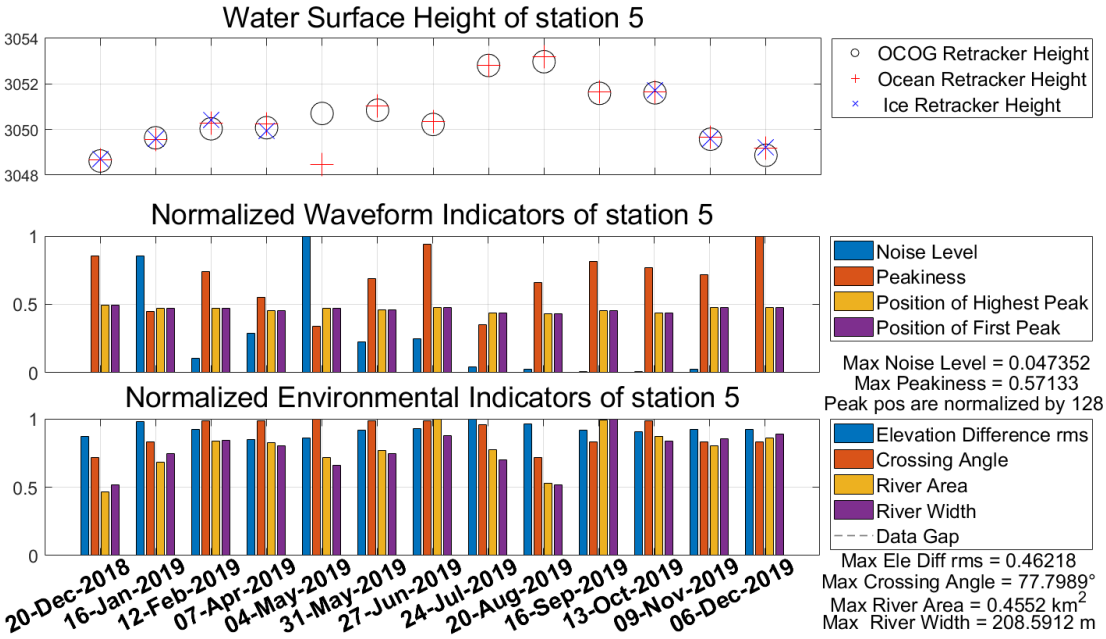

Figure 5.13: Combined results of Indicators and water surface height in station 5

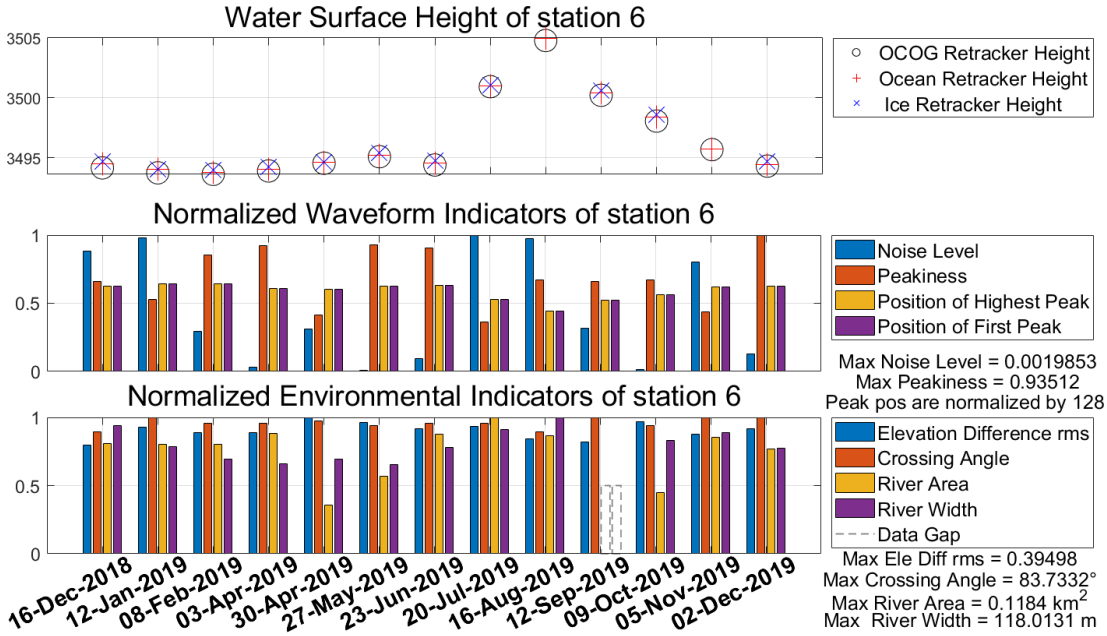

Figure 5.14: Combined results of Indicators and water surface height in station 6

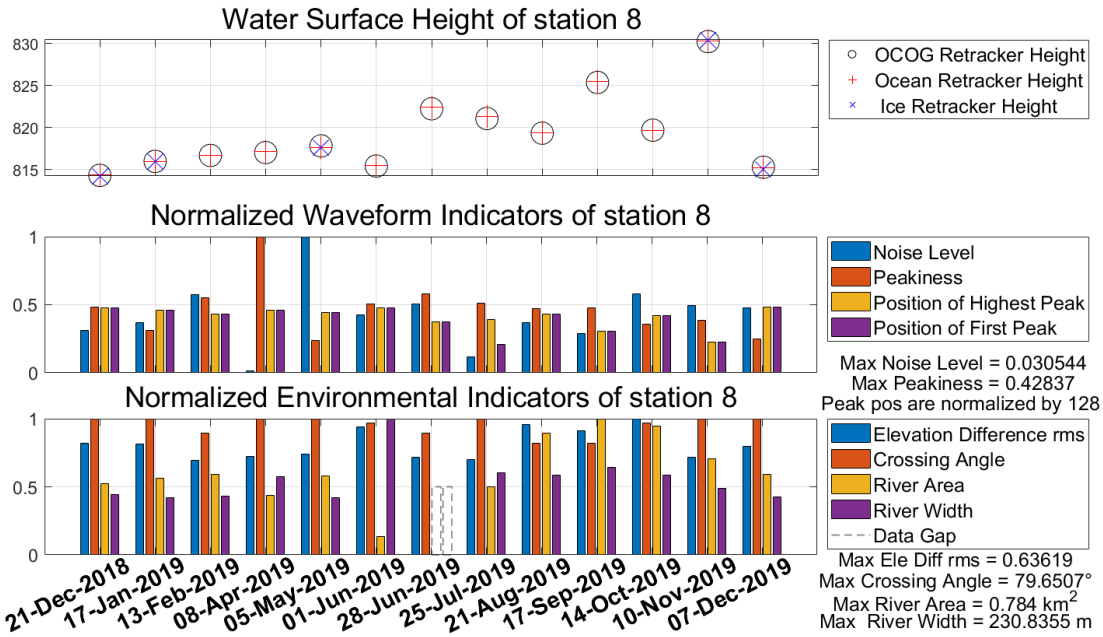

Figure 5.15: Combined results of Indicators and water surface height in station 8

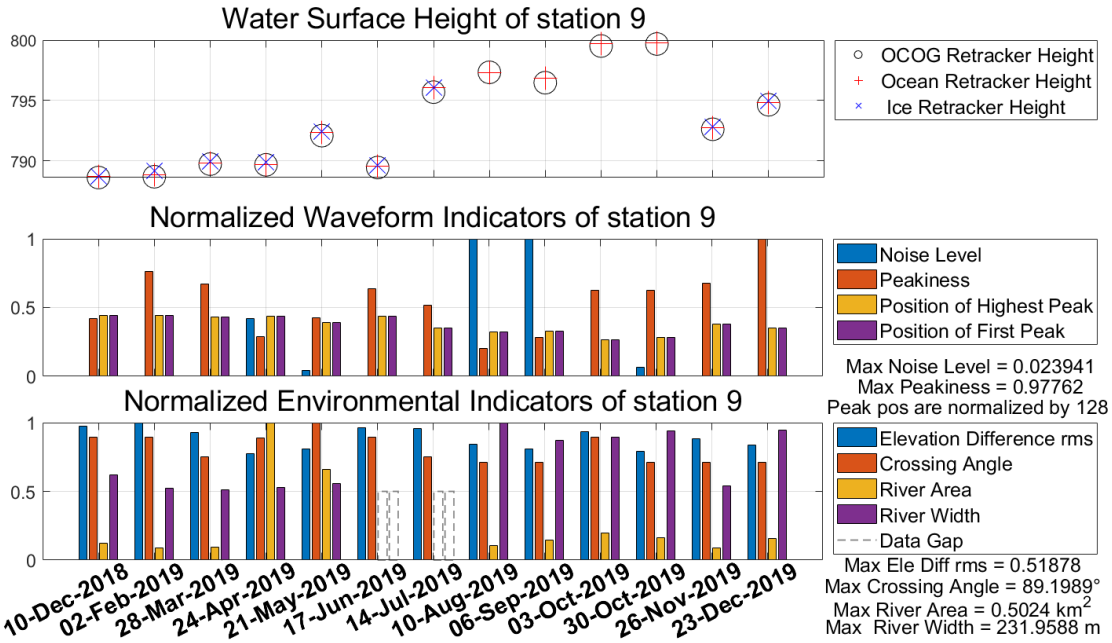

Figure 5.16: Combined results of Indicators and water surface height in station 9

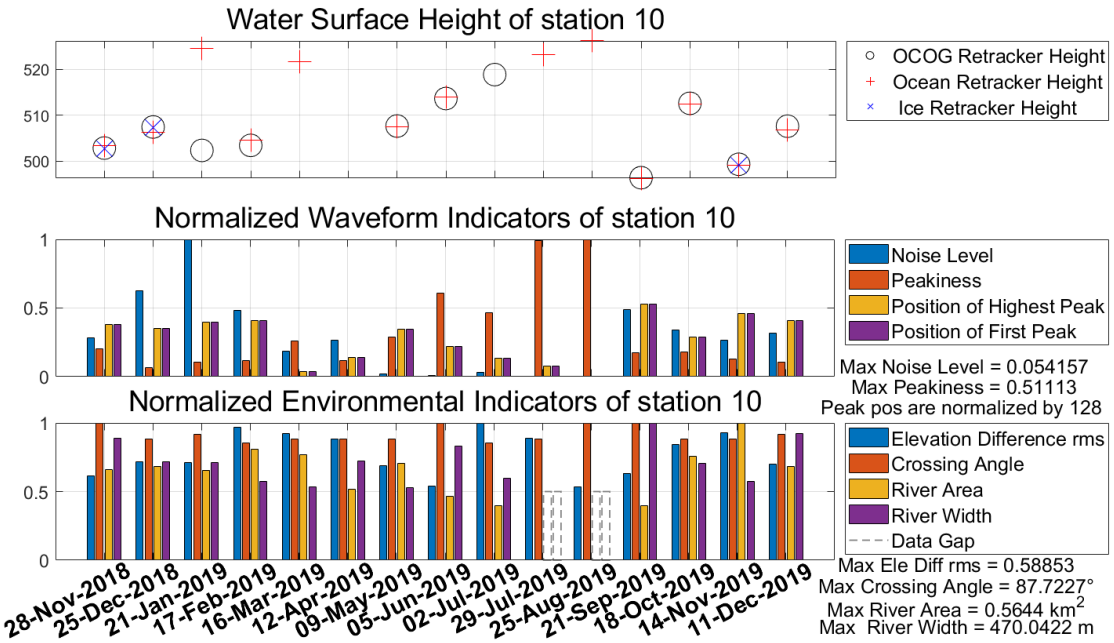

Figure 5.17: Combined results of Indicators and water surface height in station 10

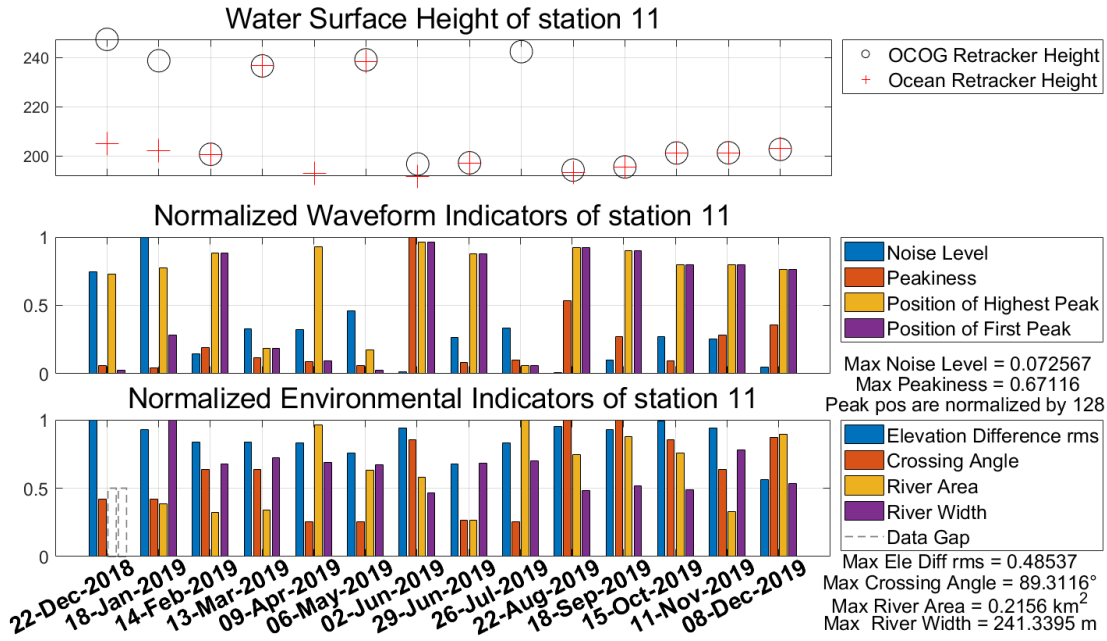

Figure 5.18: Combined results of Indicators and water surface height in station 11

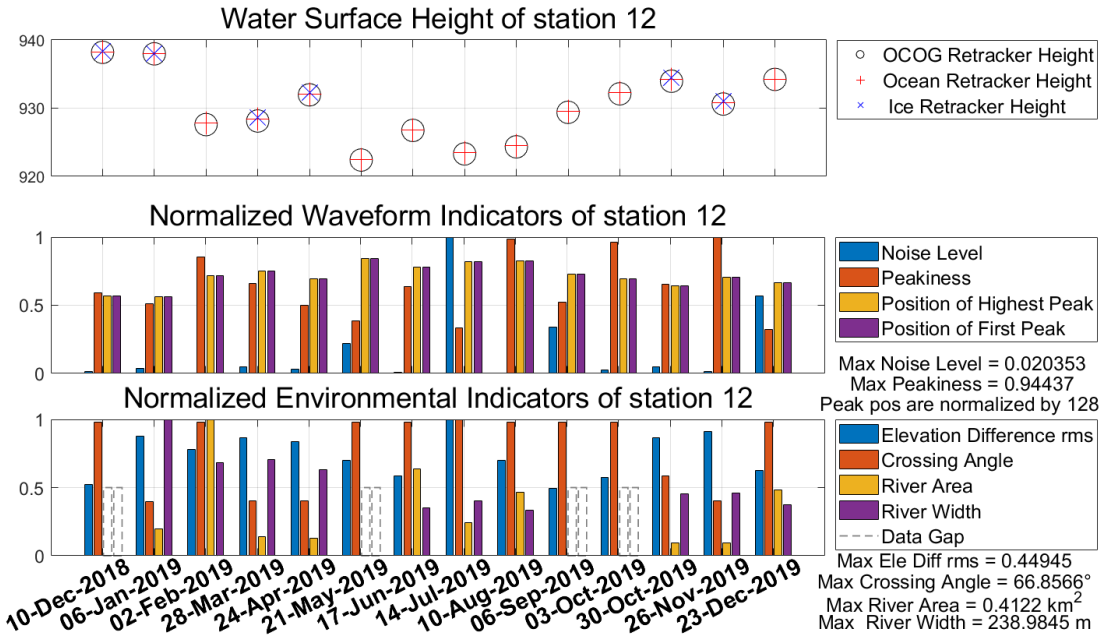

Figure 5.19: Combined results of Indicators and water surface height in station 12

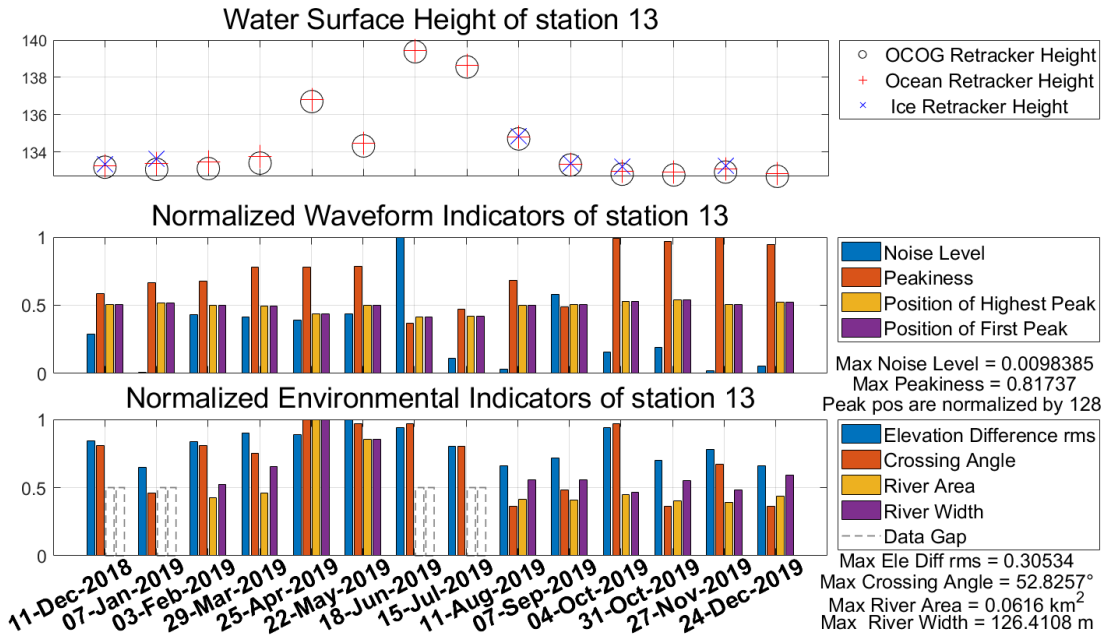

Figure 5.20: Combined results of Indicators and water surface height in station 13

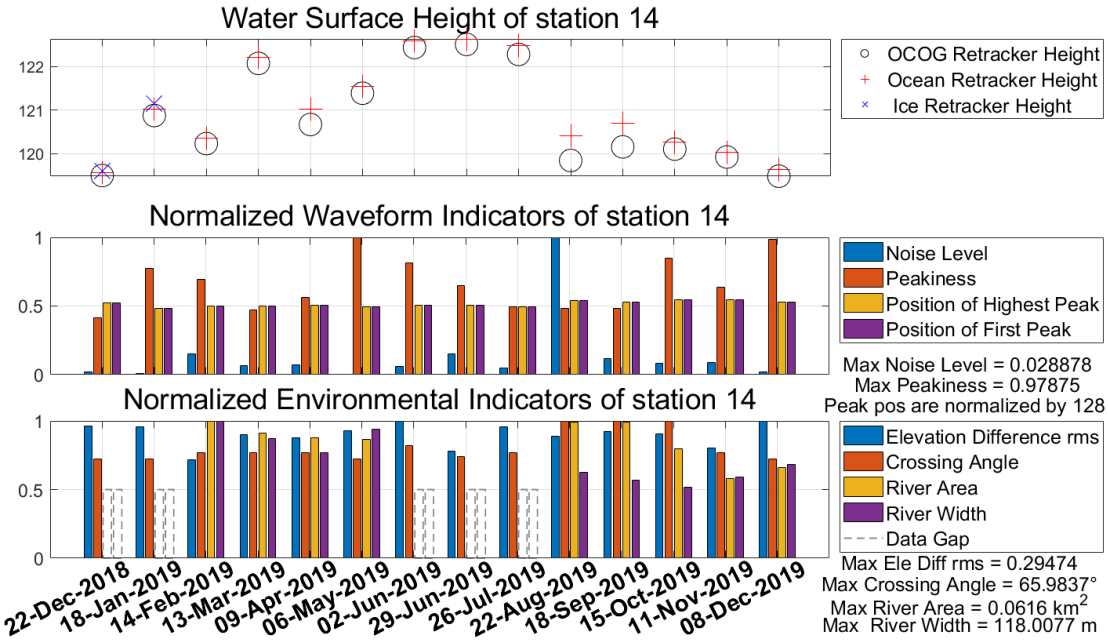

Figure 5.21: Combined results of Indicators and water surface height in station 14

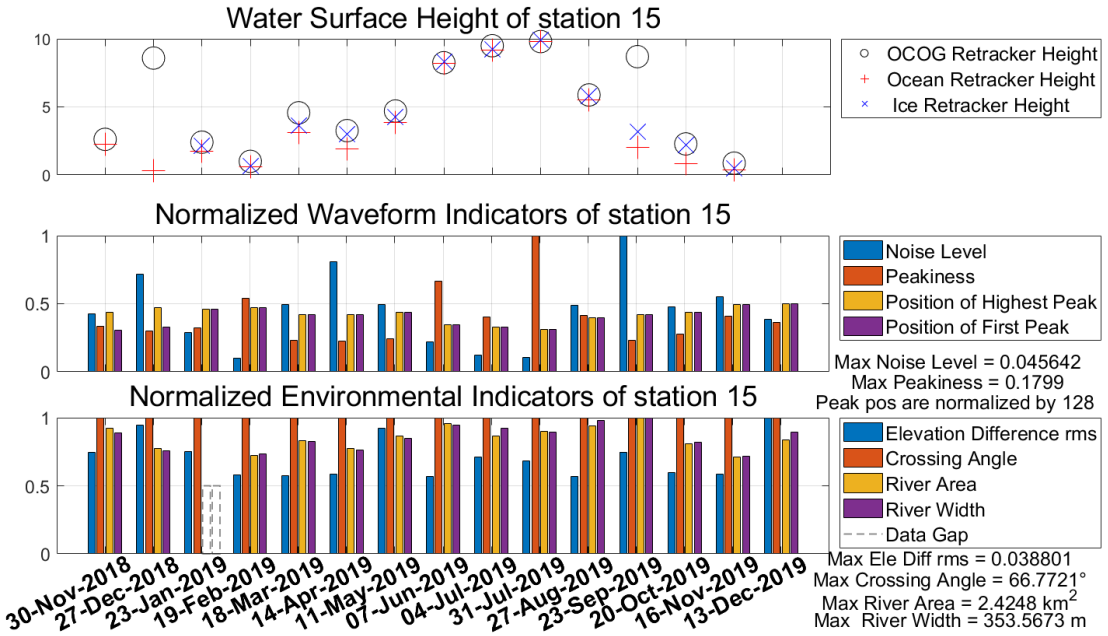

Figure 5.22: Combined results of Indicators and water surface height in station 15

Follow the classification example in Chapter 3, we first divide all results into four groups: successful retracking by three methods, two methods (OCOG and Ocean), sole

method, and failure retracking. The summarized results about waveform and environmental indicators are shown in the distribution table below (***Table 5.1***).

Table 5.1: Summary of indicator distribution for three groups

Statistical Type	Retracking by all methods	Retracking by two methods	Retracking by sole methods	Failure retracking
Total number	74	101	7	14
High noise level	6	22	2	14
Low noise level	68	79	5	0
High elevation diff	24	46	3	1
Low elevation diff	50	53	3	1
Proper tracking	74	100	1	1
Anomaly tracking	0	1	6	13

The total number in the table is the amount of four groups. High noise level and low noise level correspond to noise level indicator respectively, larger or smaller than 0.03. High elevation diff means elevation difference higher than 0.45, whereas low elevation diff represents elevation difference lower than that. The condition of proper tracking represents the position of the first peak later than 10 bins while anomaly tracking's condition is prior to 10 bins (***Figure 5.23***).

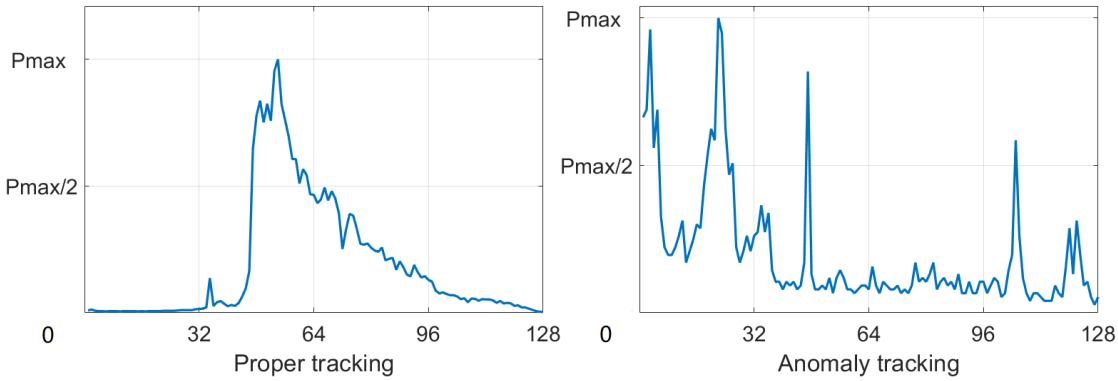

Figure 5.23: The condition of proper tracking and anomaly tracking

Anomaly tracking also includes the condition with no peak appearing in the waveform. Nevertheless, the sum of the two elevation types is smaller than the total number. This is because the DEM documents for the virtual station 2 are lost.

From the distribution table and combined results, we can observe that:

- For group one, most waveforms have a low noise level and a low elevation difference and all of them have been set a proper reception window.
- For group two, the majority of the waveforms has a low noise level. The elevation difference does not affect the success of retracking by OCOG and Ocean retracker. Only one anomaly tracking occurs in station 11 cycle 6. Its corresponding waveform has two peaks. Both of the retrackers ignore the first peak but retrack the highest peak.
- For group three, anomaly tracking is the critical factor affecting the retracking results. Most of the first peaks that are prior to 15 bins have the fact of the peak being ignored by some kinds of retracker. Although the remaining one (station 2 cycle 15) has been properly tracked, its high noise level also leads to failure retracking.
- For the last group, the waveform does not contain any water information but pure noise, which means altimeter set a definitely wrong reception window. However, the failure reason for station 15 cycle 15 is still unknown. Its waveform is a typical brown waveform which should be easily retracked by all methods. One potential explanation is that there might be some errors happened in the post-processing step.

Although some waveforms can be retracked by multiple retrackers, the height results are different across the three types retracking. According to the magnitude of height difference and indicator results, we generated a new distribution table:

Table 5.2: Summary of indicator distribution refer to the height difference

Statistical Type	**Retracking by all methods**			**Retracking by two methods**		
Height difference	< 1 m	1-5 m	> 5m	< 1 m	1-5 m	> 5m
High noise level	3	2	1	6	3	13
Low noise level	66	2	0	73	2	4
Identical peak pos	69	4	1	73	5	3
Different peak pos	0	0	0	6	0	14
Wide river	40	4	1	43	3	3
Narrow river	18	0	0	23	1	13
High elevation diff	24	0	0	29	4	15
Low elevation diff	45	4	1	50	1	2

In addition to the types of statistics introduced in the last table, identical peak position

means the position of the first peak coincides with the position of the highest peak, and different peak position represents the two aforementioned positions fail to coincide with each other. The condition of the wide river is 100 m. Otherwise, it will be considered as a narrow river.

According to the statistic of the peak's position, most of the different positions can lead to a height difference which is larger than 5 m. This is because OCOG method usually sets the retracking gate on the highest peak, but Ocean method sets it on the first peak. This can lead to a height difference of more than ten meters. Thus, although peaks' positions are different for 6 samples with a tiny height difference, we believe that OCOG and Ocean also set the retracking gate on the same peak. Here, the first conclusion can be given:

- Different retrackers applying offset on different leading-edges results in a large height difference.

Then we focus on the only sample in the fourth column of ***Table 5.2***. Its waveform is obtained from a wide river and has only one peak. The along-track elevation difference is also low but the noise level is high. Therefore, we consider:

- The high noise level contributes to the large height difference between the retrackers.

We further concentrate on the distribution of the ninth row in the table, fifteen samples in this type have large height differences, which are even more than different pos (14) and high noise level (13). Combining with conclusion mentioned in section 5.1, that elevation difference has a positive correlation with the noise level, we believe that:

- The high elevation difference is related to the high noise level. At the same time, it can generate a large height difference between retrackers.

The sample's distribution of the narrow river is similar to the high elevation difference. Most of the large height difference corresponds to a narrow river. We then interpret that:

- The width of the river affects the large height difference between retrackers.

So far, we established the connection between indicators and the water surface height. Furthermore, we determined out the relationship between them.

Chapter 6

Summary, conclusion and outlook

6.1 Summary and conclusion

The whole thesis begins with a question of how the ground environment influences the altimetry measurements over inland water. To investigate this question, several preparations are performed. For the altimetry data, we selected the Sentinel-3B data because it applies a new tracking technique OLTC, which has a better performance on the inland application. The ground environment cannot be directly obtained from any in situ instrument. Thus, we divided the environment feature into two parts: one part is the topography, which can be determined by STRM DEM data; another part is the river features and the surface type, which can be extracted from satellite optical images from Sentinel-2 and Landsat-8. Since this study focuses on the influence of the environment on altimetry, we selected rivers located in various environments. To this end, we selected 14 virtual stations located in the Yangtze River, which flows in a flat area, and the Yarlung Tsangpo River, which is surrounded by a variable topography.

After the preparation, we generate the water level of all virtual stations based on three types of range measurements recorded in the Sentinel-3 products. These three ranges correspond to three retrackers, which are Ocean retracker (SAMOSA3), Ice-sheet retracker (MLE4), and OCOG retracker. We then extract 10 indicators from waveform, they are 1) thermal noise, 2) the number of peaks, 3) the position of the highest peak, 4) the power of the highest peak, 5) the position of the first peak, 6) the ratio of thermal noise and maximum power, 7) the width of the highest peak, 8) kurtosis, 9) peakiness, and 10) noise level. Moreover, 8 environmental indicators are also introduced, namely 1) the area of the river, 2) the width of the river, 3) the number of water bodies, 4) the distance between the river and nadir point, 5) vegetation coverage, 6) elevation variance, 7) elevation difference, and 8) crossing angle of the river and satellite track.

Base on the analysis of waveform and environmental indicators, we draw the following conclusions:

- The area and width of the river show a positive correlation with the width of the waveform peak. The width of the river performs greater influence in the case of the complex waveform or the complex environment, while the area of the river performs greater influence in a normal environment.
- The number of water bodies is related to the number of peaks.

- Comparison of elevation variation of whole footprints and the general result reveals that in the case of the complex waveform, the width of the river effectively influences the shape of the waveform, while the influence of the river decreases. Elevation variance plays an important role, but the elevation difference does not show any correlation with any waveform indicators.
- With the crossing angle approaching 90°, the width of the peak increase.
- The vegetation coverage and distance between the water body and nadir point do not show any significant relationship with the waveform.

In addition, there are some conclusions based on normal or complex environment:

- In the case of the normal environment, the noise level is significantly reduced. Most of the noise level is less than 0.03. The highest peak coincides exactly with the first peak. The number of peaks is essentially equal to one except in very rare cases. That means little complex waveform appears in this condition.
- In the case of the complex environment, more noise level indicators are larger than 0.03. This high noise level is associated with the elevation difference and the number of water bodies. More complex waveforms appear in the complex environment and their corresponding river widths are narrower than 140 m.

Base on the analysis of water level and two kinds of indicators, we draw the following conclusions:

- For samples that can be retracked by three methods, most waveforms have a low noise level and a low elevation difference. All of the waveforms have been set a proper reception window.
- For samples that can be retracked by Ocean and OCOG methods, the waveform with a low noise level also is the majority and the elevation difference does not affect the success of retracking.
- For samples that can be only retracked by Ocean or OCOG method, anomaly tracking and high noise level are the critical factors affecting retracking results.
- For the failure samples, their waveforms do not contain any water information but the pure noise.

At last, we further investigate the height difference between retrackers. We conclude that:

- Different retrackers applying offset on the different leading-edges results in a large height difference.
- The high noise level contributes to the large height difference between retrackers.
- The high elevation difference is related to the high noise level. At the same time, it can generate a large height difference between retrackers.

- The width of the river has an impact on the large height difference between retrackers.

6.2 Outlook

Without the reference height, we cannot evaluate the accuracy of each retracker and ulteriorly understand the environmental influence of it. In this study, however, the feasibility of investigating the relationship between the environment and the altimetry measurements has been proved. Thus, in the future study, one should obtain in-situ data of the selected river. Meanwhile, following and improving the research method in this thesis, we can determine more virtual stations on the river, for which in-situ data can be accessed. Once the in-situ data is acquired, we can determine the interference which may reduce the accuracy due to the complex environment. Finally, according to different environments, we can design more advanced methods to eliminate their interference and improve the accuracy of altimetry measurements over inland application.

Reference

[1] Berry, P., Garlick, J., Freeman, J. & Mathers, E. (2005), 'Global inland water monitoring from multi-mission altimetry', *Geophysical Research Letters* 32(16).
URL: *https://doi.org/10.1029/2005GL022814*

[2] Biancamaria, S., Schaedele, T., Blumstein, D., Frappart, F. (2018), 'Validation of Jason-3 tracking modes over French rivers', *Remote Sensing of Environment* (209), 77-89.
URL: *https://doi.org/10.1016/j.rse.2018.02.037*

[3] Brown, G. S. (1977), 'The average impulse response of a rough surface and its applications', *IEEE TRANSACTIONS ON ANTENNAS AND PROPAGATION* AP-25.
URL: *https://doi.org/10.1109/TAP.1977.1141536*

[4] Cartwright, D. E., Ray, R. D. (1990), 'Oceanic tides from Geosat altimetry'. *Journal of Geophysical Research* 95(C3):3069.
URL: *https://doi.org/10.1029/JC095iC03p03069*

[5] Chelton, D. B., Walsh, E. J., MacArthur, J. L. (1989), 'Pulse Compression and Sea Level Tracking in Satellite Altimetry',*J. Atmos. Oceanic Technol*. 6(3), 407–438.
URL:*https://doi.org/10.1175/1520-0426(1989)006<0407:PCASLT>2.0.CO;2*

[6] Chelton, D. B., Ries, J. C., Haines, B. J., Fu, L.-L. and Callahan, P. S. (2001), 'Satellite Altimetry, in: Satellite Altimetry and Earth sciences: A Handbook of Techniques and Applications, Fu, L.-L. and Cazenave, A. (eds.)', pp. 1–132.

[7] Dinardo, S. (2020), 'Techniques and Applications for Satellite SAR Altimetry over water, land and ice', PhD Thesis, Technische Universität Darmstadt.
URL: *https://doi.org/10.25534/tuprints-00011343*

[8] Dinardo, S., Lucas, B., Benveniste, J. (2015), 'Sentinel-3 STM SAR ocean tracking algorithm and SAMOSA model', in: 2015 IEEE international geoscience and remote sensing symposium (IGARSS), Milan, pp 5320–5323.

[9] ESA (2010), Cryosat Product Handbook.

[10] ESA (2018), Cryosat-2 Product Handbook Baseline D 1.0 C2-LI-ACS-ESL-5319.

[11] ESA (2018), 'Sentinel-3 Core PDGS Instrument Processing Facility (IPF) Implementation: Product Data Format Specification - SRAL/MWR Level 2 Land products'.

[12] Fernandes, M., Lázaro. (2018), 'Independent Assessment of Sentinel-3A Wet Tropospheric Correction over the Open and Coastal Ocean', *Remote Sensing* 10(3).
URL: *https://doi.org/10.3390/rs10030484*

[13] Fu, L.-L. & Cazenave, A. (2000), 'Satellite altimetry and earth sciences: a handbook of techniques and applications', Vol. 69, Elsevier.

[14] Gao, X. (2020), 'Research on Waveform Retracking of Coastal Satellite Radar Altimetry Data', Master Thesis, Wuhan University.

[15] Gao, Q., et al. (2019), 'Analysis of Retrackers' Performances and Water Level Retrieval over the Ebro River Basin Using Sentinel-3', *Remote Sensing* 11(6).
URL: *https://doi.org/10.3390/rs11060718*

[16] Gleick, P. H. (1993), 'Water in crisis', *Pacific Institute for Studies in Dev., Environment & Security. Stockholm Env. Institute, Oxford Univ.* Press. 473p 9.

[17] Hagemann, S., Chen, C., Clark, D.B., Folwell, S. (2013), 'Climate change impact on available water resources obtained using multiple global climate and hydrology models', *Earth System Dynamics* 4 (1), 129-144.
URL: *https://doi.org/10.5194/esd-4-129-2013*

[18] Jain, M., et al. (2014), 'Evaluation of SAMOSA3 adapted retracker using Cryosat-2 SAR altimetry data over the Arctic ocean', in: 2014 IEEE international geoscience and remote sensing symposium (IGARSS).
URL: *https://doi.org/10.1109/IGARSS.2014.6947648*

[19] Kaula, W. M. (1969), Solid-Earth and ocean physics--Report of a study at Williamstown, Mass. to the National Aeronautics and Space Administration, Cambridge, Mass.

[20] Kleinherenbrink, M., Lindenbergh, R. C. (2015), 'Monitoring of lake level changes on the Tibetan Plateau and Tian Shan by retracking Cryosat SARIn waveforms', *Journal of Hydrology* 521, 119-131.
URL: *https://doi.org/10.1016/j.jhydrol.2014.11.063*

[21] Le Gac, S., Boy, F., Blumstein, D., Lasson, L., Picot, N. (2019), 'Benefits of the Open-Loop Tracking Command (OLTC): Extending conventional nadir altimetry to inland waters monitoring', *Advances in Space Research.*

URL: *https://doi.org/10.1016/j.asr.2019.10.031*

[22] Leitao C. D., Mcgoogan J. T. (1976), 'Satellite altimetry applied to marine geoid determination', *Acta Astronautica* 3(5-6), 459-469.
URL: *https://doi.org/10.1016/0094-5765(76)90150-8*

[23] Maillard, P., et al. (2015), 'New processing approaches on the retrieval of water levels in Envisat and SARAL radar altimetry over rivers: A case study of the São Francisco River, Brazil '*Remote Sensing of Environment* 156: 226-241.
URL: *https://doi.org/10.1016/j.rse.2014.09.027*

[24] Marth, P. C., Jensen, J. R., Kilgus, C. C., Perschy, J. A., MacArthur, J. L., Hancock, D. W., Hayne, G. S., Purdy, C. L., Rossi, L. C. and Koblinsky, C. J. (1993), 'Prelaunch performance of the NASA altimeter for the TOPEX/Poseidon project', *IEEE* 31, NO. 2.
URL: *https://doi.org/10.1109/36.214909*

[25] Milliman, J.D., Meade, R.H. (1983), 'World-wide delivery of sediment to the oceans', *Journal of Geology* 91 (1), 1–21.
URL: *https://www.jstor.org/stable/30060512*

[26] Nielsen, k., et al. (2017), 'The Performance and Potentials of the CryoSat-2 SAR and SARIn Modes for Lake Level Estimation' *Water* 9(6).
URL: *https://doi.org/10.3390/w9060374*

[27] Rapley, C. G., M. A. J. Guzkowska, W. Cudlip, and I. M. Mason (1987), 'An exploratory study of inland water and land altimetry using Seasat data', *ESA* Rep. 6483/85/NL/BI.

[28] Remy, F., et al. (2012), 'Radar altimetry measurements over antarctic ice sheet: A focus on antenna polarization and change in backscatter problems', *Advances in Space Research* 50(8): 998-1006.
URL: *https://doi.org/10.1016/j.asr.2012.04.003*

[29] Sandwell, D. T. & Smith, W. H. F. (2005), 'Retracking ERS-1 altimeter waveforms for optimal gravity field recovery', *Geophysical Journal International* 163(1): 79-89.
URL: *https://doi.org/10.1111/j.1365-246X.2005.02724.x*

[30] Shu, S., et al. (2020), 'Analysis of Sentinel-3 SAR altimetry waveform retracking algorithms for deriving temporally consistent water levels over ice-covered lakes', *Remote Sensing*239, 111643.
URL: *https://doi.org/10.1016/j.rse.2020.111643*

[31] Tapley B. D., Born G. H., Parke M. E. (1982), 'The SEASAT altimeter data and its accuracy assessment', *Journal of Geophysical Research* 87(C5), 3179.
URL: *https://doi.org/10.1029/JC087iC05p03179*

[32] Tourian, M. J. (2012), 'Controls on satellite altimetry over inland water surfaces for hydrological purposes', Master Thesis, University of Stuttgart.
URL: *http://dx.doi.org/10.18419/opus-3879*

[33] USUG (2019), Landsat 8 (L8) Data Users Handbook LSDS-1574 Version 5.0

[34] Vignudelli, S., Kostianoy, A. G., Cipollini, P., Benveniste, J. (2011), Coastal Altimetry. Berlin Heidelberg. Springer-Verlag.

[35] Wingham, D.J., Francis, C.R., Baker, S., et al. (2006), 'CryoSat: A mission to determine the fluctuations in Earth's land and marine ice fields' *Adv. Space* Res.37, 841–871.
URL: *https://doi.org/10.1016/j.asr.2005.07.027*

[36] Wingham, D. J., Rapley, C. & Griffiths, H. (1986), New techniques in satellite altimeter tracking systems, *in* 'Proceedings of IGARSS', Vol. 86, pp. 1339–1344.

[37] Xu, H. (2007), 'Modification of normalised difference water index (NDWI) to enhance open water features in remotely sensed imagery', *International Journal of Remote Sensing* 27(14): 3025-3033.
URL: *https://doi.org/10.1080/01431160600589179*

[38] Yue, W., et al. (2007), 'The relationship between land surface temperature and NDVI with remote sensing: application to Shanghai Landsat 7 ETM+ data' *International Journal of Remote Sensing* 28(15): 3205-3226.
URL: *https://doi.org/10.1080/01431160500306906*